SUPPORTING INFORMATION

ORIGIN OF THE URUCUM IRON FORMATIONS (NEOPROTEROZOIC, BRAZIL): TEXTURAL AND MINERALOGICAL EVIDENCE (Mato Grosso do Sul – Brazil)

Running title: Fe-rich rocks from Urucum

Márta Polgári[1,2*], João Carlos Biondi[3], Ildikó Gyollai[1], Krisztián Fintor[4], Máté Szabó[1]

[1]*Institute for Geological and Geochemical Research, RCAES, Eötvös Loránd Research Network, 1112 Budapest, Budaörsi u. 45, Hungary, e-mail: rodokrozit@gmail.com, gyildi@gmail.com, szmatez@gmail.com*

[2]*Eszterházy Károly University, Dept. of Natural Geography and Geoinformatics, 3300 Eger, Leányka u. 6, Hungary*

[3]*Federal University of Paraná State, Polytechnic Center, Geology Department, 81531-980 Curitiba, Brazil, e-mail: biondiufpr@gmail.comS*

[4]*Szeged University, Dept. of Mineralogy, Geochemistry and Petrology, 6722 Szeged, Egyetem u. 2-6, Hungary, e-mail: efkrisz@gmail.com*

**corresponding author:*
rodokrozit@gmail.com

Content

SI 1. Iron deposits similar to Urucum

SI-2. Panorama and high resolution optical rock microscopic photos of thin sections

SI 3. FTIR measurement of Urucum iron ore deposit

SI 4. FTIR dataset of samples

SI 5. Raman spectroscopy dataset of samples

SI 6. Mineral composition of nodules and sections based on Raman spectroscopy

SI 7. Raman profiles of nodules

SI 8. Raman profiles of sections

SI 9. Back scattered electron images of samples with mineral composition

SI 10. Element map images in a complex system with OM, CL, FTIR, Raman and stable isotope datasets

SI 11. Carbonate composition of samples based on EPMA analyses

SI 12. Carbonate composition of samples based on EPMA analyses

SI 13. Temperature calculation on $\delta^{18}O_{SMOWcarb}$ (based on Kim et al., 2009; Hodel et al., 2018)

Table S1. Samples and methods used

Table S2. Mineral and organic matter composition and frequency

Table S3. Raman profiles, point dataset and FTIR mineralogy both for nodules and sections according to Fe and Mn cycles and syn-and diagenetic formation

Table S4. Mineral assemblage in Urucum Fe ore, Brazil. and typical minerals indicative of Eh-pH ranges based on environmental mineralogy (low T)

Table S5. Carbonate types and $\delta^{13}C_{PDBcarb}$ and $\delta^{18}O_{PDBcarb}$ values of sedimentary carbonates in BIFs and Mn ore from Urucum and Vetorial mines, Urucum region (MS, Brazil)

SI 1. Iron deposits similar to Urucum

Ever since Young (1976) described the iron formations of the Rapitan Group (Canada), and genetically related them to Neoproterozoic glaciations, authors who work with iron formations across the planet have adopted the term "Rapitan-type iron formation" to designate all BIFs formed at the end of the Neoproterozoic. Klein and Beukes (1993a, 1993b) showed that the Rapitan Group is aged between 755 and 730 Ma and that it is coeval with several other extensive iron-formations worldwide, all of which are associated with glaciogenic sequences. These sequences would have be related in origin to the enrichment in Fe^{2+} of seawater, isolated from the atmosphere by ice crusts generated by regional glaciations from the end of the Neoproterozoic (according to the Snowball Earth Theory of Kirschvink, 1992). With the end of the glaciation and the disappearance of glaciers, in some restricted places on the continental shelves there would have been the oxidation of Fe^{2+} to Fe^{3+} which, being insoluble in sea water, would sediment together with a large amount of jasper, forming BIFs.

Included in the Rapitan Group type are the following iron-manganesiferous units: (1) Urucum district of Brazil (Urban et al., 1992; Trompette et al., 1998; Klein and Ladeira, 2004), (2) Mutum in Bolivia (Trompette et al., 1998), (3) MacKenzie and Ogilvie Mountains of North America (Young, 1976; Klein and Beukes, 1993a, b), (4) southeastern Uruguay (Pecoits et al., 2008), (5) Damara orogen of Namibia (Breitkopf, 1988; Bühn et al., 1992), (6) Adelaide geosyncline of South Australia (Lottermoser and Ashley, 1999), (7) Erzin basin in Tuva, Russia, and in adjacent Mongolia (Ilyin, 2009), (8) Malyi Khingan in the southern part of the Russian Far East (Ilyin, 2009), and (9) middle Tien-Shan in Kazakhstan, Kyrgyzstan.

Urucum, located in Brazil, and Mutum, located in Bolivia, are different names given to the same geological unit. The eastern part of the Jacadigo Hill (Fig. 1A), located in Brazil, belongs to the Santa Cruz Formation of the Jacadigo Group, which contains several iron-manganese units, including those from the Urucum mine, the name that was historically adopted to designate around 10 other iron and manganese deposits and mines of the Santa Cruz Formation. Crossing the border to the west and entering Bolivia, the western part of Jacadigo Hill is called Mutum (Trompette et al., 1998). The geology and genesis of banded iron formations (BIFs) of the Urucum-Mutum and of the manganese deposits interstratified in these iron formations have been discussed in many publications, among which the most recent and comprehensive are Klein and Ladeira (2004), Angerer et al. (2016), Biondi and Lopez (2017), and Biondi et al. (2020).

Urban et al. (1992) considered the iron formations of the Urucum region similar to the iron formations of the Rapitan Group. By similarity, Urban et al. (1992) considered that the Urucum BIFs would be Cryogenian (720-635 Ma), and their genesis, like the Rapitan Group, would be related to the great glaciations of the late Neoproterozoic, especially to the Marinoan glaciation (650 to 635 Ma).

After Urban et al. (1992), and Klein and Beukes (1993) several authors adopted the same ideas about the Urucum, even though Biondi and Lopez (2017) and Biondi et al. (2020) describe several geological features that indicate that the BIFs of Urucum (and Mutum) are Ediacarans, aged 560-550 Ma (Piacentini et al., 2013; Biondi and Lopez, 2017; Biondi et al., 2020). Indeed, the iron formations of the Rapitan Iron Formation Group, especially at Cranswick River, Mackenzie Mountains, of the Canada Northwestern Territories, are very similar to those of the Urucum. Layers with nodular and banded jasper interlayered with hematite bands and overprinted by anastomosing hematite are similar to the arkosean iron formations located at the base of the Santa Cruz Formation (Biondi and Lopez, 2017), and the BIFs with jasper nodules in massive hematite (Bekker et al., 2010) are very similar to the BIF types 4 and 4A (Fig. 3), one of the most common BIF-type in the Urucum. On the other hand, besides their ages, Urucum and Rapitan have some other important differences. The total thickness of the Rapitan Group's BIFs rarely exceeds 70 m, but it is more than 400 m in Urucum. In Rapitan there are diagnostic evidences of sedimentation in a glacial environment, with frequent diamictites, dropstones, striated pebbles, etc., while in Urucum no diagnostic evidence was found for regional glacial environments, and the coarse grained rocks are conglomerates formed by avalanches. There are no manganese layers interspersed in the Rapitan Group's BIFs, while in Urucum there are three layers of manganese that are economically very important, with thicknesses between 0.5 and 6.0 m, of biogenic origin (Biondi and Lopez, 2017; Biondi et al. 2020), interspersed in the BIFs of the basal portion of the Santa Cruz Formation. Another important difference between the two units is indicated by multi-element REE diagrams. Urucum BIFs have negative Ce anomalies ranging from discrete to large (Angerer et al., 2016; Biondi and Lopez, 2017) indicating a marine sedimentary environment with hot water (Angerer et al., 2016; Biondi and Lopez, 2017), which contrasts with the sedimentation in the glacial environment of Rapitan BIFs.

According to Klein and Beukes (1993a, b), the Rapitan Group is well exposed in the Mackenzie Mountains and in the eastern Wernecke Mountains of the northeastern Cordillera of North America, with correlatives in the upper Tindir Group (Young, 1982) in the Ogilvie Mountains on the Alaska-Yukon border. It unconformably overlies a thick platform assemblage of carbonates and relatively mature siliciclastics of the Mackenzie Mountains Supergroup (Young et al., 1979) and is paraconformably overlain by shale of the Twitya Formation, forming the base of the Hay Creek Group (Young et al., 1979). Young (1992) suggests that the glaciogenic Rapitan sequence correlates with the Mackenzie Mountains Supergroup in the northern Cordillera. The Mackenzie Mountains

Supergroup and the Ogilvie Mountains differ from the Rapitan Group only because the lower mixtite unit of the Rapitan is not developed in Mackenzie and Ogilvie Mountains. The BIFs, the stratigraphic sequence and the genetic process appear to be the same as those of the Rapitan Group.

The Arroyo del Soldado Group, in Uruguay, is a mixed siliciclastic-carbonate succession, mainly represented by an intercalation of basal pink dolostones, banded siltstones, rhythmites of dolostone-limestone, iron formations, cherts and conglomerates. According to Pecoits et al. (2008), these stratigraphic and chemostratigraphic features are suggestive of a Gaskier age (ca 580 Ma) for the basal glacial-related units. Gaucher et al. (1998) identified two different facies associations, shallow-water and deep-water. The shallow-water facies association is the most widely distributed and consists of basal conglomerates, followed by intercalations of sandstones and pelites in the middle of the succession, grading to banded siltstones at the top. The deep-water facies association comprises an alternation of finely laminated dark shales and arkoses; which are turbidites. More recently Gaucher et al. (2004) reported the presence of oxide-facies, a 50 m thick BIF with up to 24% magnetite/hematite. These rocks display centimeter alternation of chert and iron-rich layers that do not show the characteristic microbanding of Archean-Palaeoproterozoic (Pecoits et al., 2008), but which is similar to the BIF type 2 (Fig. 3) that occurs in Urucum. Gaucher et al. (1996) suggested that the succession was deposited on a stable continental shelf undergoing tectonic quiescence. Gaucher et al. (2004) suggested that deposition of the BIF took place on a shelf, due to enhanced upwelling of nutrient-rich waters and consequent production of phytoplankton blooms during greenhouse conditions. However, the depositional geological setting of the group does not correspond to an Atlantic-type continental shelf, in which the model was developed, and the age of the whole Arroyo del Soldado Group is younger than the Gaskiers glacial event, which is problematic for that model. Thus, in the absence of more evidence, the mechanism that triggered the iron precipitation remains unresolved (Pecoits et al., 2008).

Otjosondu, Namibia, is a region known mainly for its mines with ferruginous manganese ore, but which also contain some iron deposits derived from intensely metamorphosed BIFs, formed and deformed during the Neoproterozoic Damara orogenesis (Breitkopf, 1988; Bühn et al., 1992). Iron formations occur within the metasedimentary/metavolcanic sequence of the Chuos Formation, with age estimated between 750 and 650 Ma (Miller 1983). Hematite-feldspar-quartzites are considered impure and finely banded hematite-quartzites are recognized as pure iron-formations (Bühn et al., 1992). According to Breitkopf (1988), the iron-rich lithologies comprise magnetite-quartz, hematite-quartz and magnetite-quartz-silicate±carbonate rocks. Iron formation in amphibolite was developed both as a chemical sediment and as a composite rock consisting of chemical iron-rich sediment with admixture of varying amounts of volcanic detritus, while iron formation in diamictite represents a pure chemical sediment. Both of the iron-rich rocks contain abundant apatite and their manganese contents are low. The iron-rich horizons are reported to have a thickness of 20-30 m. The proposed depositional model involves chemical precipitation of dissolved iron (+ manganese) in high-energy, estuarine-deltaic environments. Lack of impurities of the iron-rich layers and their sharp upper and lower contacts indicate chemical precipitation in restricted basins during intervals of interrupted clastic deposition. For interpretation of sharp contacts, Polgári et al. (2016) and Biondi et al (2020) proposed changes of oxygen supply on a fine level between suboxic and obligatory oxic conditions, which determine microbial Fe(II) as suboxic and microbial Mn(II) oxidation as obligatory oxic, and enrichment of Fe- and Mn-ores. Breitkopf (1988) suggests an exhalative origin for the iron formations related to mafic volcanism and ensialic rifting. Because the banded ferriferous formations of Chuos Formation were destroyed by metamorphism and the associated deformation, it is not possible to compare them with those of Urucum.

The eastern part of the Adelaide Geosyncline (South Australia) contains well preserved glaciomarine sequences of the Sturtian glaciation (≈ 750–700 Ma) including calcareous or dolomitic siltstone, manganiferous siltstone, dolostone and diamictite units and the associated Braemar ironstone facies (Lottermoser and Ashley, 1999). The ironstone facies occurs as matrix to diamictites and as massive to laminated ironstones and comprises abundant Fe oxides (hematite, magnetite) and quartz, minor silicates (muscovite, chlorite, biotite, plagioclase, tourmaline), carbonate and apatite, and detrital mineral grains and lithic clasts. Laminated ironstones looking like BIF have magnetite and hematite-rich darker laminae and lighter laminae in siliciclastic and carbonate components. Interbedded lighter coloured siltstone displaying cross-laminations and soft-sediment deformation are common features. Micro-textures indicate that magnetite and hematite are of metamorphic origin. Chemical compositions of ironstones vary greatly and reflect changes from silica-, alumina-poor ironstones, formed by predominantly chemical precipitation processes, to silica-, alumina-rich examples with a significant detrital component. The intimate association of dolostones, manganiferous siltstones, ironstones and diamictites was explained by a transgressive event during a postglacial period. Hydrothermal exhalations added significant amounts of Fe and other metals to Neoproterozoic seawater. Release of CO_2 to the atmosphere from the oxygenated waters resulted in the precipitation of carbonate as dolostones, and oxygenation of ferriferous (± manganiferous) waters led to the precipitation of Fe^{3+} oxides as laminated ironstones and as matrix of diamictic ironstones (Lottermoser and Ashley, 1999). If the iron-rich rocks of the Adelaide Geosyncline are jaspilites, the abundance of cross-laminations and soft-sediment deformation would characterize them as unusual banded iron formations,

devoid of jasper nodules and small jasper lens, and very different from those existing in Urucum and the Rapitan Group.

The Erzin basin is likely to extend over several hundreds of kilometers southwestward, beneath the sand cover of the Borig Del Basin from Tuva to Mongolia, where BIFs are also found on the northern slopes of Khangai. Quite recently rocks hosting BIFs of the basin have been dated by the $^{206}Pb/^{238}U$ zircon method at 767 ± 15 Ma based on garnet–biotite plagio-gneiss underlying the quartzites (Ilyin, 2009).

The Erzin BIF, similar to those of the Rapitan Group (Ilyin, 2009), is localized in a tectonically active zone of conjunction of the Precambrian Tuva–Mongolia Massif and Caledonian structures. They differ from the BIFs in other regions mainly by a higher grade of metamorphism (amphibolite facies). They exhibit a clear banded structure related to the alternation of interbeds of magnetite and fine quartz grains. The Erzin BIF are divided into coarse- and thin-banded varieties. In some places, the thin-banded varieties comprise cummingtonite and pass into amphibole–magnetite rocks. Laminae are up to 2 cm thick in the coarse banded varieties and less than 0.7 mm thick in the thin banded varieties. The average ratio of magnetite and quartz laminae is 1:1 (Ilyin, 2009). Apparently the BIFs in the Erzin region were laminated and banded jaspilites (BIFs types 1 and 2, from Fig.3), which were metamorphosed and acquired a different mineral composition from that of the Urucum. No mention is made of the presence of nodular jaspilites (BIFs type 4 and 4A, Fig. 3).

The Erzin iron ore basin has the following specific features: (1) Stratigraphy section is composed of the lower meta-terrigenous and upper carbonate (conformably overlying) complexes. A small stratigraphic hiatus is likely to separate the complexes. Terrigenous rocks of the lower complex are metamorphosed up to the amphibolite–granulite facies. In the Mugur area, 200–300 m above glacial deposits, dolomites and black graphite marbles include several horizons of organic-rich phosphorites with a small amount of phosphoric anhydrite (10–15%). The $^{87}Sr/^{86}Sr$ absolute age of the phosphorite was estimated at ≈600 Ma. Therefore, BIFs belong to the Cryogenic interval of the Neoproterozoic, whereas phosphorites belong to the Ediacaran (Ilyin, 2009). (2) BIFs of the Mugur deposit occur 100–200 m below glacial deposits. The Mugur deposit has proven BIF reserves of approximately 300 Mt with bulk Fe content of 39–40%. The deposit encloses two contiguous, ≈10 m thick BIF beds extending over 60 km. The ore component is mainly represented by hematite or magnetite. The REE distribution and Co + Ni + Cu index suggest an influence of hydrothermal sources of Fe, although it was subordinate to the continental washout. According to Ilyin (2009) iron accumulated in seawater during glaciations, whereas iron mineralization took place at the earliest stages of postglacial transgressions. (3) BIFs are associated with graphitic shales and “red” muscovite schists with powdery pyrite dissemination. Similar occurrence of phosphorites and Neoproterozoic BIFs and their closeness in the stratigraphic section are also characteristic of the Malyi Khingan Ridge, Khankai region, Buryatia (Ilyin, 2009). Bekker (2010) mentions the existence of Neoproterozoic BIFs also in the Tien-Shan in Kazakhstan, Kyrgyzstan region, but no publications were found on these occurrences.

Only Urucum-Mutum has BIFs with mineral composition and structures similar to those of the Rapitan Group region, although apparently formed in a different time and geological environment. Among the diverse geological characteristics of the BIFs described above, the only characteristic common to all is that they are Neopoterozoic, with ages estimated between 767 ± 15 (Erzin region) and 550 Ma (Urucum). The second common feature, though not valid for all, is the origin in a glacial environment following the "Terra Bola de Neve" iron deposits model. Apparently an ice cap separating ocean water from the atmosphere was not necessary to accumulate large concentrations of iron after the GOE (Great Oxidation Event). This model probably does not apply to the Urucum, and also does not apply to BIFs in the Erzin region, where BIFs are 100–200 m stratigraphically below glacial deposits, to the magnetite or siderite iron formation of the Aok Formation, in Canada, with 840 Ma (Rainbird et al., 1994), or to the 1,400 Ma iron formation (IF) from the Xiamaling Formation of the North China Craton (Canfield et al., 2018). Therefore, substantial IFs formed without relation with glacial periods, in the time window between 1,800 and 800 Ma, where they are generally believed to have been absent, and during the transition between Neoproterozoic and Cambrian, at 660-650 Ma (Biondi et al., 2020).

REFERENCES

Bekker, A., Slack, J.F., Planavsky, N., Krapež, B., Hofmann, A., Konhauser, K.O., Rouxel, O.J., 2010, Iron Formation: The Sedimentary Product of a Complex Interplay among Mantle, Tectonic, Oceanic, and Biospheric Processes: Economic Geology, v. 105, pp. 467–508.

Biondi, J.C., Polgári, M., Gyollai, I., Fintor, K., Kovács, I., Fekete, J. & Mojzsis, S.J. 2020. Biogenesis of the Neoproterozoic kremydilite manganese ores from Urucum (Brazil) – a new manganese ore type. Precambrian Research 340, 105624. https://doi.org/10.1016/j.precamres.2020.105624

Biondi, J.C.; Lopez, M., 2017. Urucum Neoproterozoic–Cambrian manganese deposits (MS, Brazil): Biogenic participation in the ore genesis, geology, geochemistry, and depositional environment. Ore Geology Reviews 91:335-386.

Breitkopf, J.H., 1988, Iron formations related to mafic volcanism and ensialic rifting in the southern margin zone of the Damara orogen, Namibia: Precambrian Research, v. 38, p. 111−130.

Bühn, B., Stanistreet, I.G., and Okrusch, M., 1992, Late Proterozoic outer shelf manganese and iron deposits at Otjosondu (Namibia) related to the Damaran oceanic opening: Economic Geology, v. 87, p. 1393−1411.

Gaucher, C., Sial, A.N., Blanco, G., Sprechmann, P., 2004, Chemostratigraphy of the lower Arroyo del Soldado Group (Vendian, Uruguay) and palaeoclimatic implications. Gondwana Research., v.7, p.715–730.

Gaucher, C., Sprechmann, P. and Schipilov, A., 1996, Upper and Middle Proterozoic fossiliferous sedimentary sequences of the Nico Pérez Terrane of Uruguay: Lithostratigraphic units, paleontology, depositional environments and correlations. Neues Jb. Geol. Palaeontol. Abh., v. 199, p. 339–367.

Ilyin, A.V., 2009, Neoproterozoic banded iron formations: Lithology and Mineral Resources, v. 44, p. 78–86.

Kirschvink, Joseph L., 1992, Late Proterozoic Low-Latitude Global Glaciation: the Snowball Earth. *Late Proterozoic Low-Latitude Global Glaciation: the Snowball Earth.* In: The Proterozoic biosphere: a multidisciplinary study. Cambridge University Press, New York, pp. 51-52. ISBN 9780521366151

Klein, C., and Beukes, N.J.,1993a, Sedimentology and geochemistry of the glaciogenic Late Proterozoic Rapitan Iron Formation in Canada: Economic Geology, v. 88, p. 542–565.

Klein, C., and Beukes, N.J.,1993b, Proterozoic iron-formations, in Condie, K.C., ed., Proterozoic crustal evolution: Amsterdam, Elsevier, p. 383−418.

Klein, C., and Ladeira, E.A., 2004, Geochemistry and mineralogy of Neoproterozoic banded iron-formations and some selected, siliceous manganese formations from the Urucum district, Mato Grosso do Sul, Brazil: Economic Geology, v. 99, p. 1233−1244.

Lottermoser, B.G., and Ashley, P.M., 1999, Geochemistry, petrology and origin of Neoproterozoic ironstones in the eastern part of the Adelaide geosyncline, South Australia: Precambrian Research, v. 101, p. 49−67.

Miller, R. McG., 1983, The Pan-African Damara Orogen of South West Africa/Namibia. In: R McG Miller (Editor), Evolution of the Damara Orogen of South West Africa/Namibia. Special Publication of the Geological Society of South Africa, v. 11, p. 431-515.

Pecoits, E., Gingras, M.K., Aubet, N., and Konhauser, K.O., 2008, Ediacaran in Uruguay: Palaeoclimatic and palaeobiologic implications: Sedimentology, v. 55, p. 689−719.

Pecoits, E., Ingras, M.G., Aubet, N., Konhauser, K.O., 2008, Ediacaran in Uruguay: palaeoclimatic and palaeobiological implications: Sedimentology (2008) 55, 689–719.

Polgári, M., Hein, J.R., Bíró, L., Gyollai, I., Németh, T., Sajgó, C., Fekete, J., Schwark, L., Pál-Molnár, E., Hámor-Vidó, M., Vigh, T., 2016. Mineral and chemostratigraphy of a Toarcian black shale hosting Mn-carbonate microbialites (Úrkút, Hungary). Palaeogeography, Palaeoclimatology, Palaeoecology 459:99-120.

Trompette, R., Alvarenga, C.J.S., and de Walde, D., 1998, Geological evolution of the Neoproterozoic Corumbá graben system (Brazil): Depositional context of the stratified Fe and Mn ores of the Jacadigo Group: Journal of South America Earth Sciences, v. 11, p. 587−597.

Urban, H., Stribrny, B., and Lippolt, H.J., 1992, Iron and manganese deposits of the Urucum district, Mato Grosso do Sul, Brazil: Economic Geology, v. 87, p. 1375−1392.

Young, G.M., 1976, Iron formation and glaciogenic rocks of the Rapitan Group, Northwest Territories, Canada: Precambrian Research, v. 3, p.137−158.

Young, G.M., 1982, The Late Proterozoic Tindir Group, east-central Alaska: Evolution of a continental margin: Geological Society of America Bulletin, v. 93, p. 759-783.

Young, G.M., 1992, Late Proterozoic stratigraphy and the Canada-Australia Connection: Geology, v. 20, p. 215-218.

Young, G.M., Jefferson, C.W., Delaney, G.D., and Yeo, G.M., 1979, Middle and Late Proterozoic evolution of the northern Canadian Cordillera and Shield: Geology, v. 7, p. 125-128.

SI 2. Panorama and high resolution optical rock microscopic photos of thin sections

86 (transmitted light)

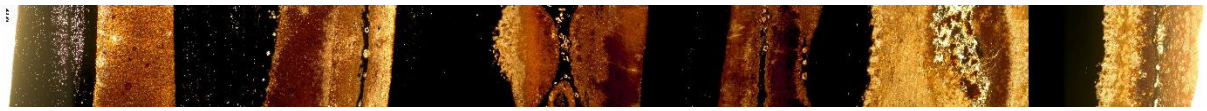

88 (transmitted light)

93 (transmitted light)

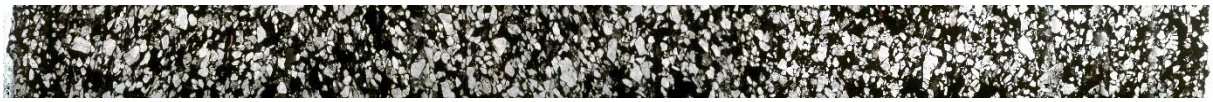

141 (transmitted light)

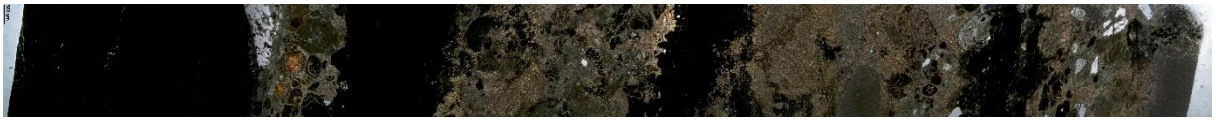

152 (transmitted light)

153A (transmitted light)

153B (reflected light)

157 (reflected light)

SI-2. Panorama microscopic photos of thin sections

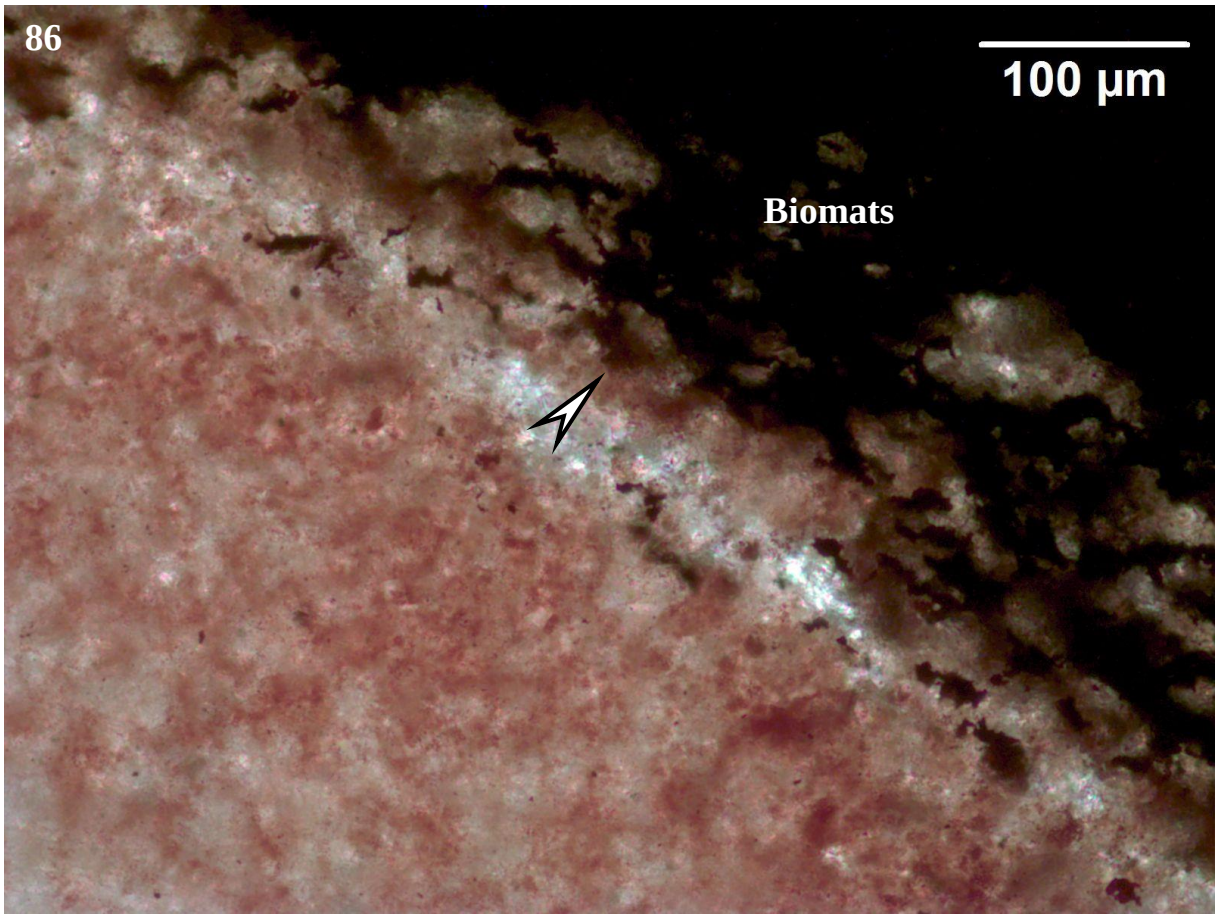
86
100 µm
Biomats

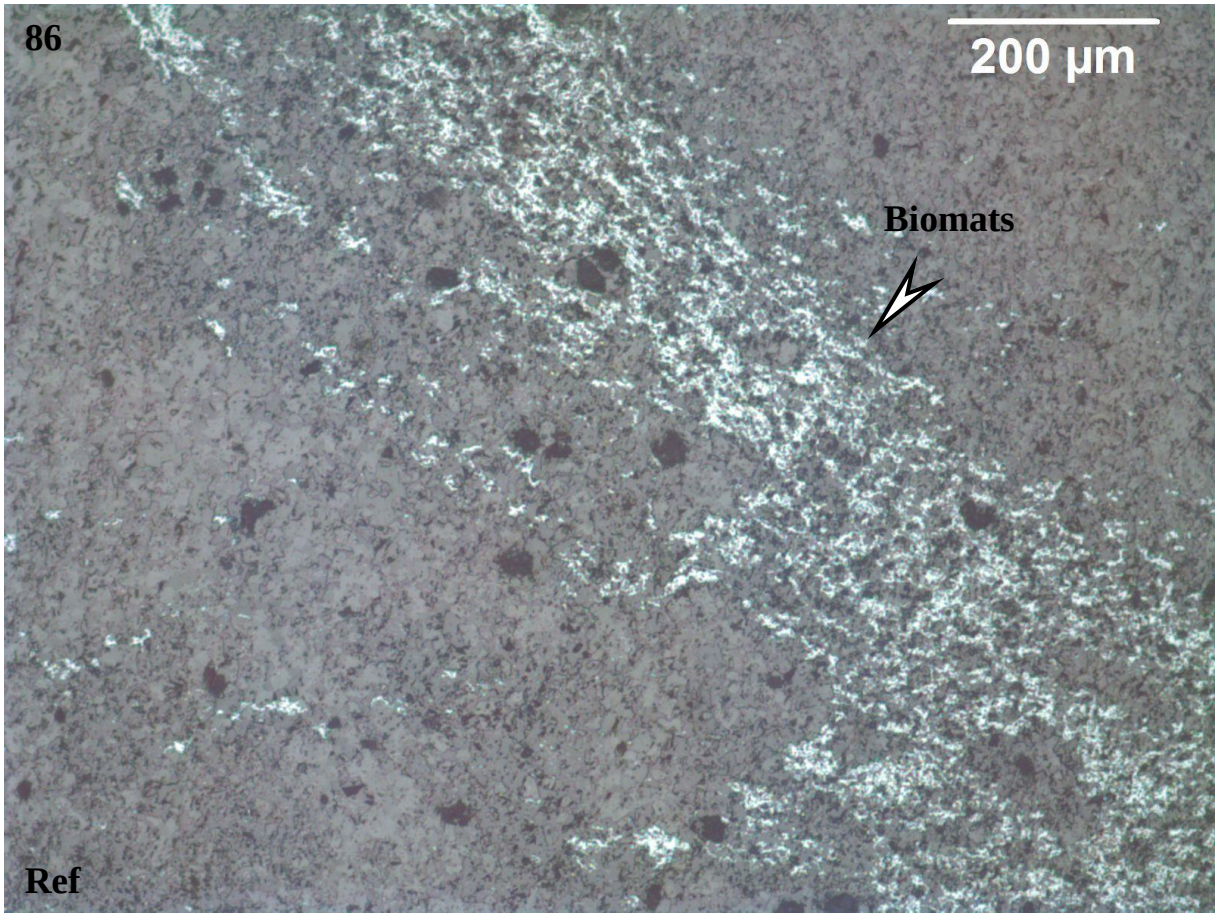
86
200 µm
Biomats
Ref

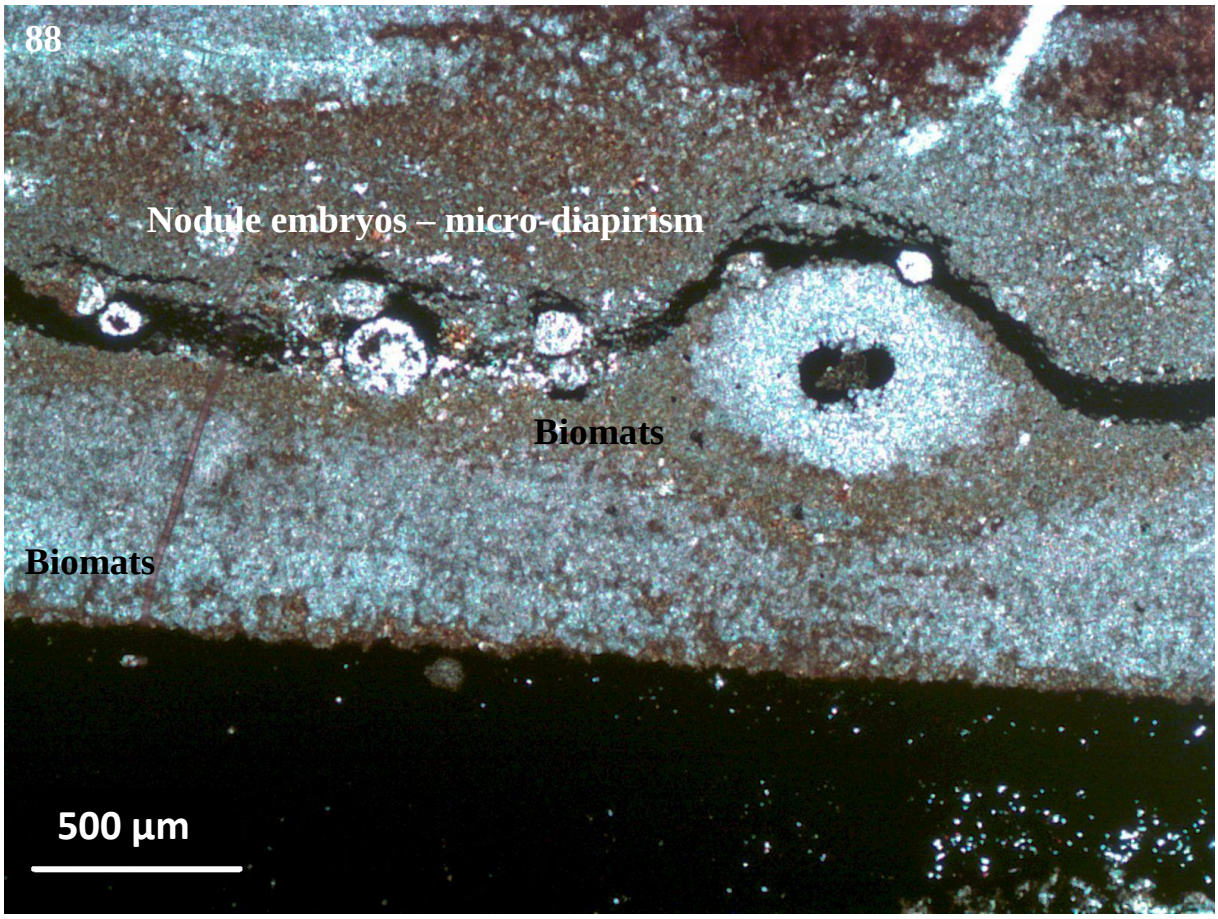
88
Nodule embryos – micro-diapirism
Biomats
Biomats
500 µm

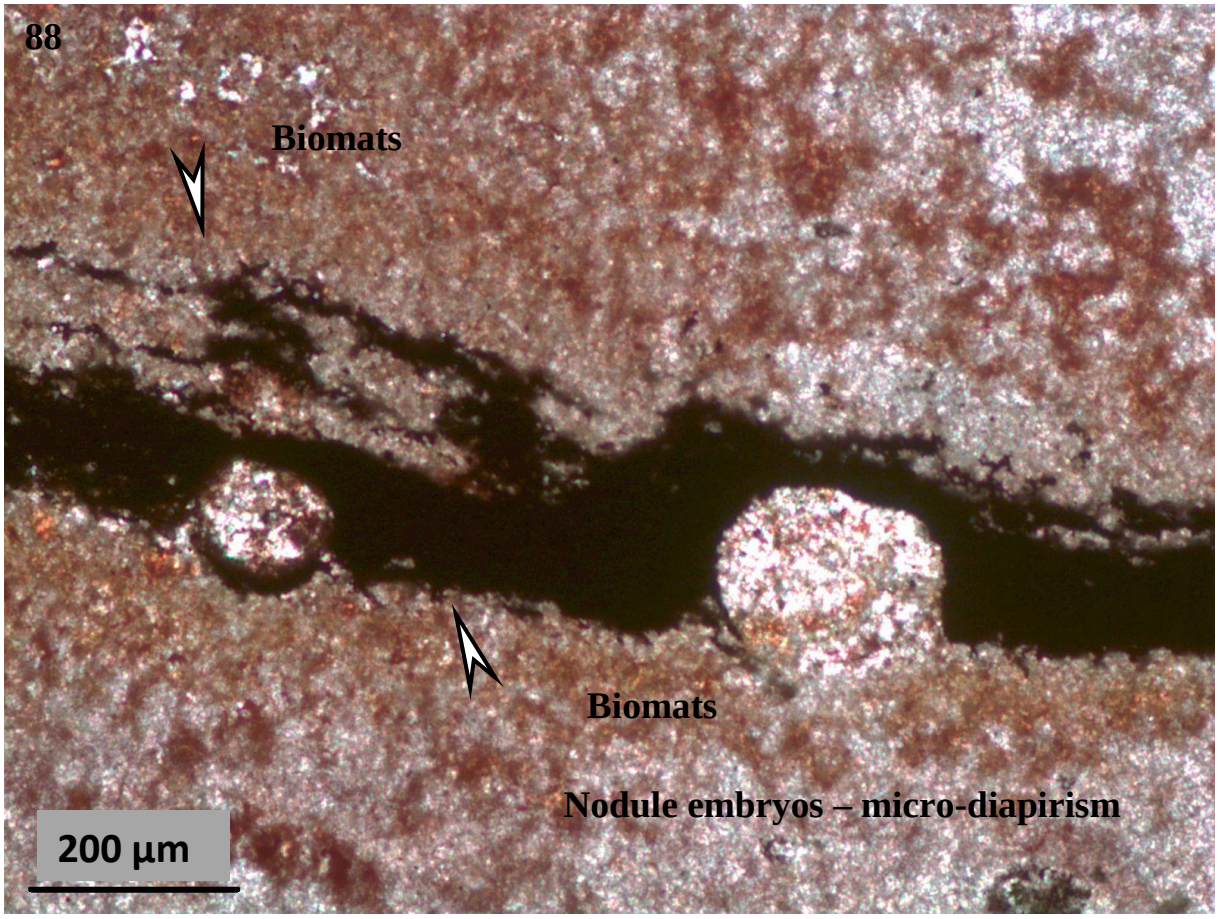
88
Biomats
Biomats
Nodule embryos – micro-diapirism
200 µm

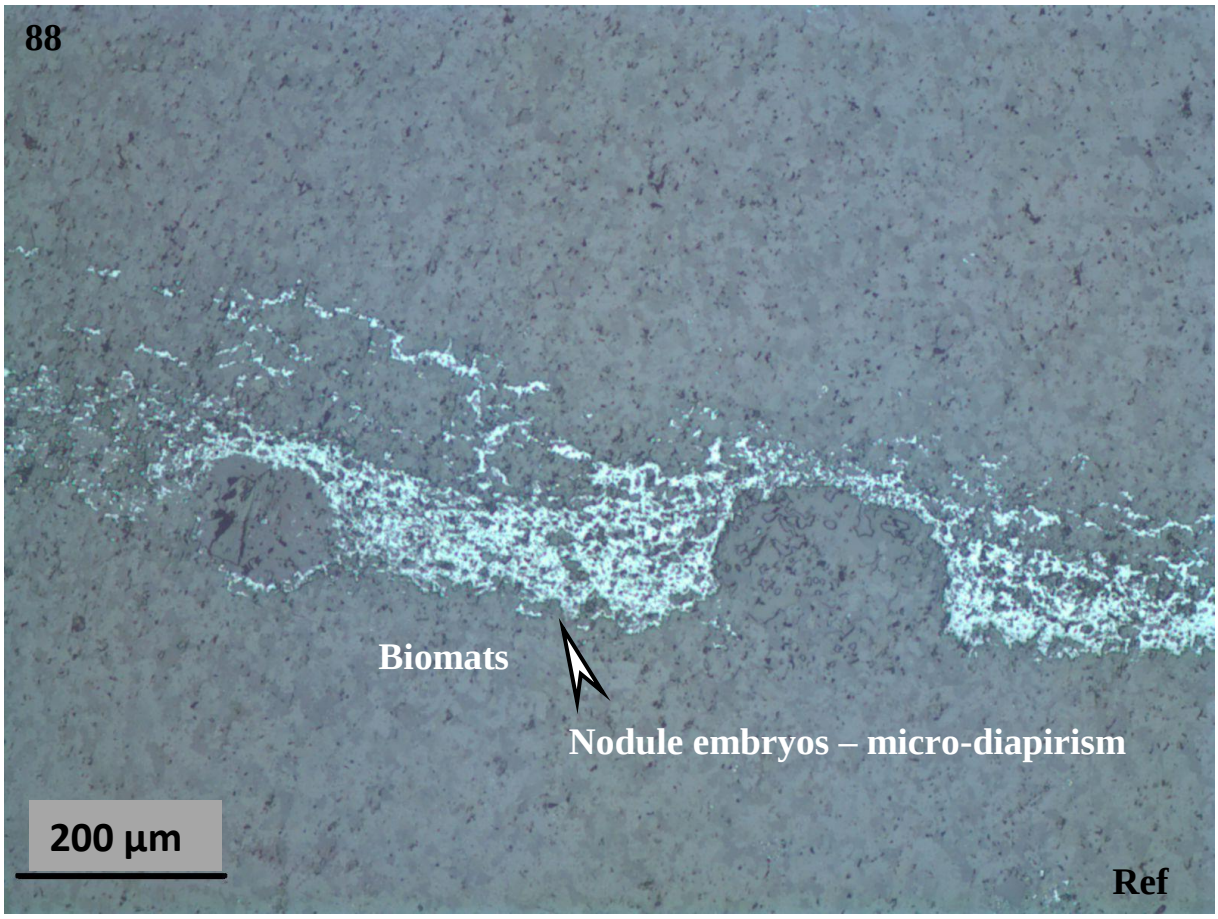
88
Biomats
Nodule embryos – micro-diapirism
200 µm
Ref

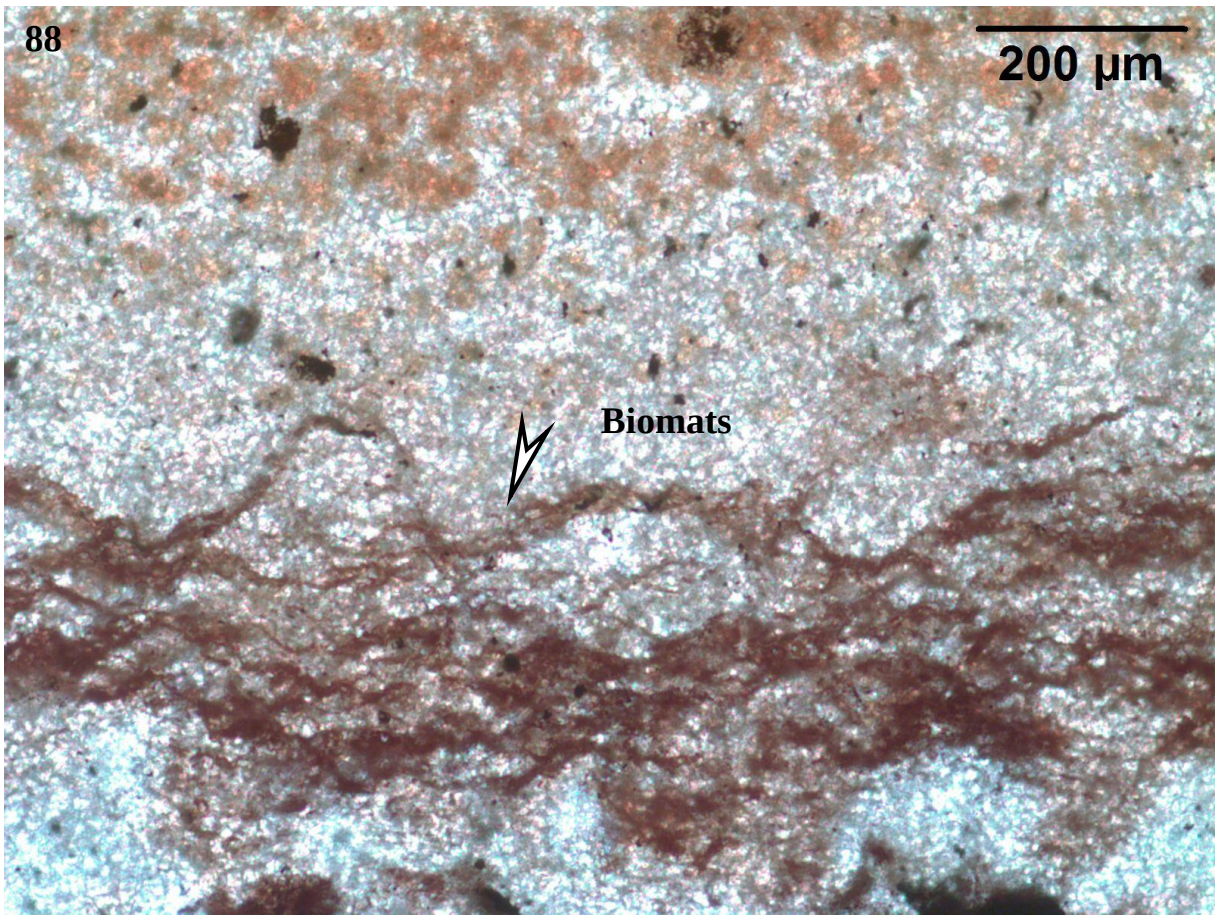
88
200 µm
Biomats

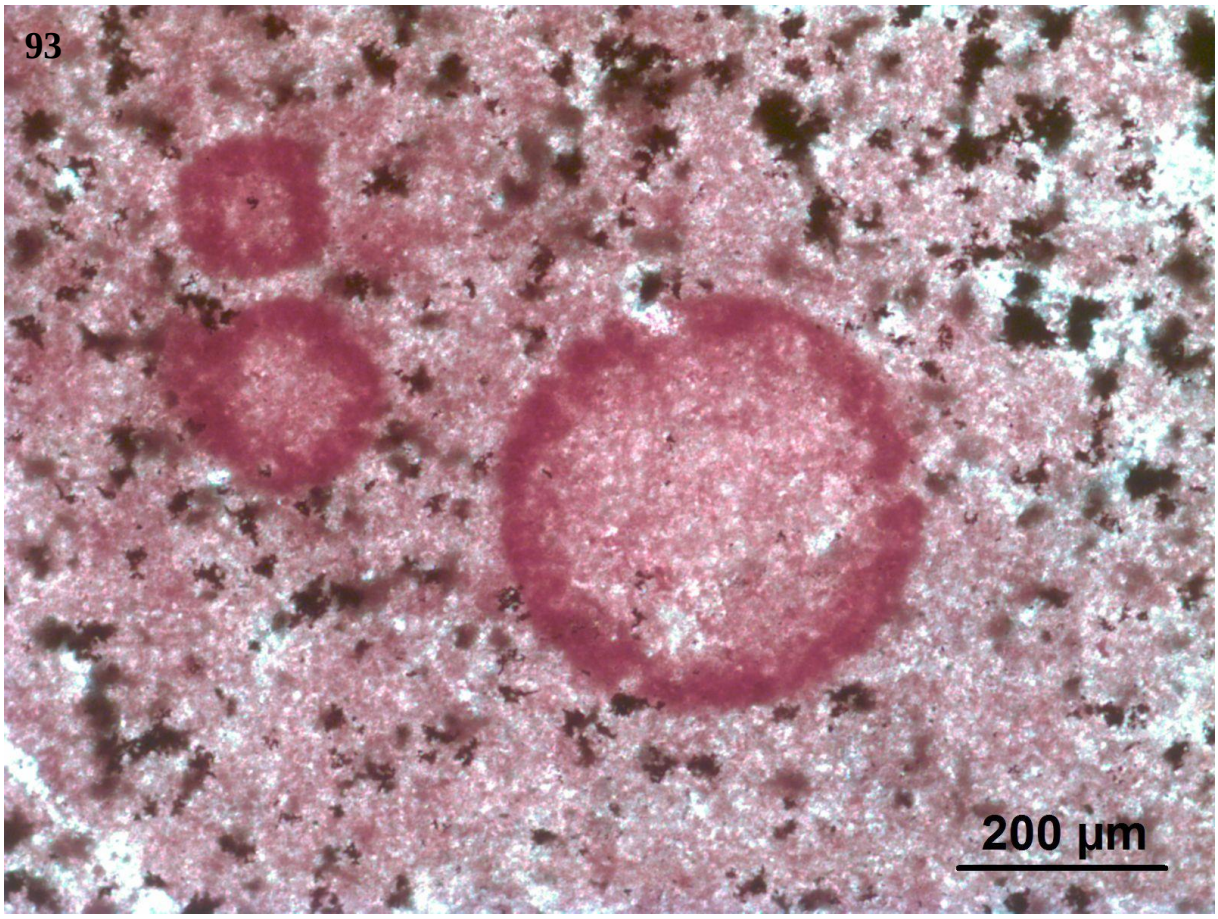
93
200 µm

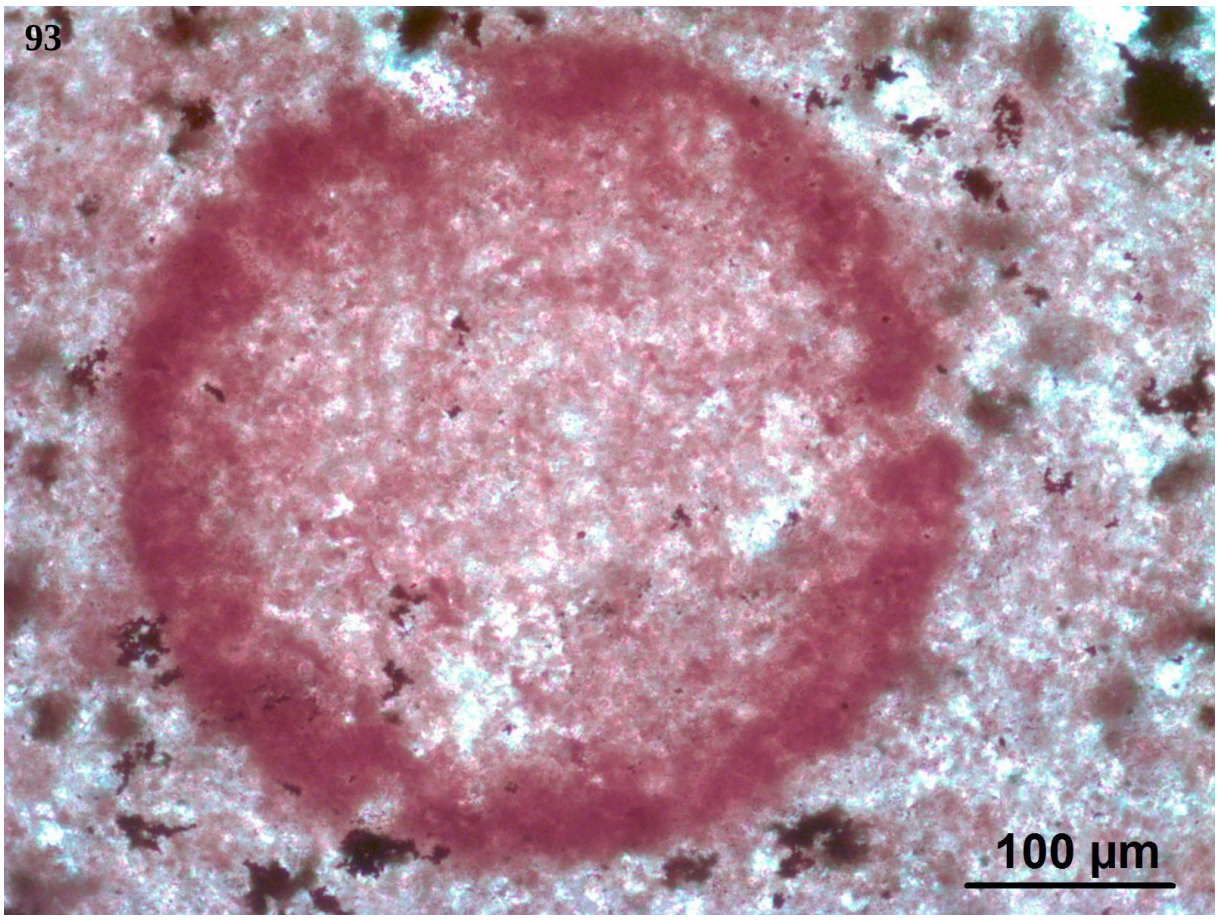
93
100 µm

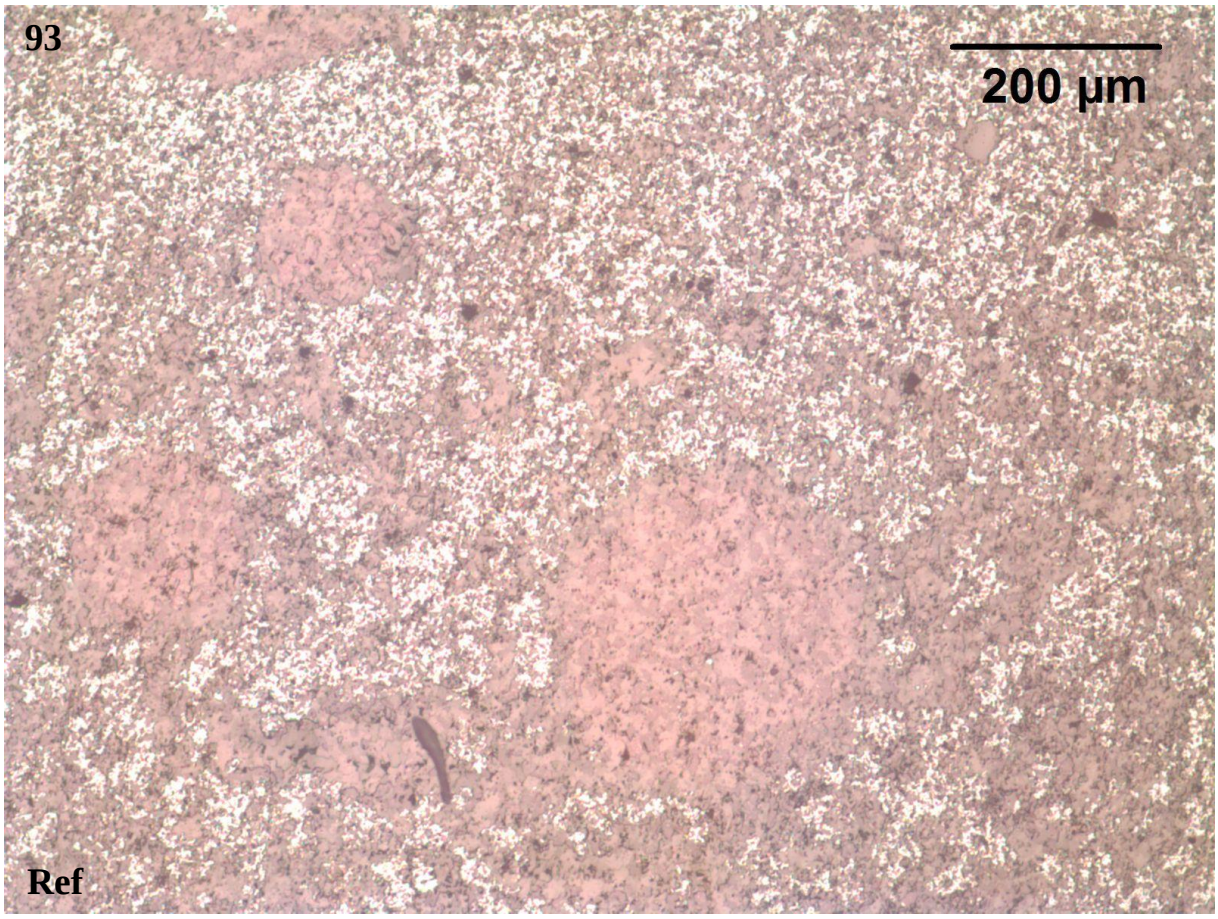
93
200 µm
Ref

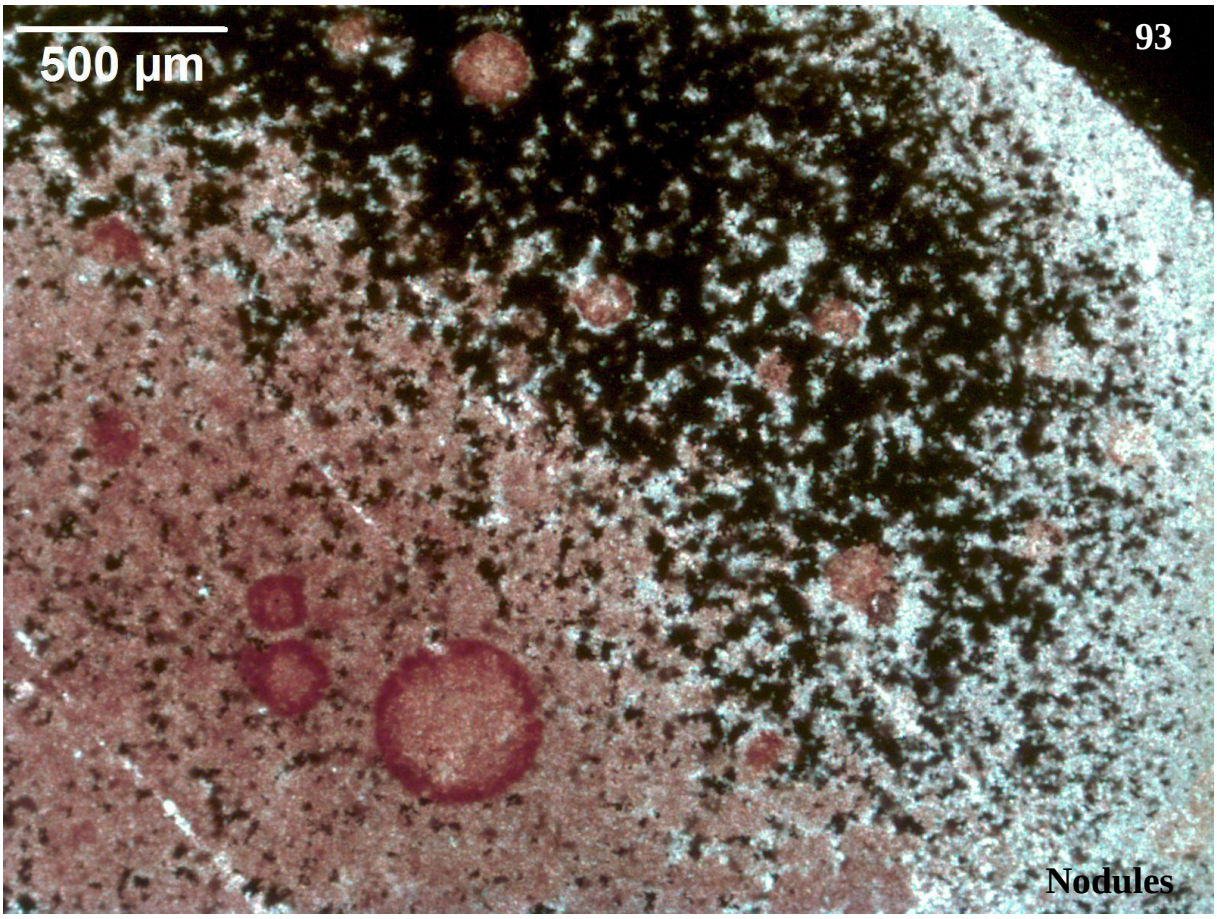
500 µm
93
Nodules

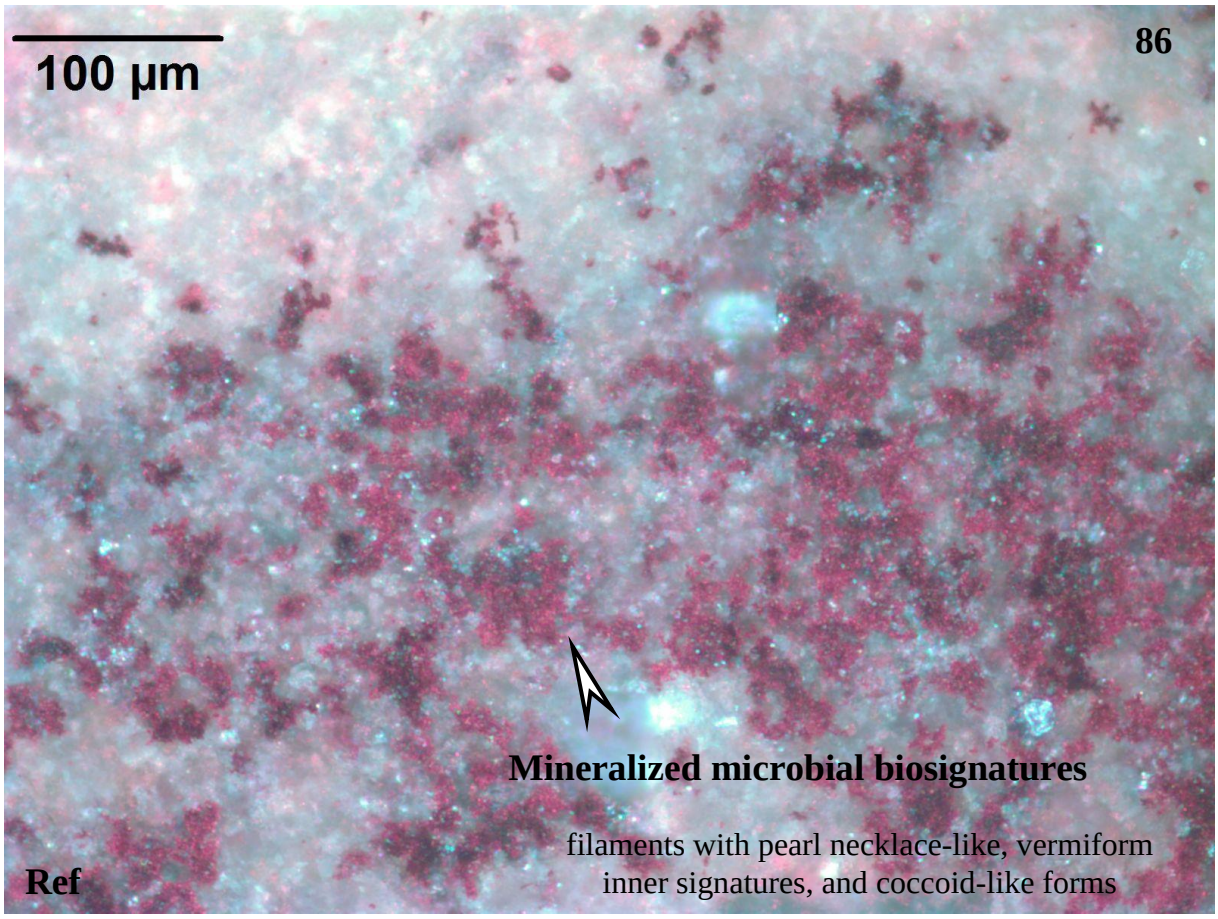
100 µm
86
Mineralized microbial biosignatures
filaments with pearl necklace-like, vermiform inner signatures, and coccoid-like forms
Ref

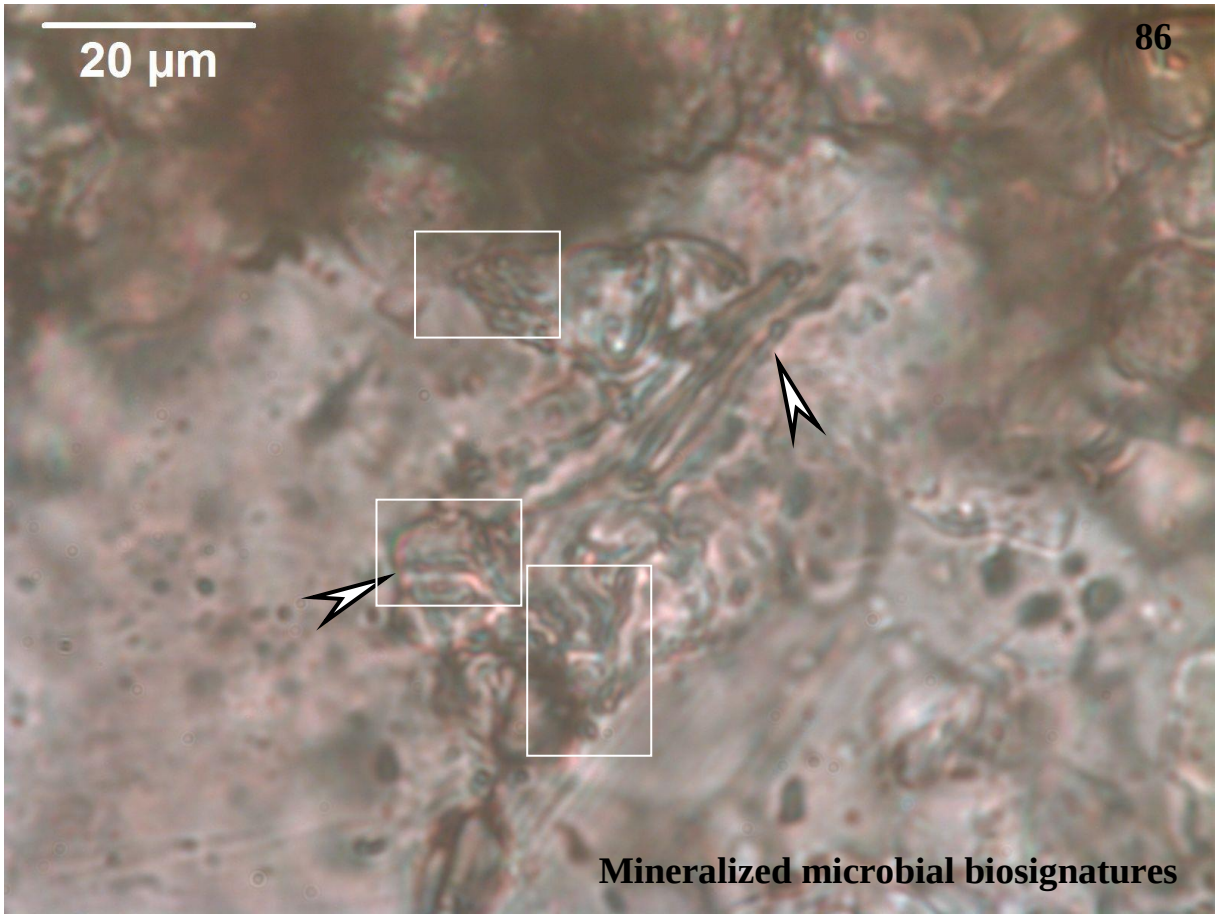
20 µm
86
Mineralized microbial biosignatures

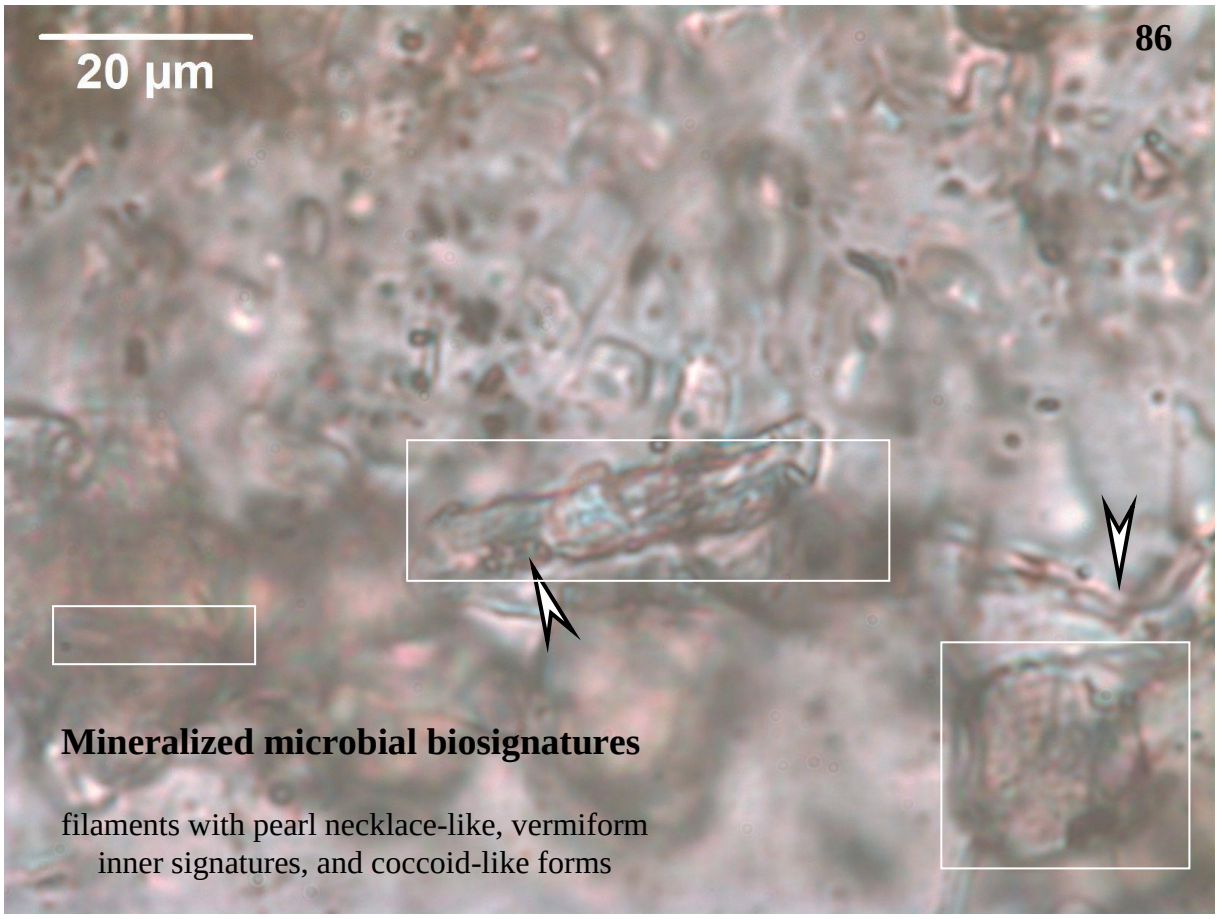
20 µm
86
Mineralized microbial biosignatures
filaments with pearl necklace-like, vermiform inner signatures, and coccoid-like forms

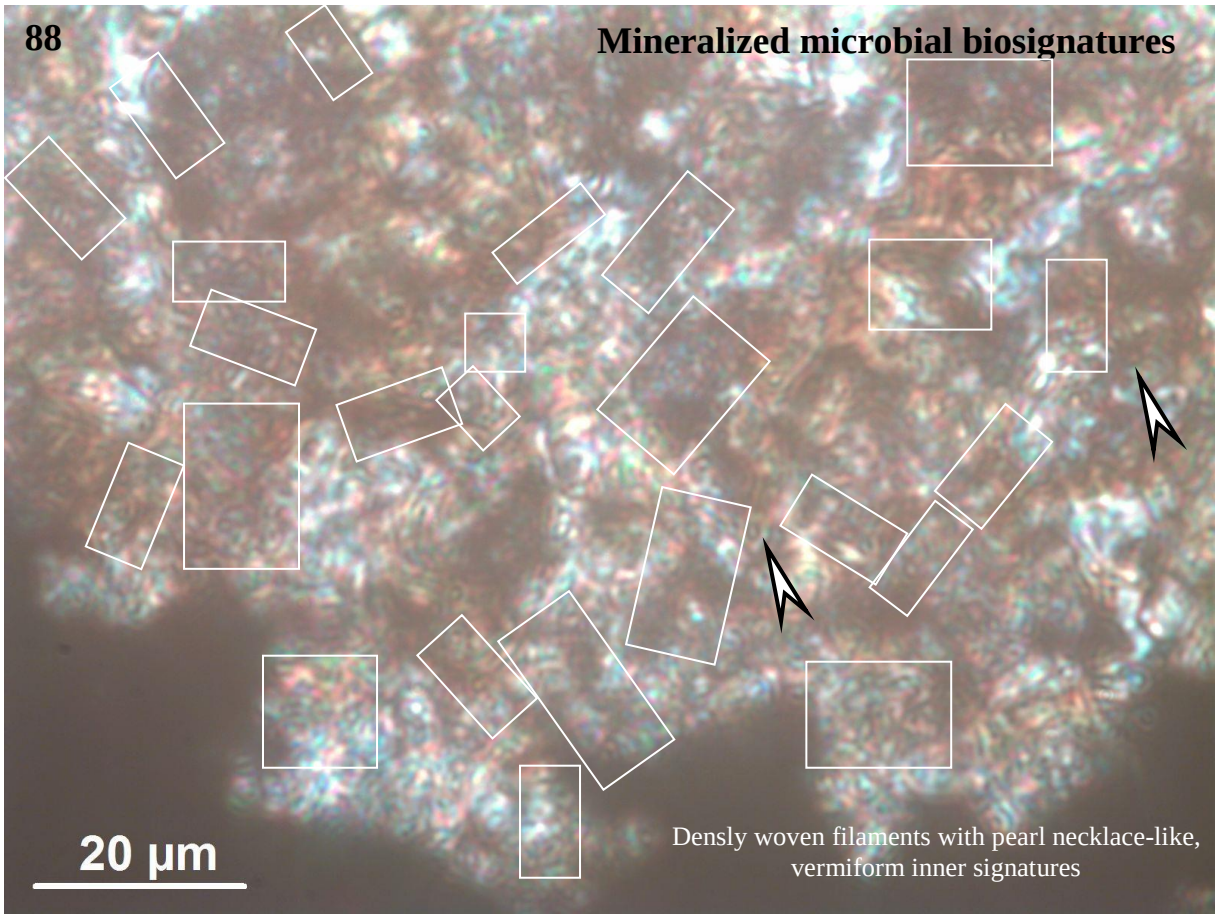
88
Mineralized microbial biosignatures
20 µm
Densly woven filaments with pearl necklace-like, vermiform inner signatures

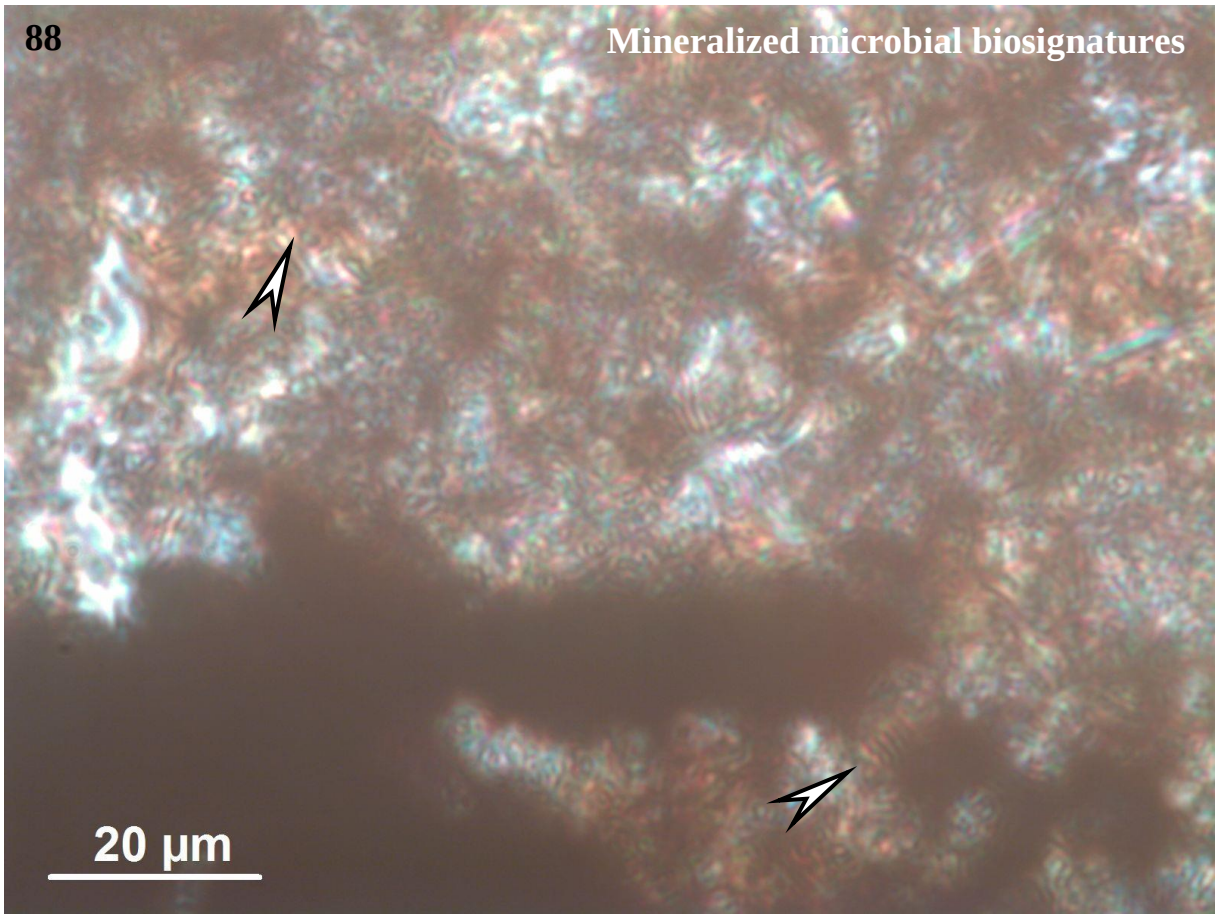
88
Mineralized microbial biosignatures
20 µm

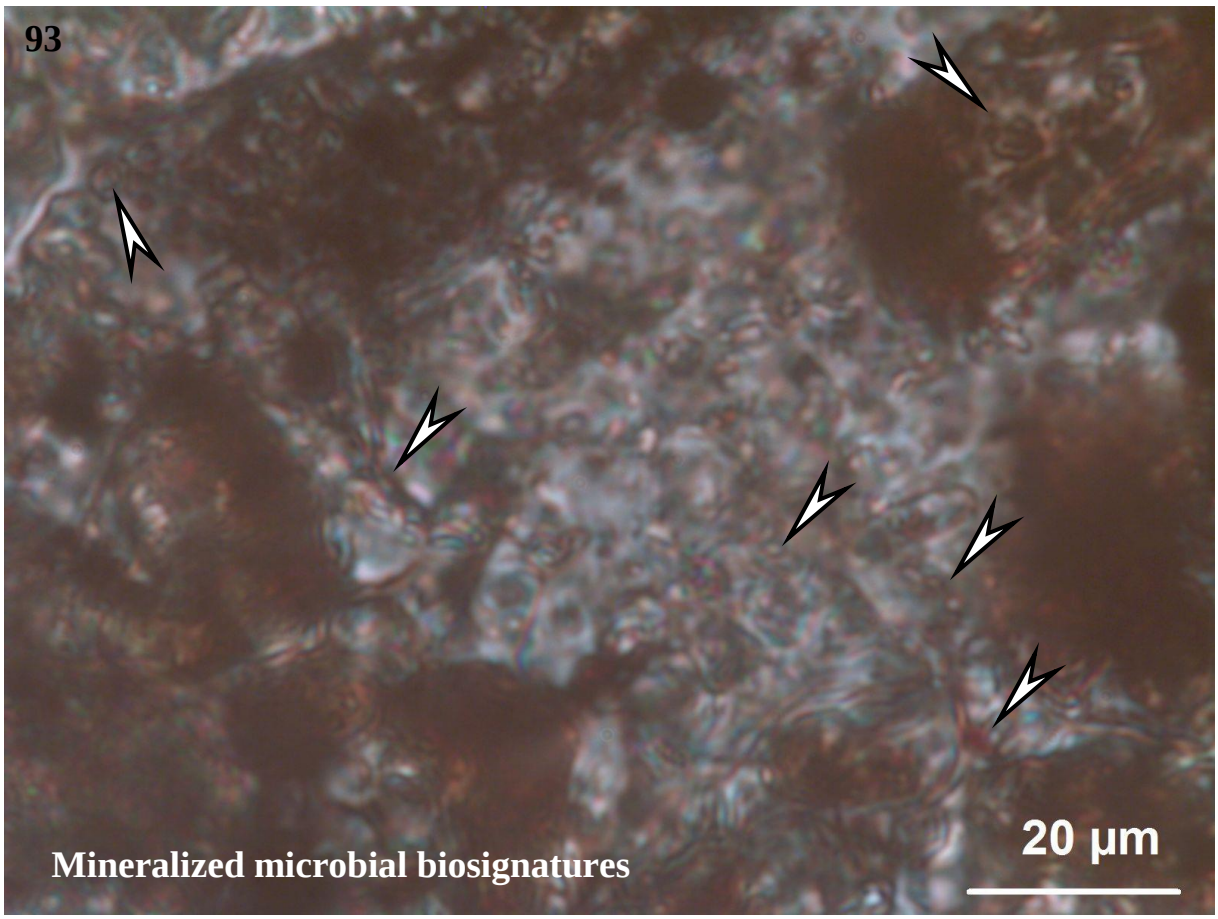
93
Mineralized microbial biosignatures
20 µm

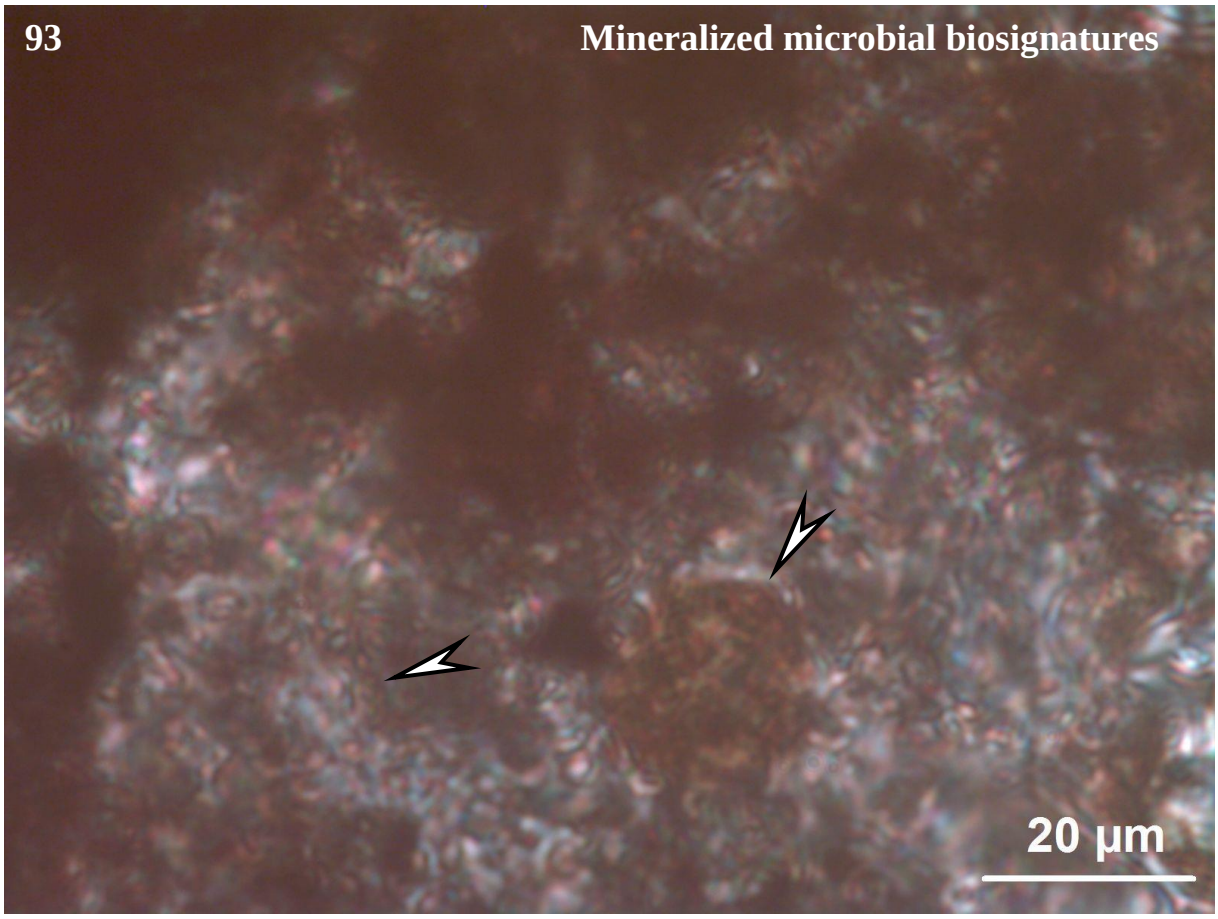
93
Mineralized microbial biosignatures
20 µm

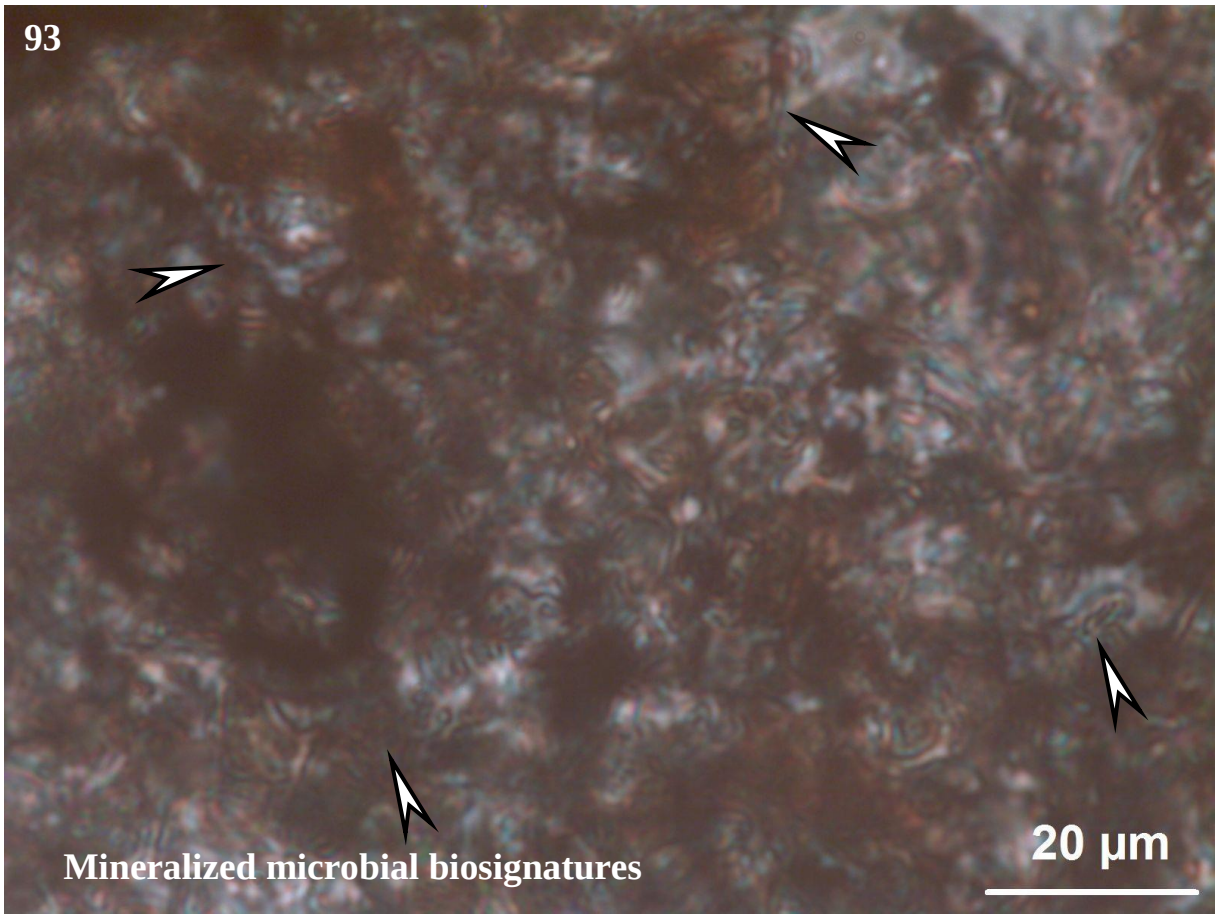
93
Mineralized microbial biosignatures
20 µm

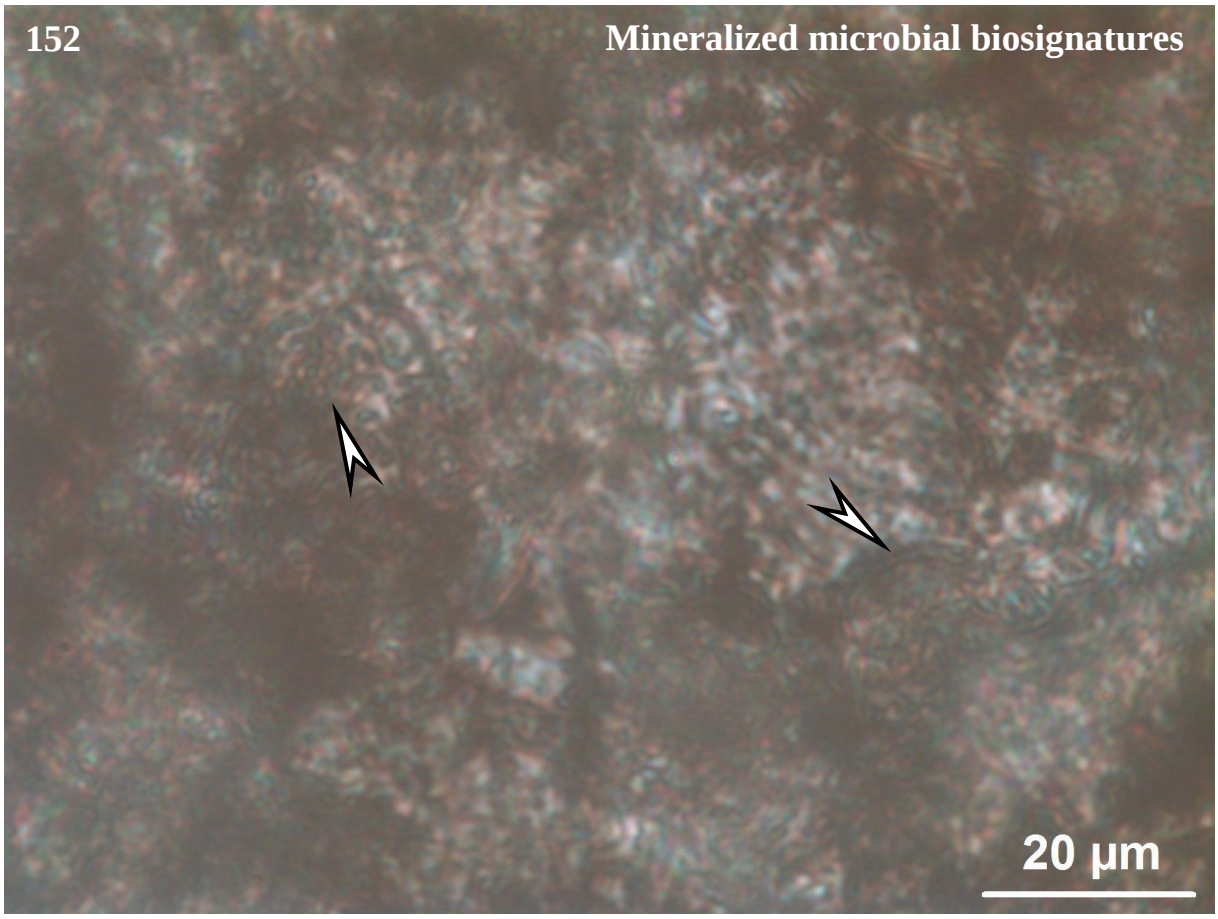

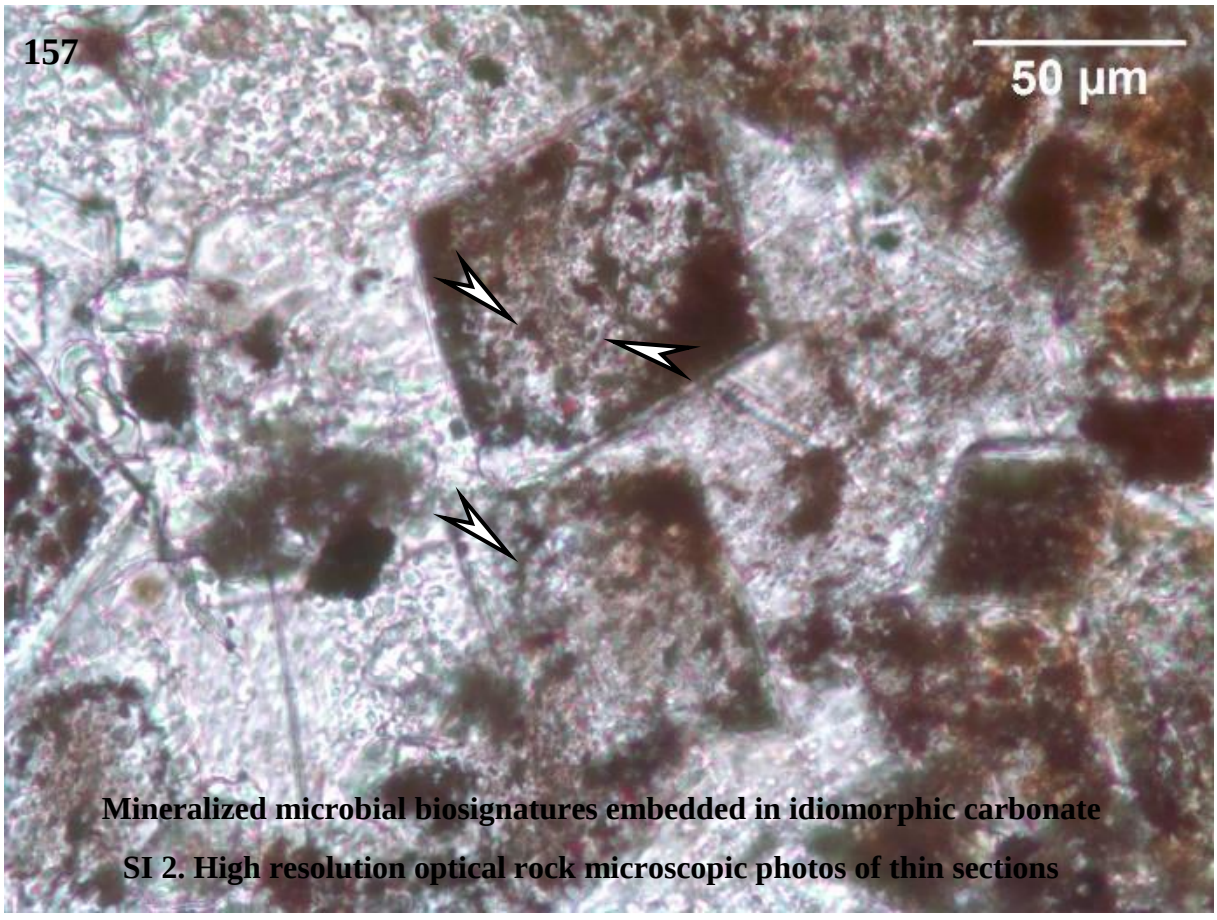

Mineralized microbial biosignatures embedded in idiomorphic carbonate

SI 2. High resolution optical rock microscopic photos of thin sections

SI 3. FTIR measurement of Urucum iron ore deposit

Mineral phase	**Reference***	**Sample ID cor**	88									86						93	
Nodule types (numbers) and profiles (letters)			B1	B2	B3	2A	A1	A2	A3	A4	1	Area1	1	2	4A	4B	C	3B	3
		Total No. of spectra→	6	7	9	7	8	4	6	9	12	6	16	7	8	6	8	5	6
Mineral phase	**Reference***	**Wavelength [cm^{-1}]**																	
dolomite	1	720. 888. 1425.		2					6										
siderite	1	740. 864. 1402													8	6			
rhodochrosite	1	729. 860. 1394		1		7		1	6	3								5	
montmorillonite		696. 798. 985s. 1633. 3623											2						
ferrihydrite	2	692. 878. 3400	3	2	3	2	3	2			2		16				3		
hematite	2	600. 1019	1	2	3			1	2	1					2	2	3	2	2
apatite	3	790. 1012. 1093	3	4				1	3	5		6		7	8	6	4	5	6
albite	4	798. 950. 1000	3			3		2									1		
quartz	4	701. 776. 1059		2	6	5	5	1		2	12	6	10	6			4	5	6
Organic compounds																			
C-N. CH deformation	5	1526	6	6	9	7	8												

C-N N-H amide II	5	1540-1550							3	12	6			2		8		6
amide I C=O. C-N. N_H	5	1632-1652	6	7	9	7	8		6	12	6			2		8		6
CO	5	2343	6	7	9	7	8	4	6	9	12	6	16	7	8	6	8	5	6
CO	5	2365	6	7	9	7	8	4	6	9	12	6	16	7	8	6	8	5	6
OH	6	3230-3700	6	7		7	8				12		16		8		8		6

Mineral phase	**Reference**	**Sample ID cor**	141			152			152					153A	153A			153B	157	157	157	157	157	157
Nodule types (numbers) and profiles (letters)			F1	F2	F3	D1	D2	D3	E1	E2	E3	E4	E5	6	G1	G2	G3	5	Area 1	Area 2	Area 3	2	2B	3
		Total No. of spectra→	**7**	9	14	8	9	6	4	9	8	10	5	14	9	7	12	12	12	7	9	8	11	10
		Wavelength [cm^{-1}]																						
dolomite	1	720. 888. 1425.								5	5		5	9		7								
ankerite		720. 884. 1405																				4		
siderite	1	740. 864. 1402				1	1		4	5	5	4		12		7	12							
rhodocrosite	1	729. 860. 1394																12	12	7	9		6	
ferrihydrite	2	692. 878. 3400										2		6			5					8	11	7
hematite	2	600. 1019	4	4	6	5	6	3		1		2		6			4	3			3			
aegirine	1	642. 730. 967	4	2	2												3							
apatite	3	790. 1012. 1093				7	9			3								5	5					

albite	4	798. 950. 1000	3	3										9	7									
quartz	4	701. 776. 1059	1		5			6		4	6	3	5	3	9			12	12	7	9	8	11	5
mica	1	653. 976										4												
Organic compounds																								
C-N. CH deformation	5	1526	7	9	14	8	9	6	4	9	8	10	5	16		7	12	12	12	7	9	8	8	10
C-N N-H amide II	5	1540-1550	7	9	14	8	9	6	4	9	8	10	5	16		7	12	12	12	7	9	8	8	10
amide I C=O. C-N. N_H	5	1632-1652	7	9	14	8	9	6	4	9	8	10	5			7	12	12	12	7	9	8	8	10
CO	5	2343	7	9	14	8	9	6	4	9	8	10	5	16		7	12	12	12	7	9	8	11	10
CO	5	2365	7	9	14	8		6	4	9	8	10	5	16		7	12	12	12	7	9	8	11	10
OH	6	3230-3700	7	9	14	8	9	6	4													8	11	10

For details see Fig. 6 (thin sections with signed nodule types and profiles)

References are marked by numbers, details in reference list. The number of spectra for minerals and organic materials in measuring area is added in columns. Total number of spectra: 330

References:

[1] RRUFF Database

[2] Glotch, T. D. & Rossman, G. R. (2009). Mid-infrared reflectance spectra and optical constants of six iron oxide/oxyhydroxide phases. *Icarus*, *204*(2). 663-671.

[3] Beasley, M. M., Bartelink, E. J., Taylor, L. & Miller, R. M. (2014). Comparison of transmission FTIR. ATR and DRIFT spectra: implications for assessment of bone bioapatite diagenesis. *Journal of Archaeological Science*, *46*. 16-22.

[4] Müller, C. M., Pejcic, B., Esteban, L., Delle Piane, C., Raven. M. & Mizaikoff, B. (2014). Infrared attenuated total reflectance spectroscopy: an innovative strategy for analyzing mineral components in energy relevant systems. *Scientific reports*, *4*. 6764.

[9] Parikh, S. J. & Chorover, J. (2006). ATR-FTIR spectroscopy reveals bond formation during bacterial adhesion to iron oxide. *Langmuir*, *22*(20). 8492-8500.

[5] Madejova, J. & Komadel, P. (2001). Baseline studies of the clay minerals society source clays: infrared methods. *Clays and clay minerals*, *49*(5). 410-432.

SI 4. FTIR dataset of samples

Urucum Banded Iron Formation

FTIR data

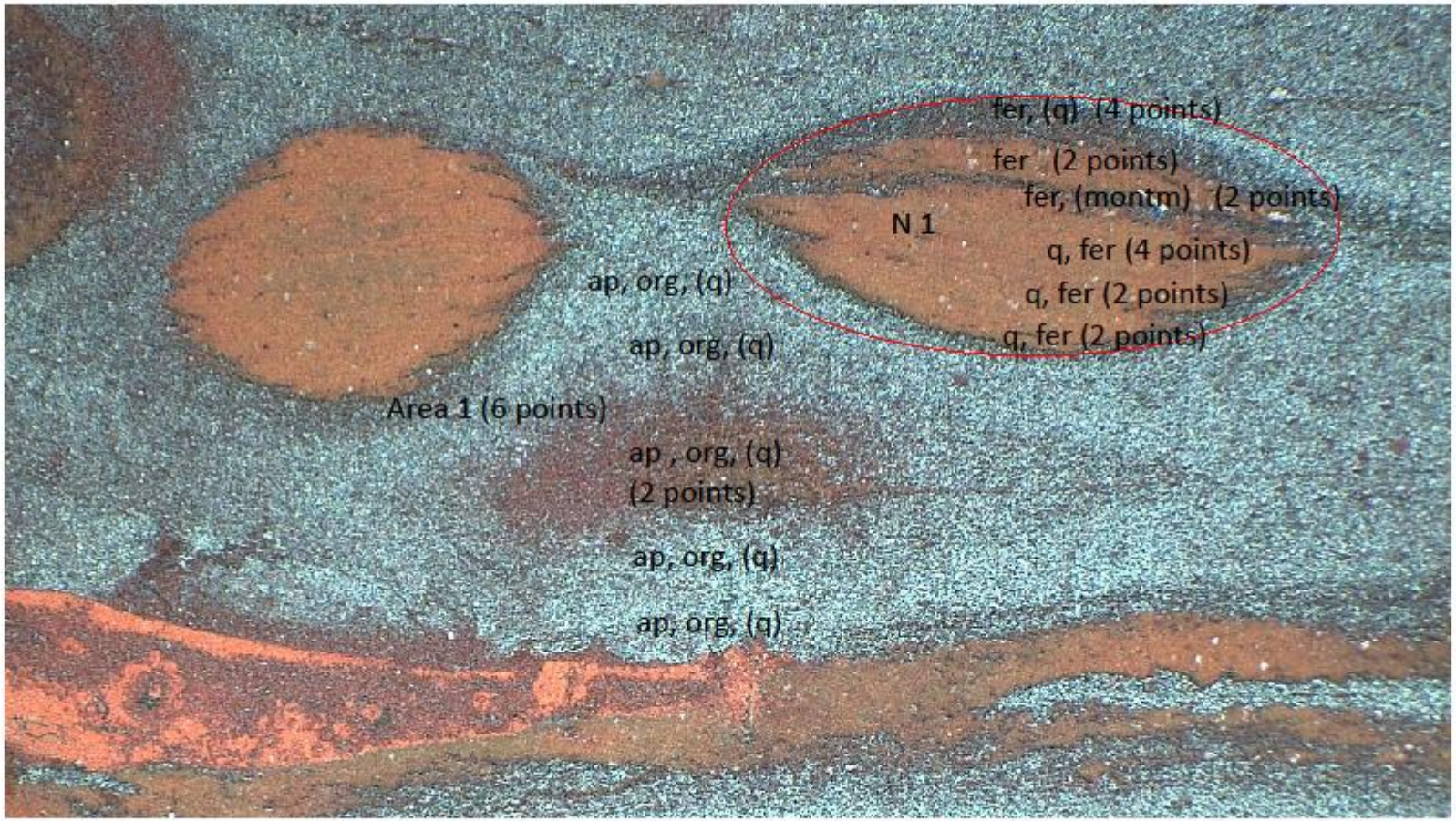

Cor86

Area 1

(6 points)

(q) = overlapping with apatite

Nodule 1
(16 points)

Cor86

2

(7 points)

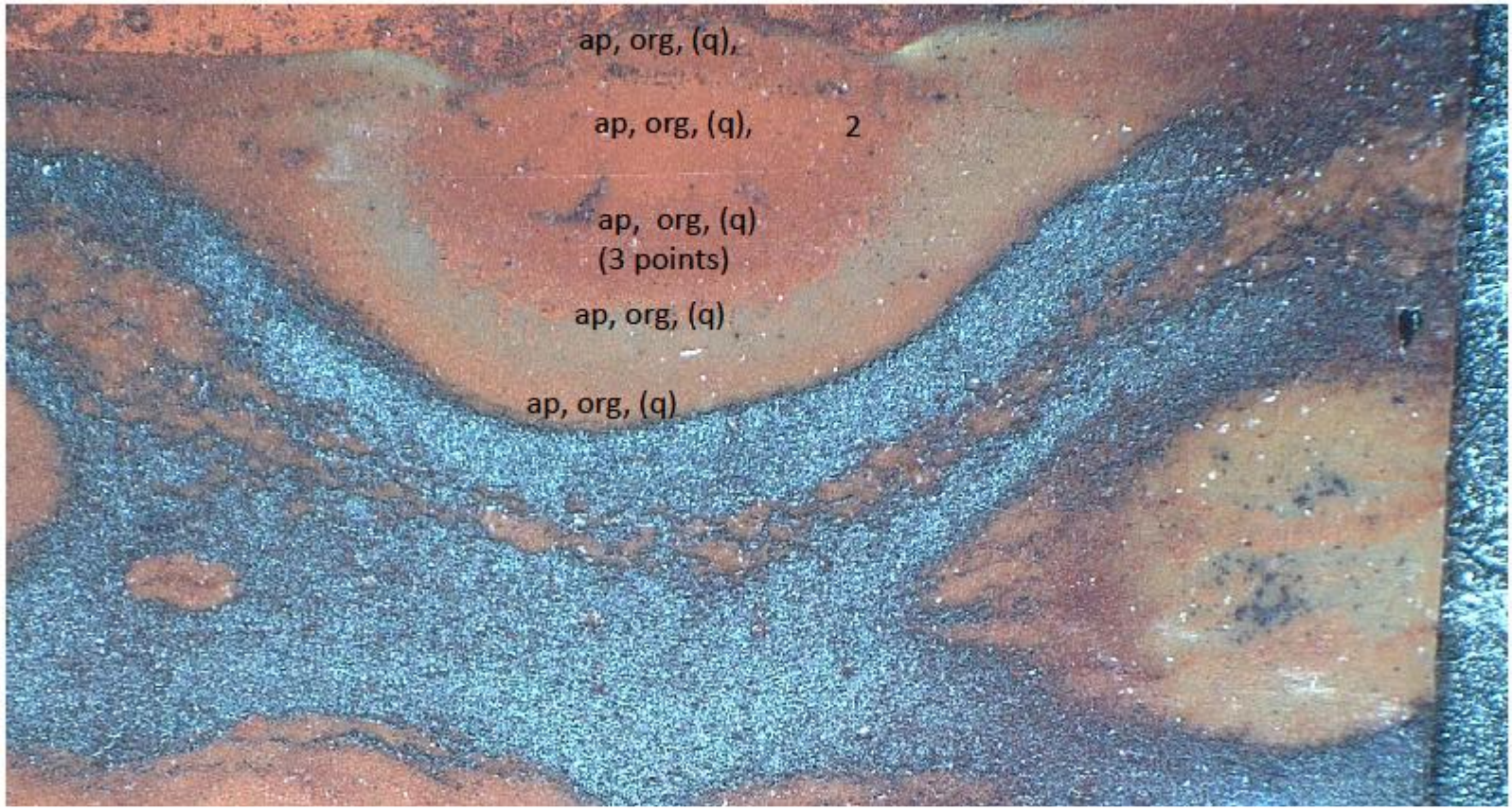

(q) = overlapping with apatite

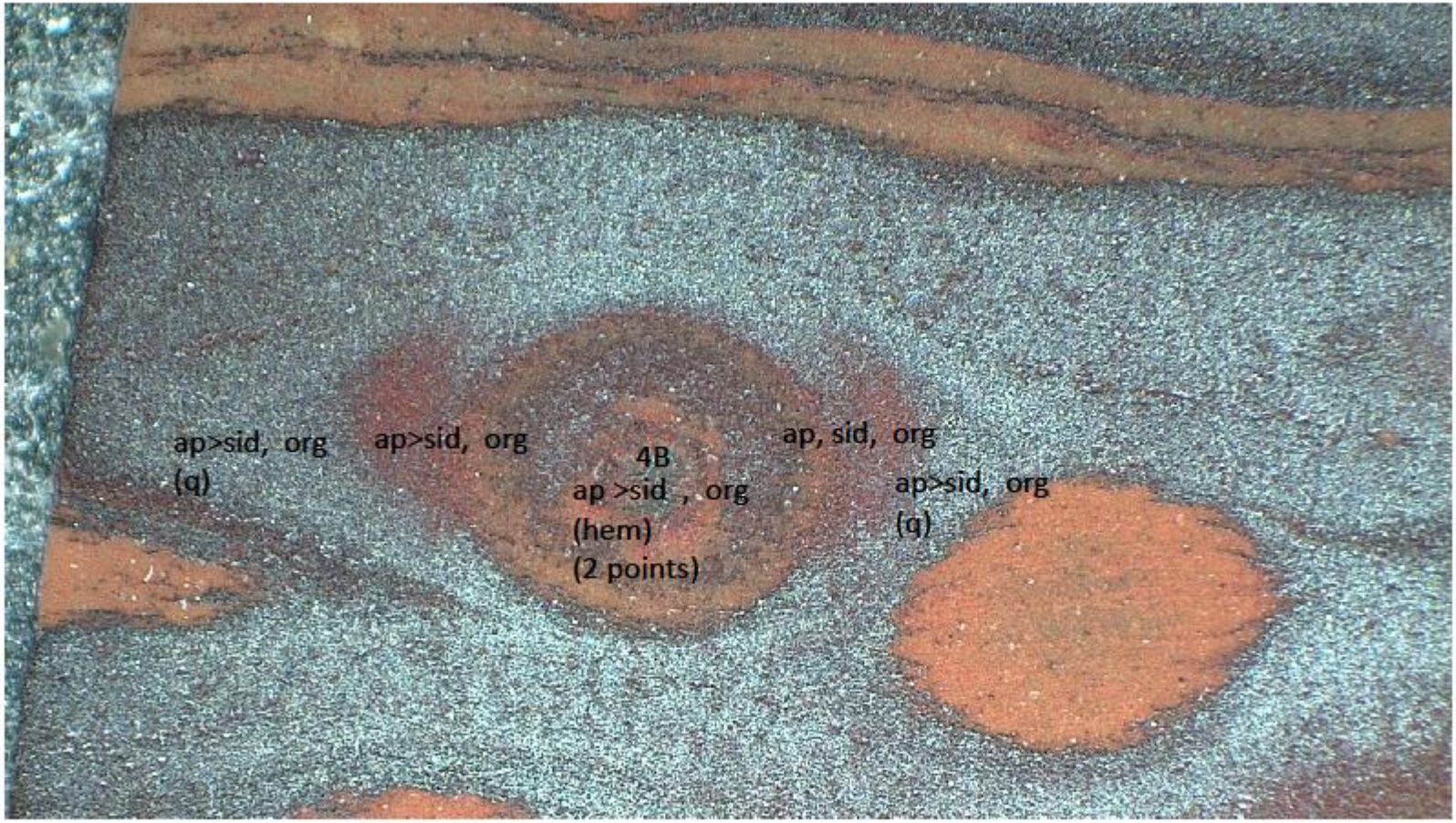

Cor86

4B

(6 points)

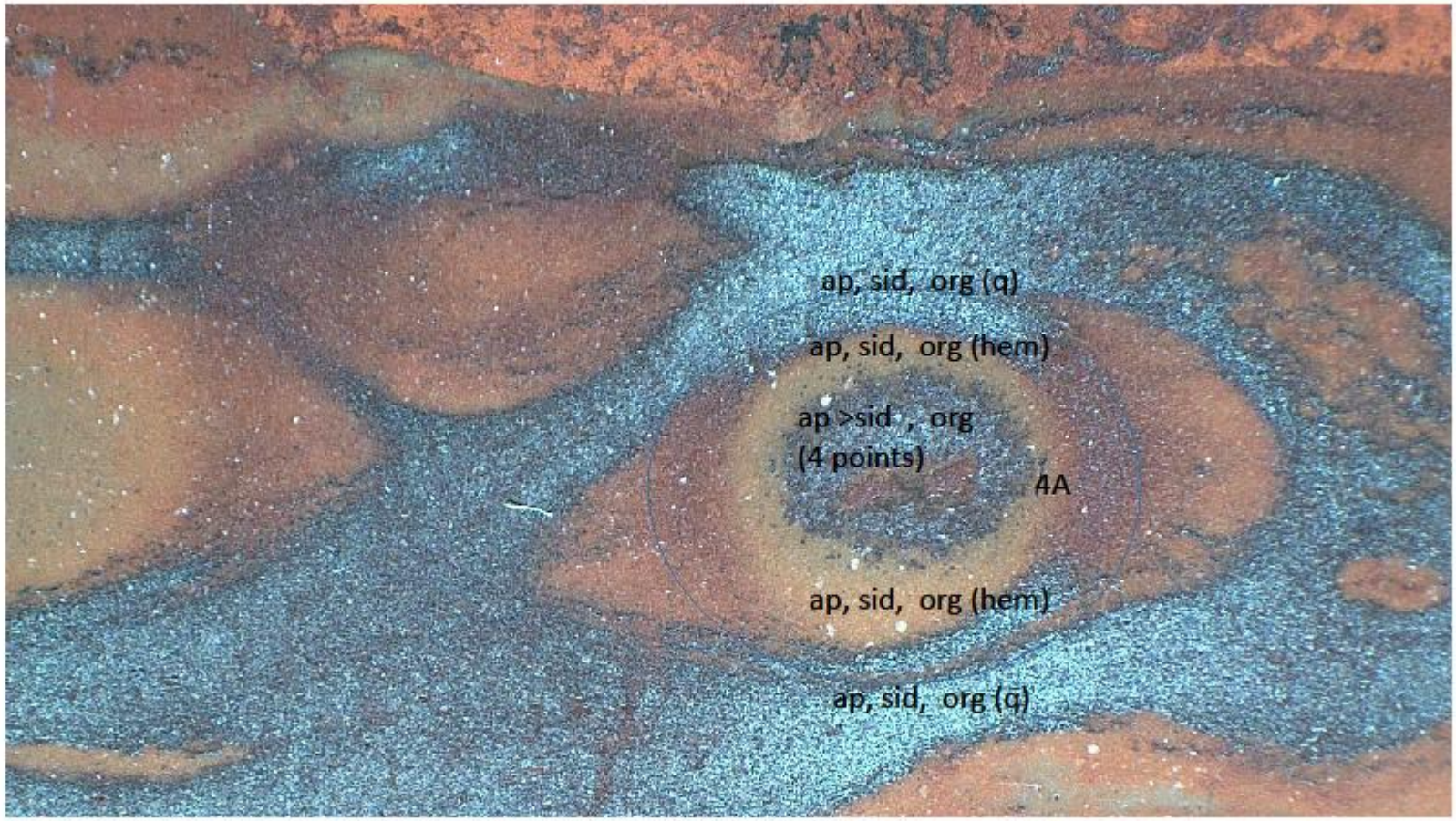

Cor86

4A

8 points

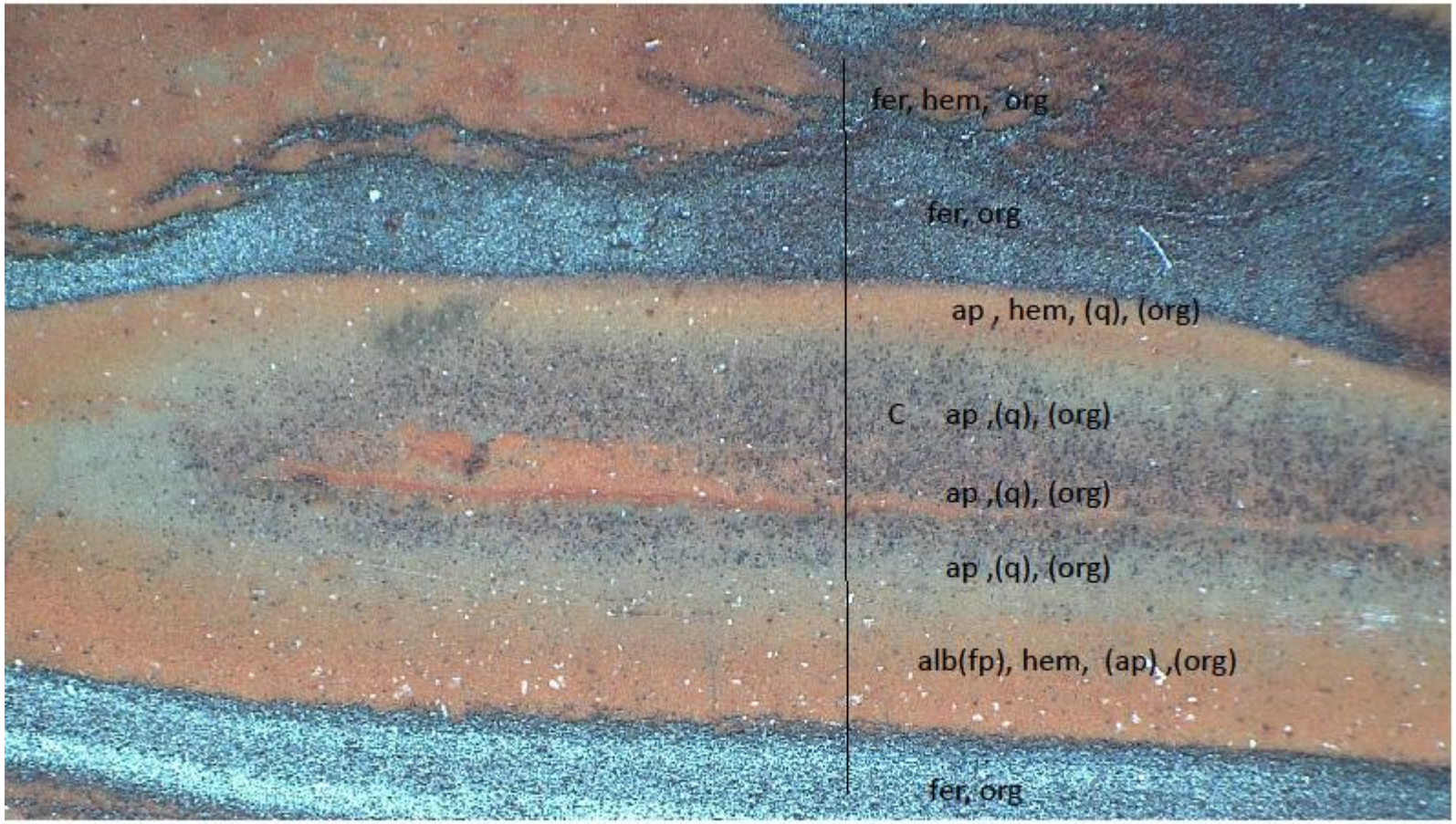

Cor86

C

(q): overlapping with apatite

(ap): overlapping with albite (fp)

(8 points)

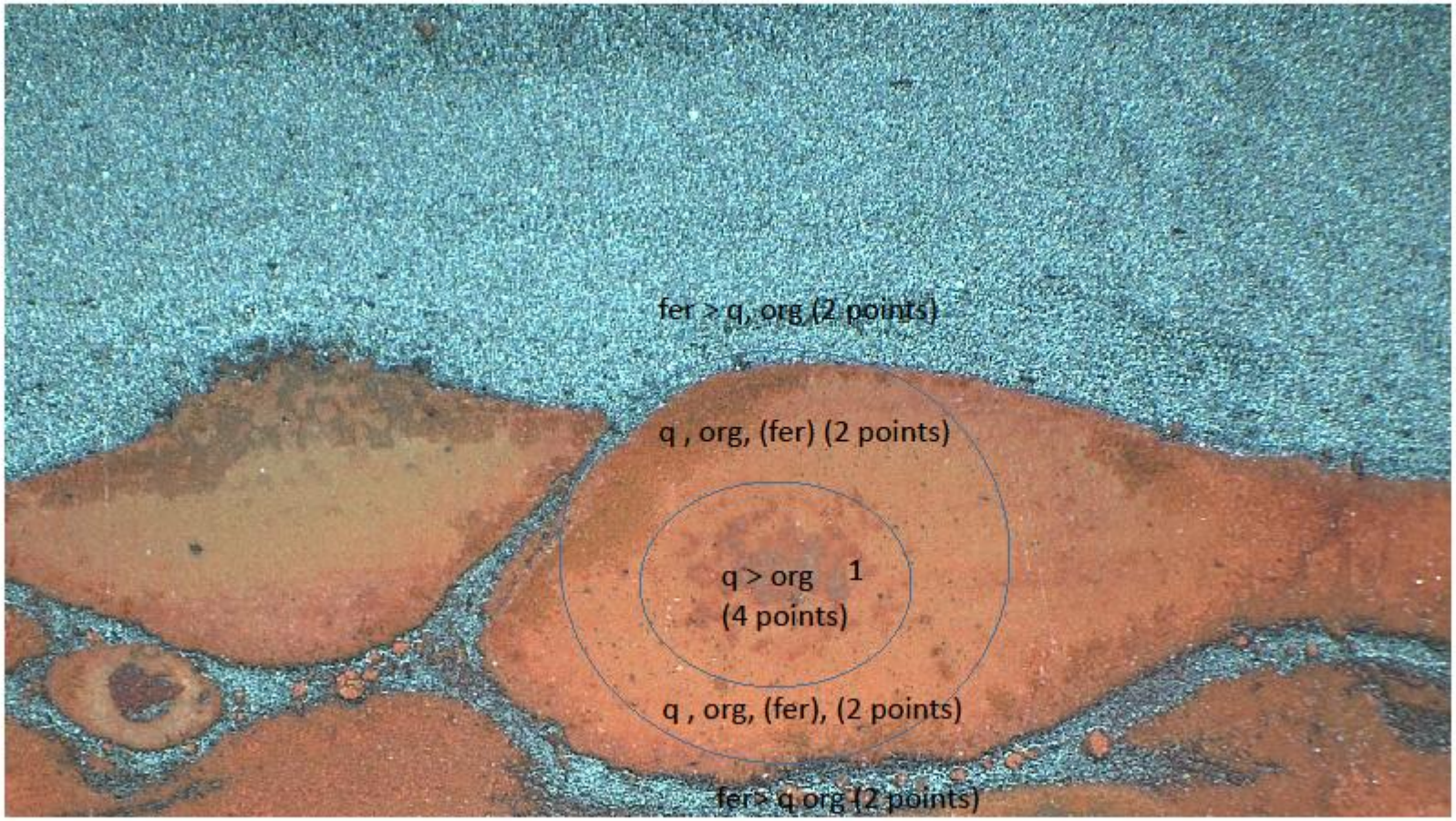

Cor88
1

(12 points)

(fer) = near to detection limit

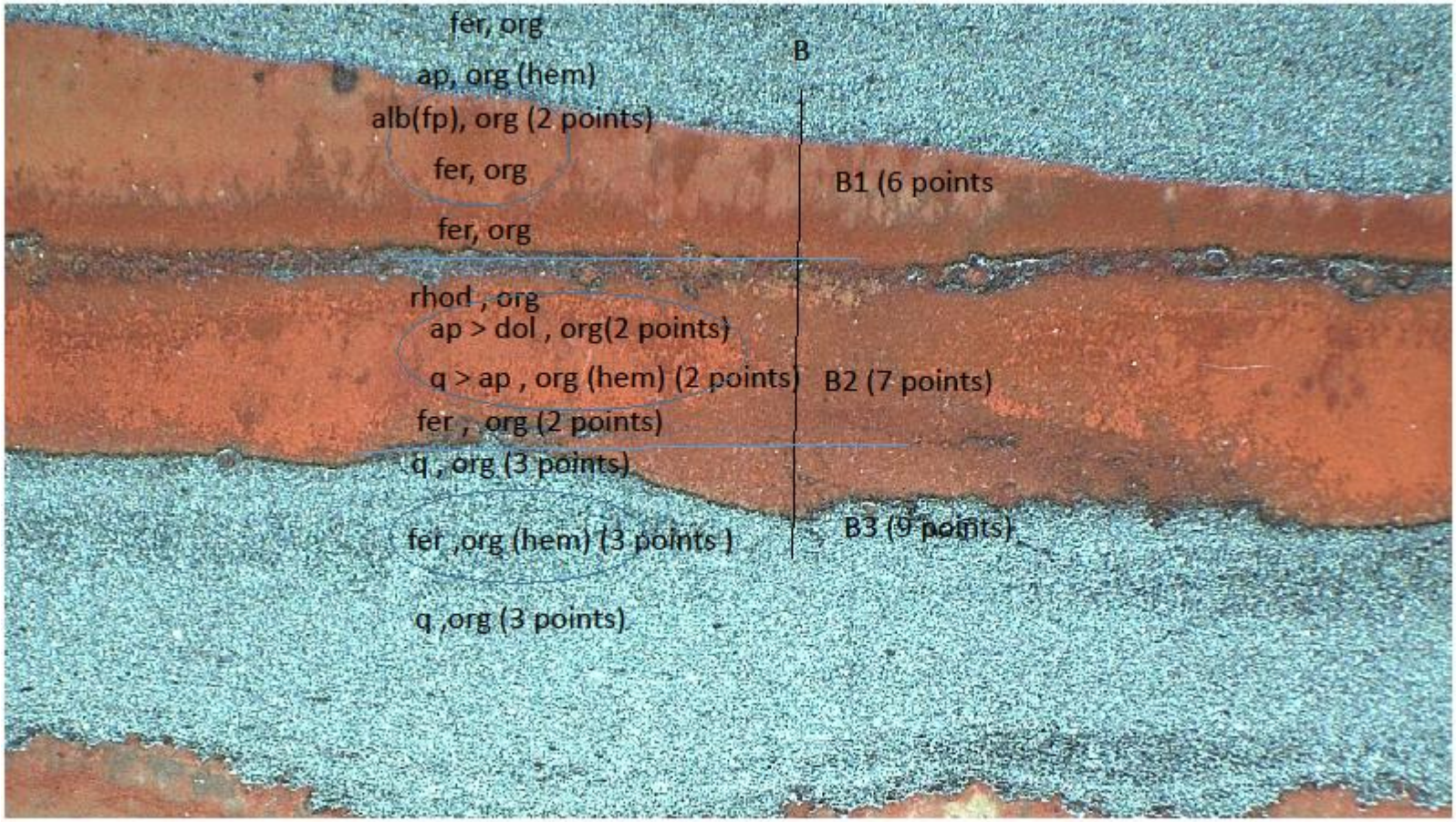

Cor88

B

(23 points)

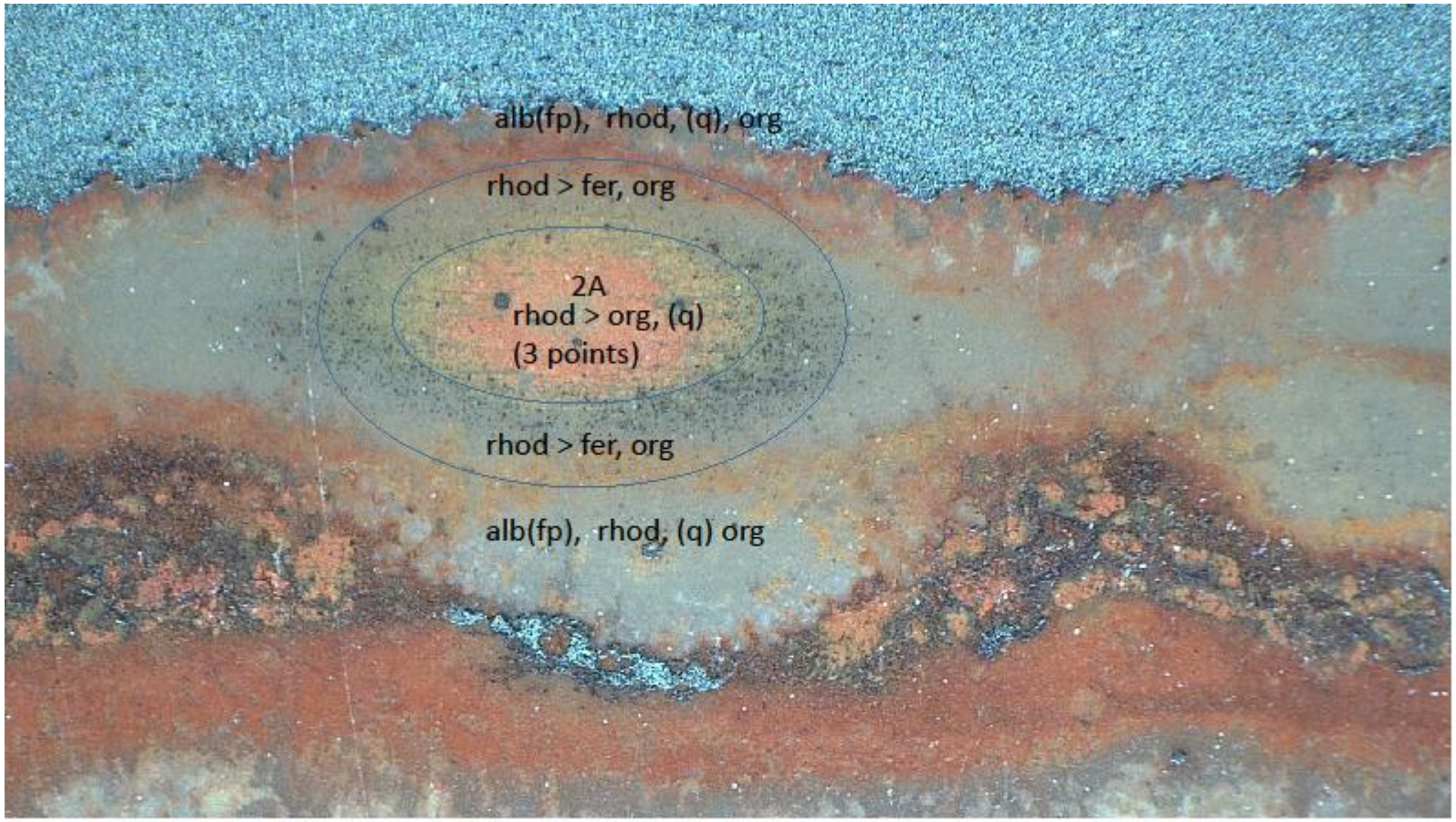

Cor88

2A

(7 points)

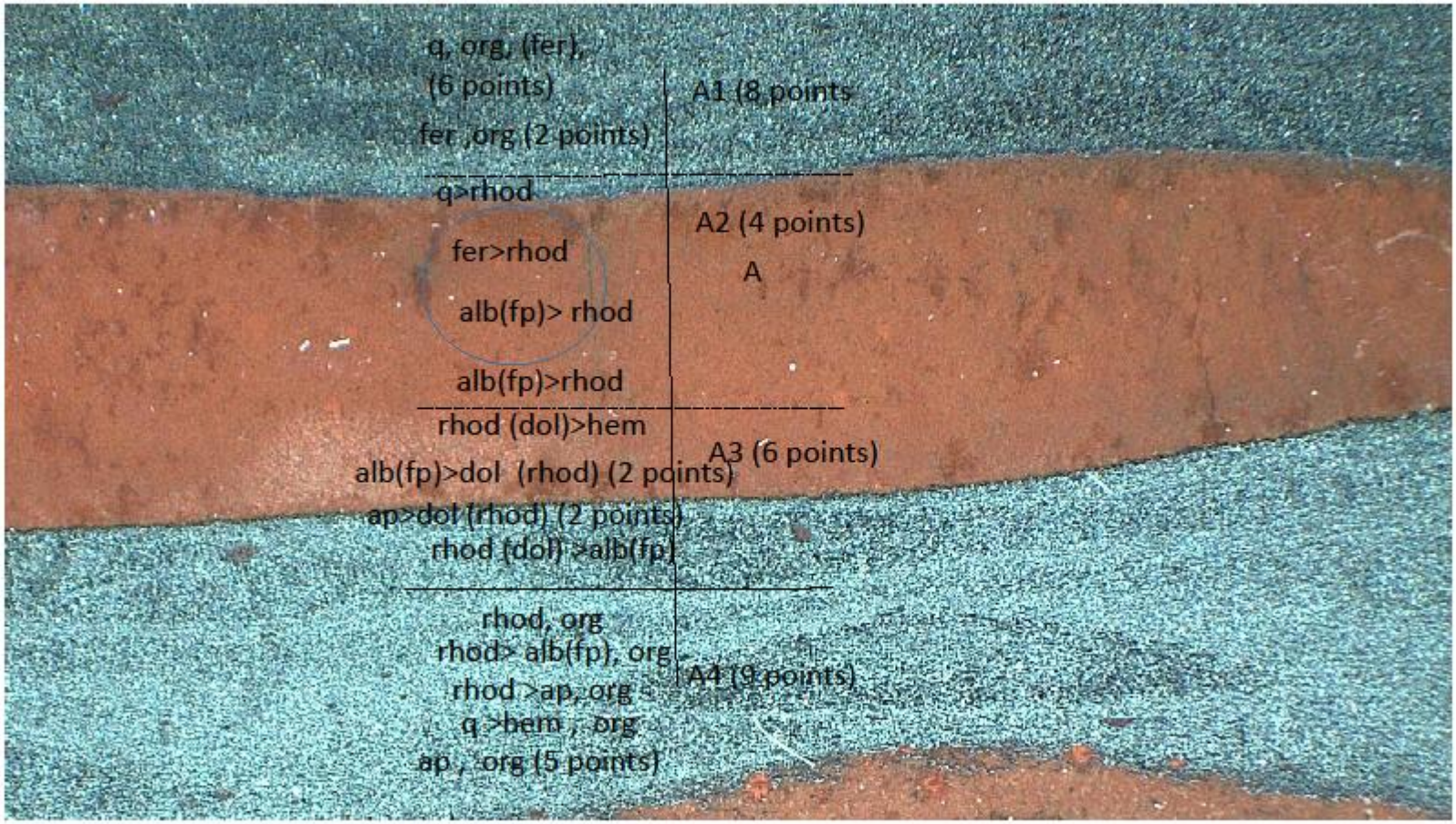

Cor88
A

(A1 fer) = overlapping with quartz
A 3 (rhod) = overlapping with dolomite

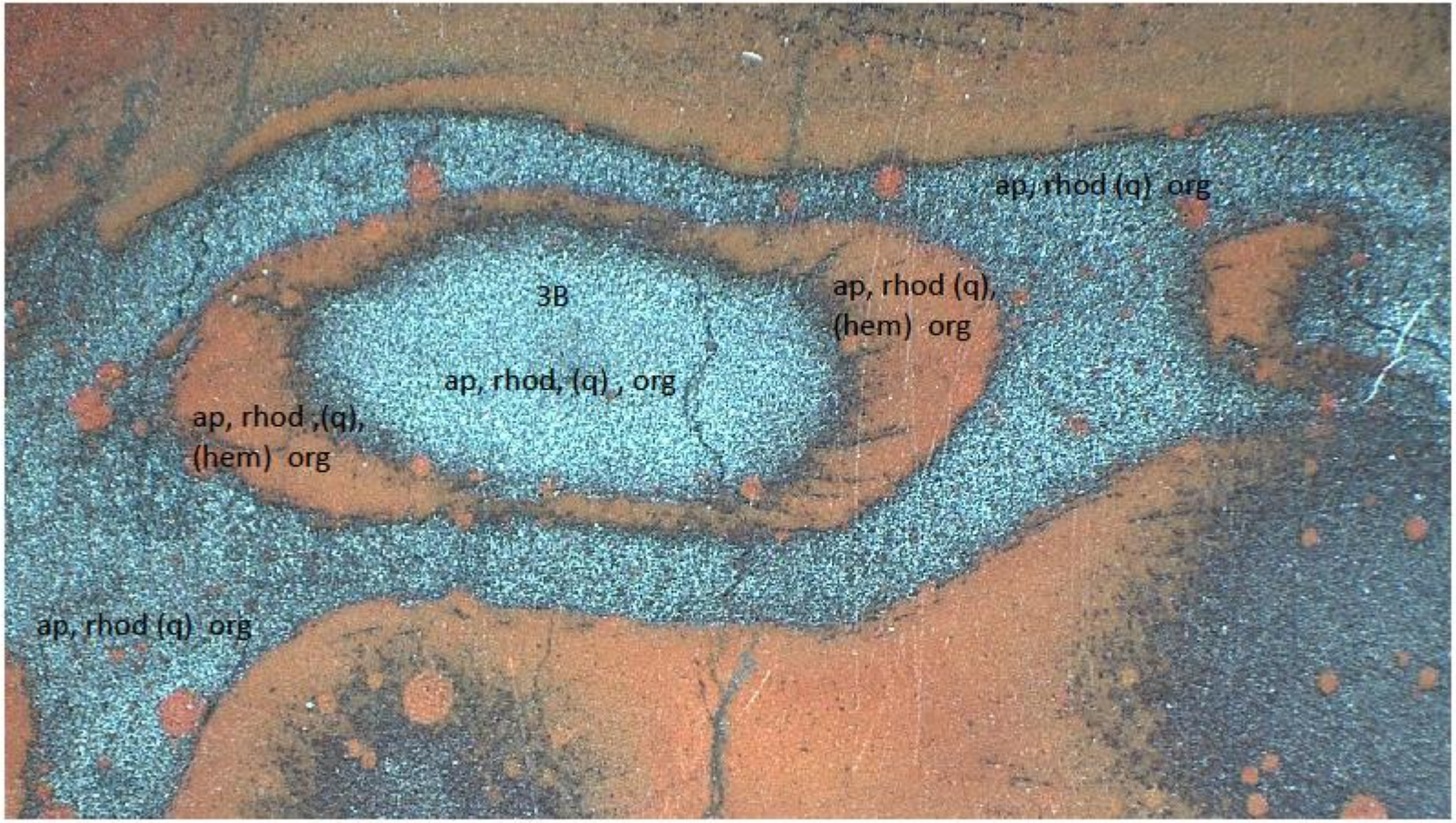

Cor93

3B

(5 points)

(q), (hem):
near to
detection limit

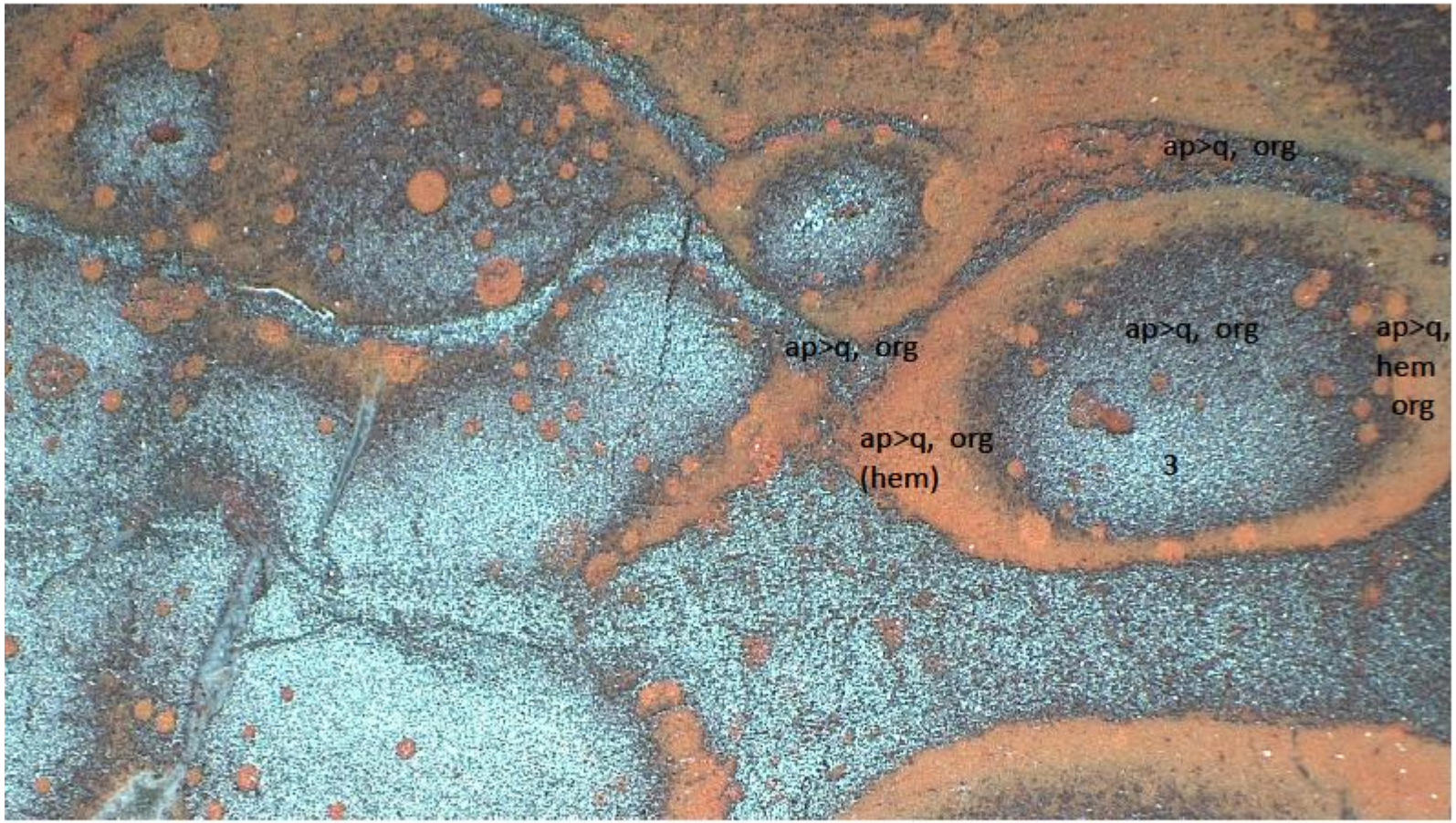

Cor93

3

(6 points)

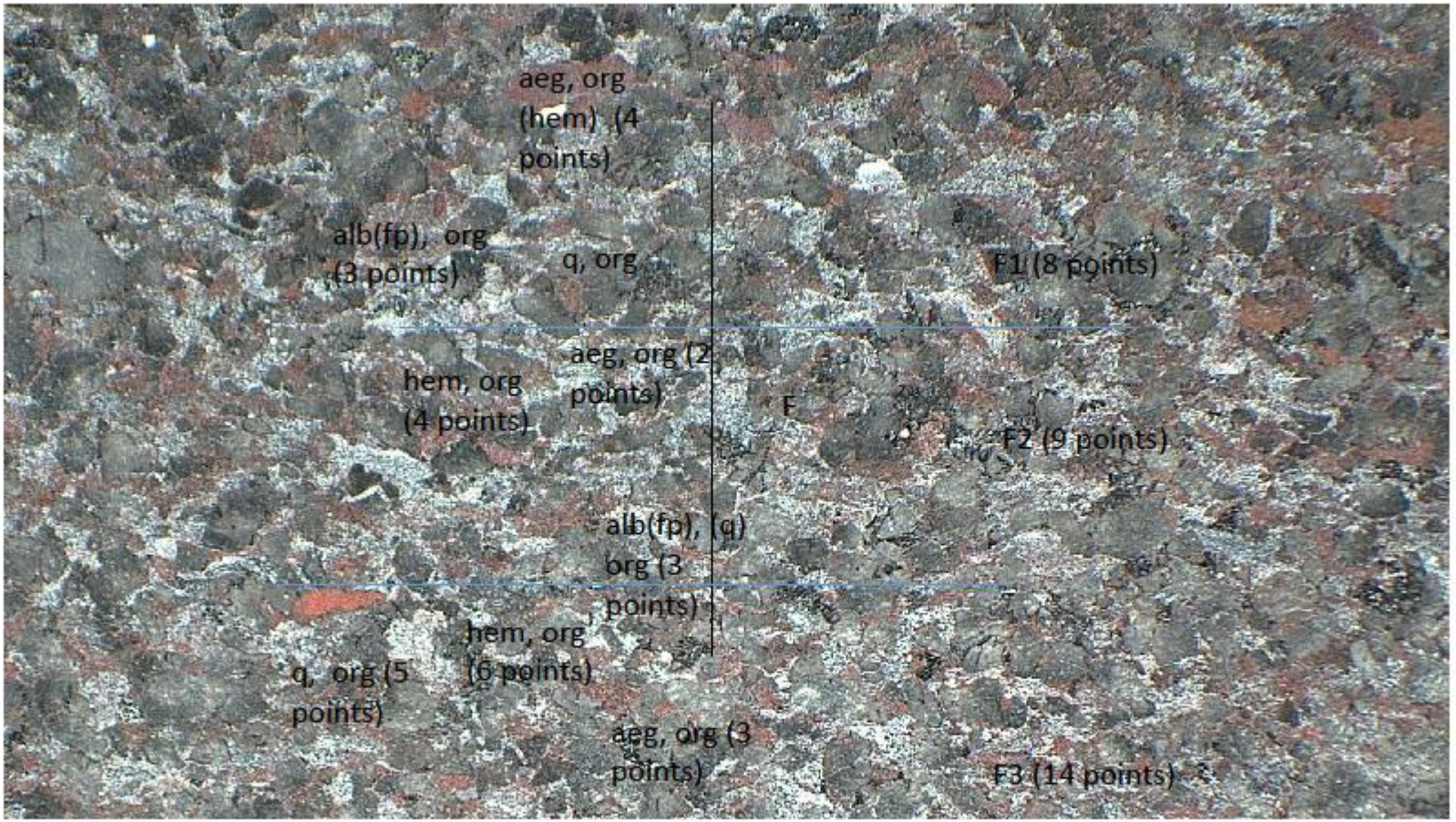

Cor141

F
(30 points)

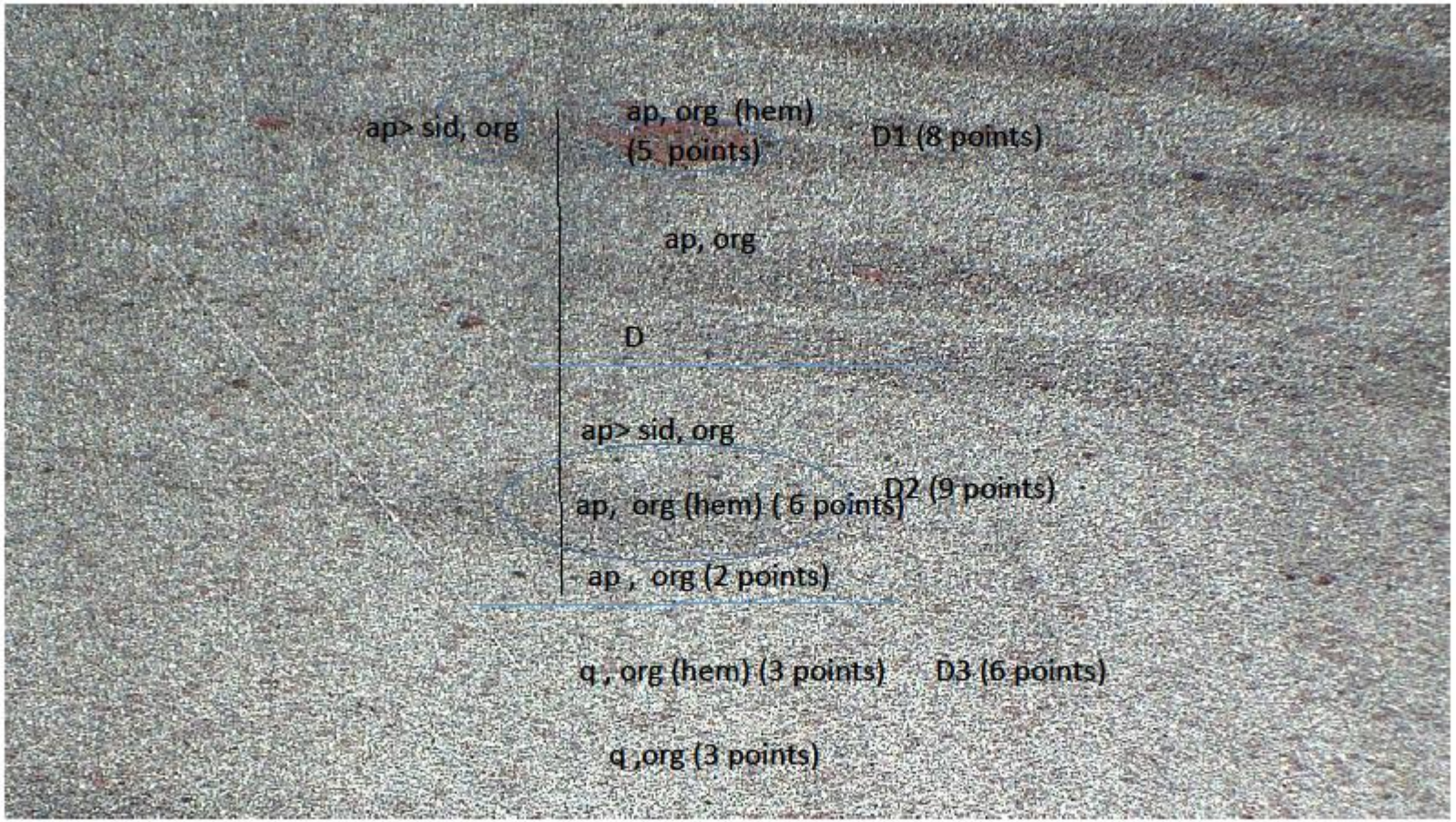

Cor152
D
(23 points)

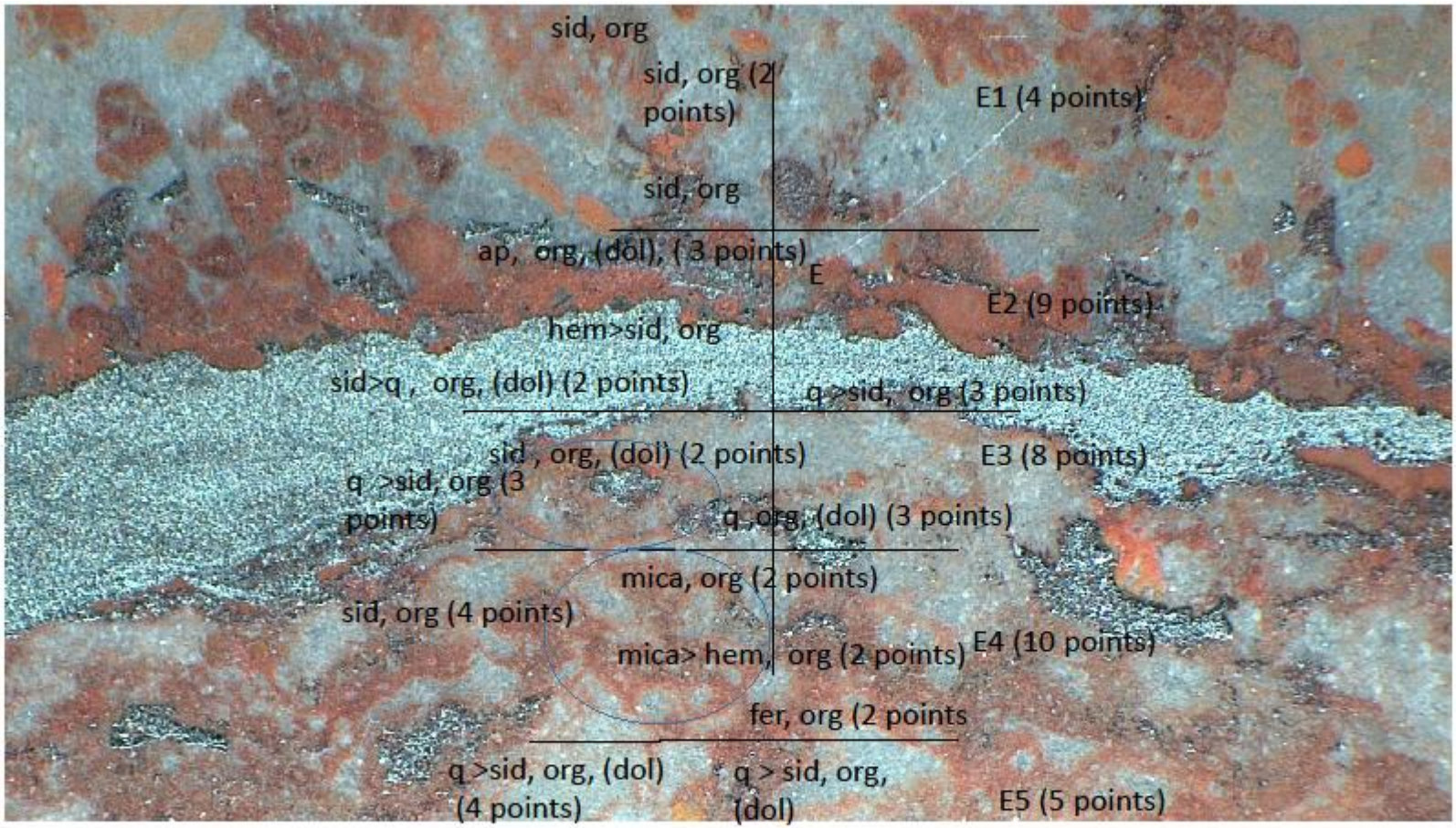

Cor152

E
(36 points)

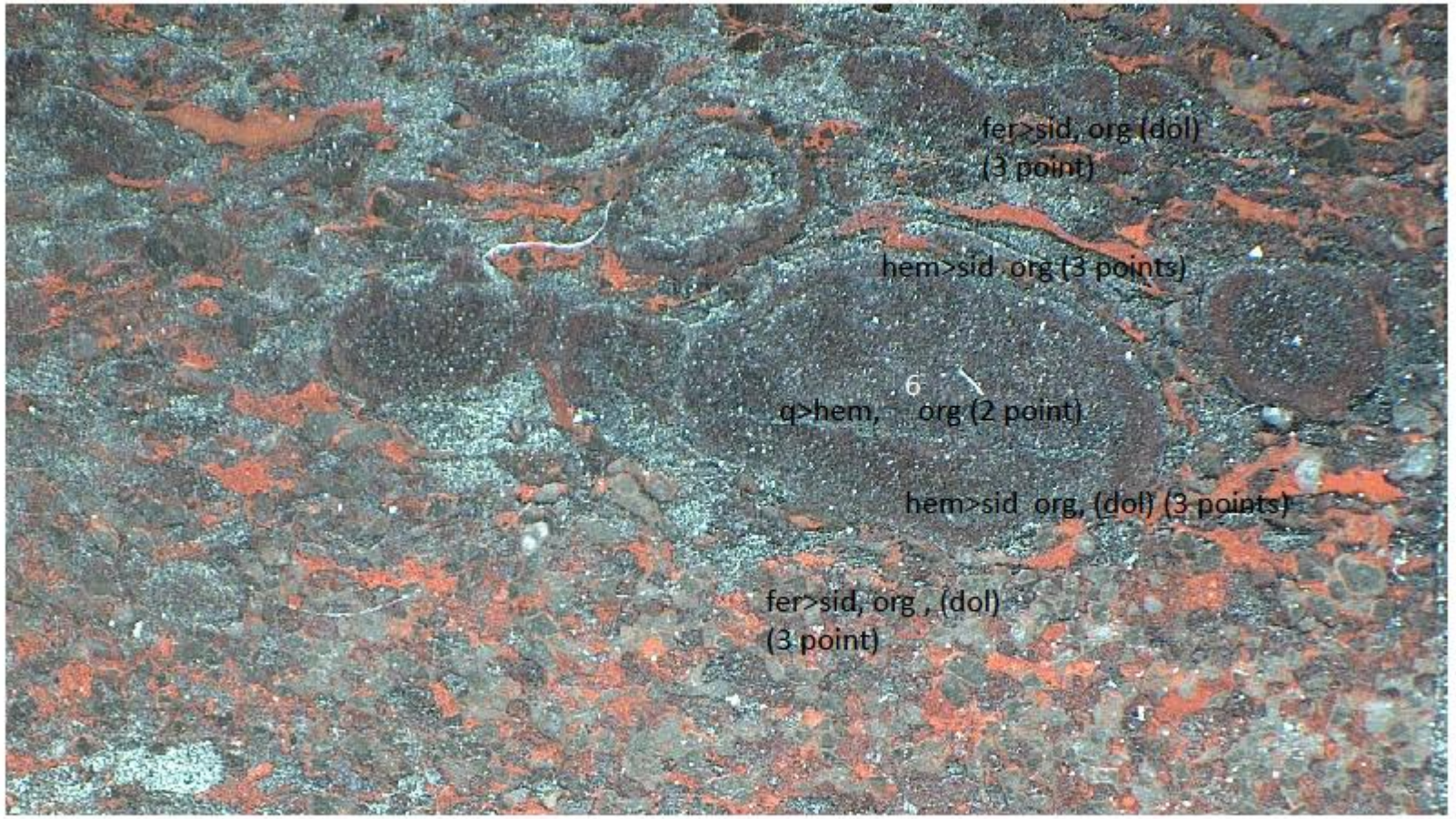

cor153A

6

(14 points)

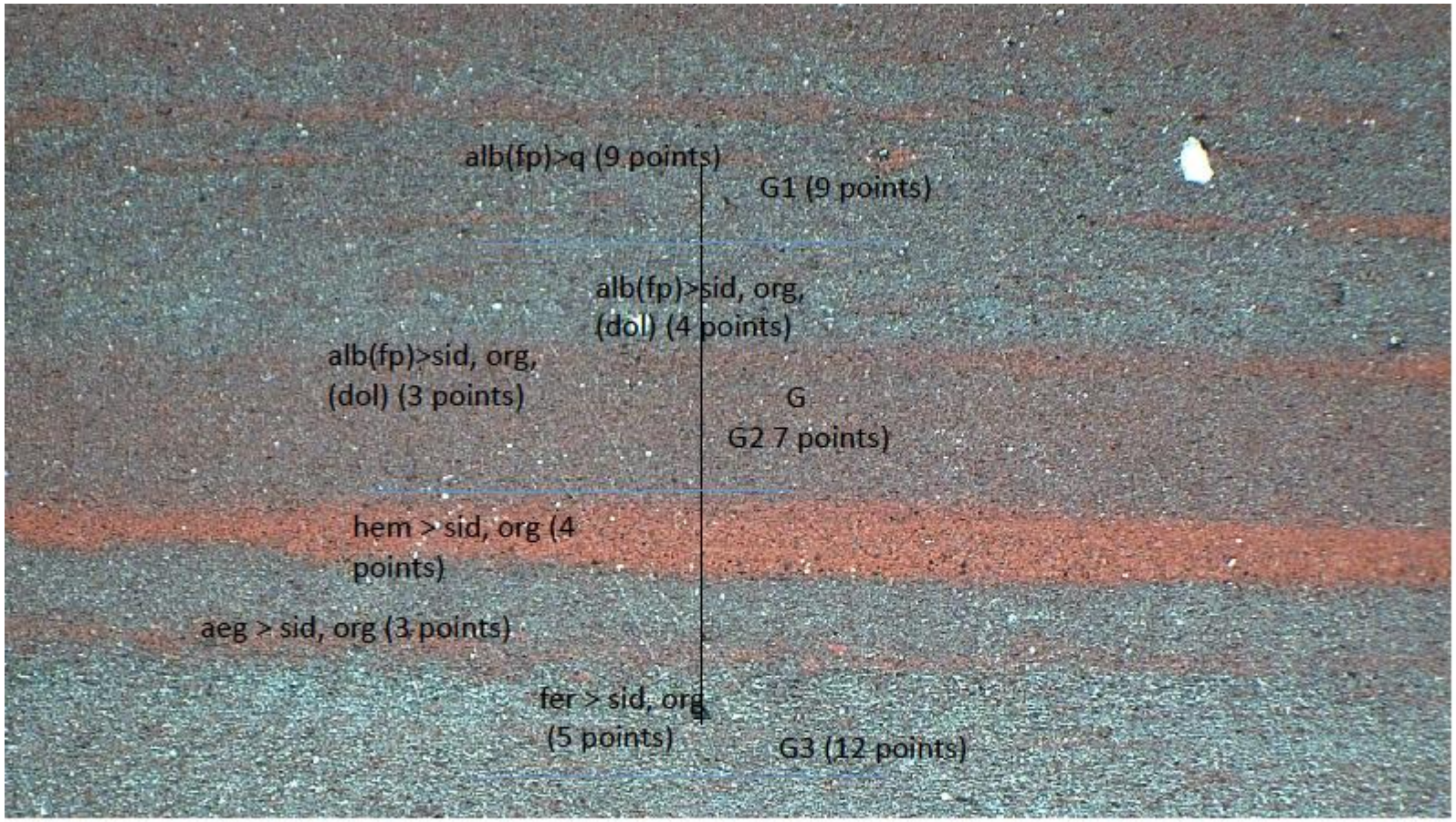

Cor153A

G
(28 points)

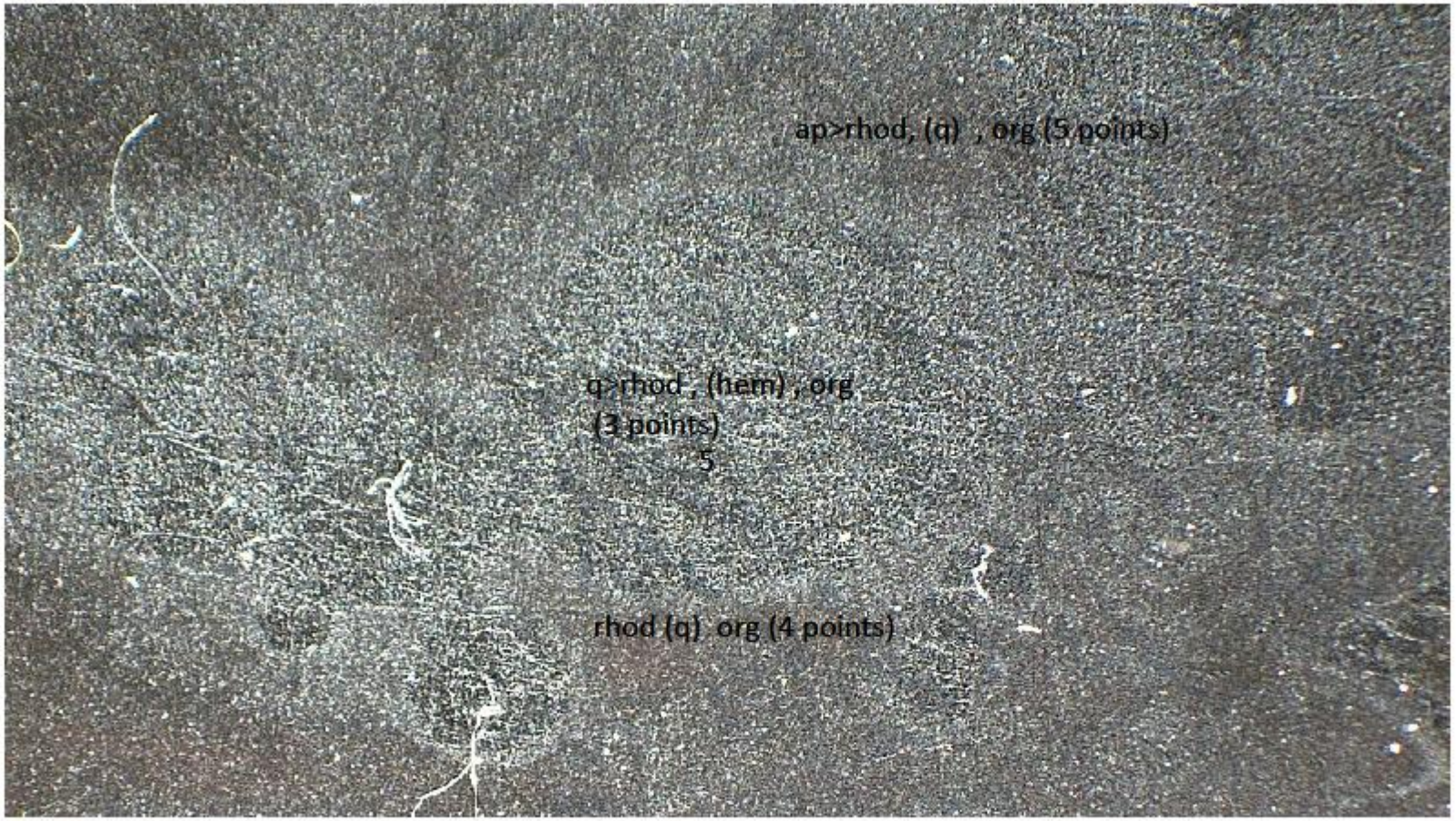

core153B

5

(12 points)

Cor157

Area 1

(12 points)

Nodule 2

(8 points)

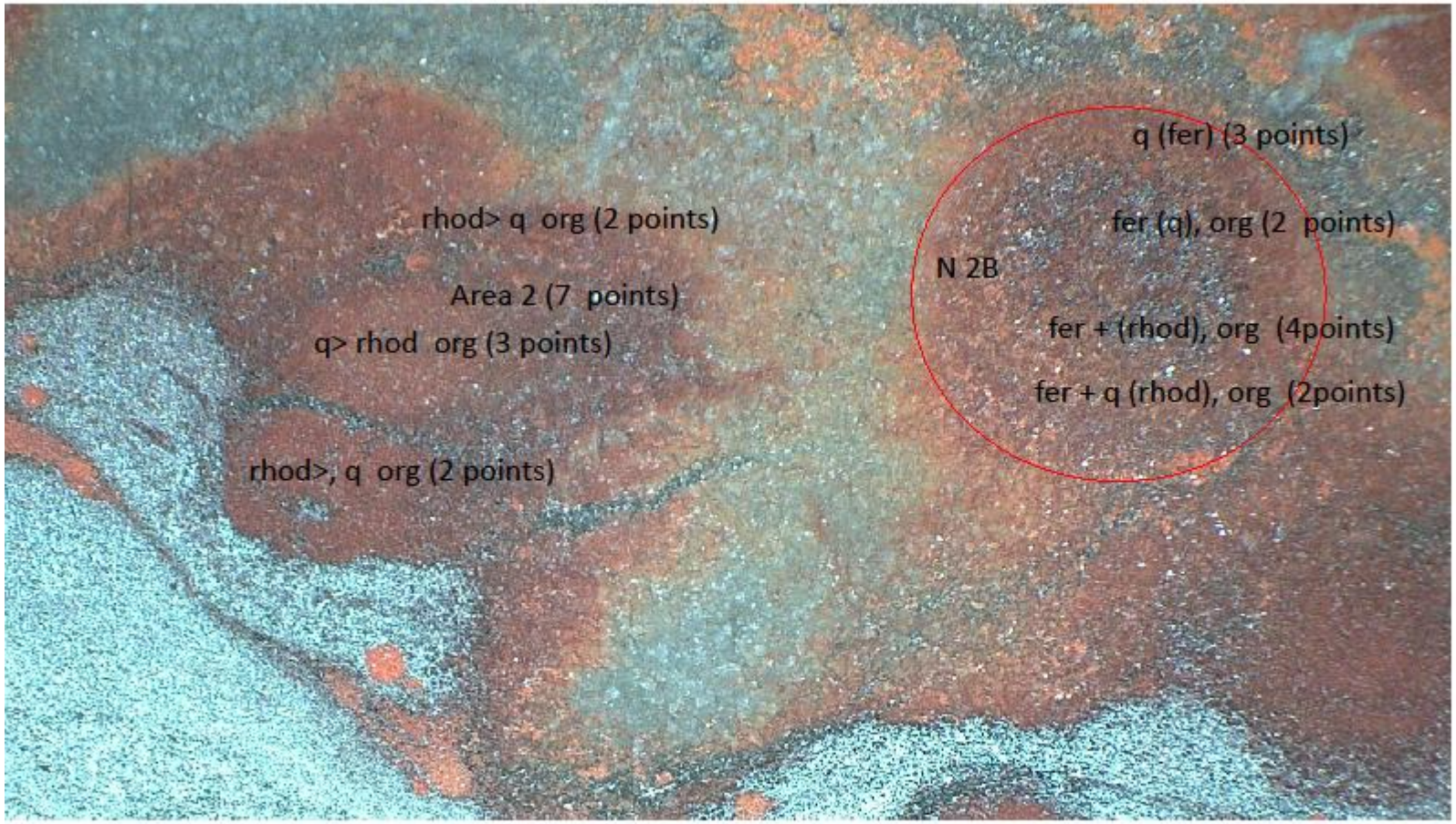

Cor157

Area 2 (7 points)

Nodule 2B
(11 points)

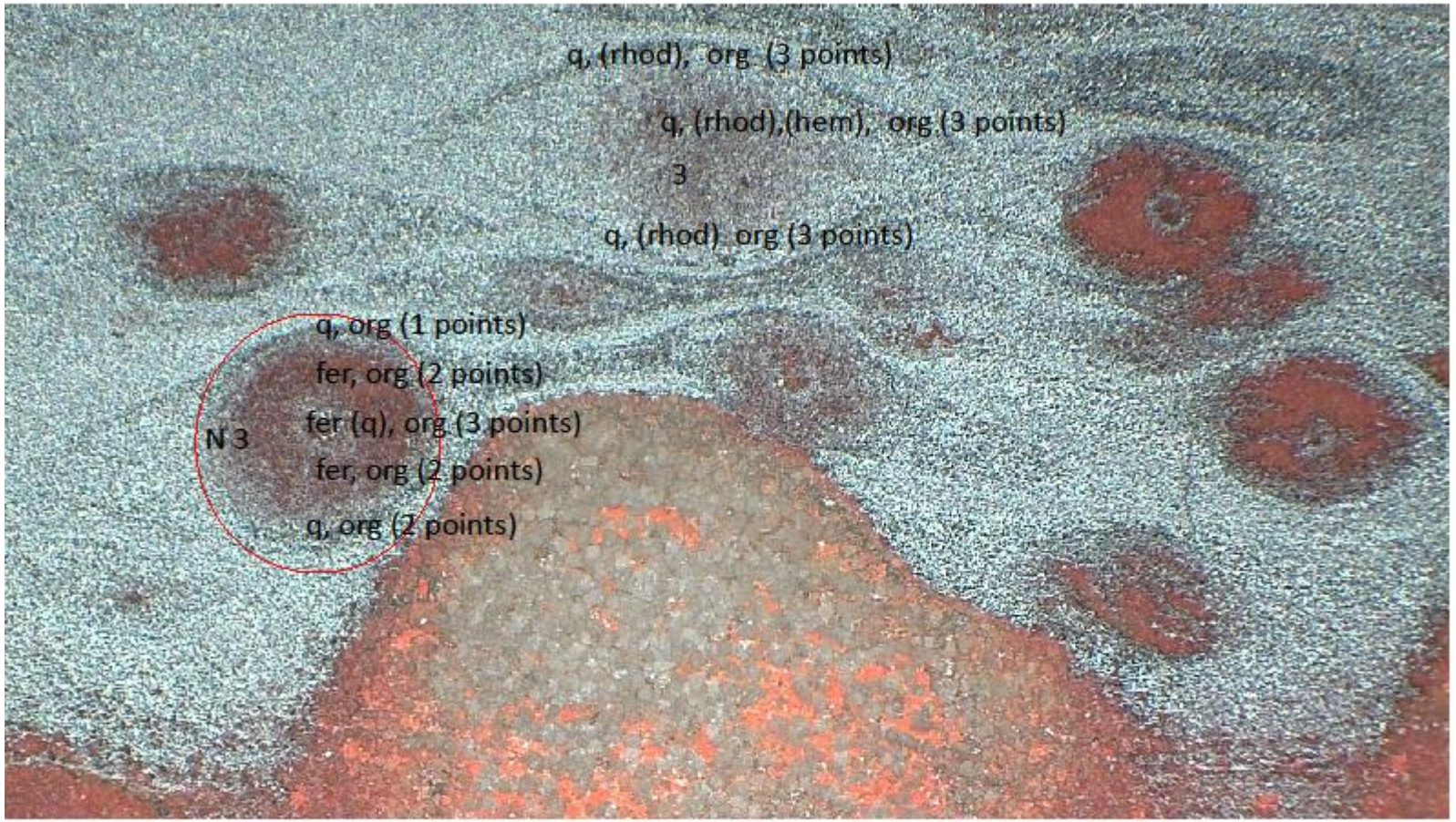

Cor157
Area 3
(9 points)

Nodule 3
(10 points)

SI 5. Raman spectroscopy dataset of samples

Sections. Raman vibration of minerals in sections of Urucum banded iron formation samples with references and detected types of organic materials. The number of spectra detected in samples are given in columns

Minerals Sample ID	Chemical formula	Bands	References	cor86_01	cor88_01	cor88_02	cor141_01	cor152_01	cor152_02	cor153_01
Section				**C**	**A**	**B**	**F**	**E**	**D**	**G**
No. Spectra				**701**	**566**	**550**	**701**	**701**	**601**	**701**
Mn mineral assemblage										
Oxides and hydroxide										
Todorokite	$Na_{0.2}Ca_{0.05}K_{0.02}Mn^{4+}{}_4Mn^{3+}{}_2O_{12}\bullet 3(H_2O)$	633s	RRUFF	0	0	0	1	0	0	0
Manjiroite	$Na(Mn^{4+}{}_7Mn^{3+})O_{16}$	641s	RRUFF	0	0	0	2	0	0	0
Manganite	$Mn^{3+}OOH$	387. 528. 552s. 621	RRUFF	0	0	0	245	0	0	2
Carbonates										
Rhodochrosite	$MnCO_3$	181. 287. 721. 1087	RRUFF	165	0	7	0	82	0	28
Kutnohorite	$CaMn^{2+}(CO_3)_2$	160. 286. 712. 1093	RRUFF	228	15	25	4	395	12	8
Mn-bearing calcite	$Mn\text{-}CaCO_3$	153. 275. 712 1017w. 1085	RRUFF	16	0	19	0	95	1	28
Sulfides										
Alabandite	MnS	(167m. 193m). (297s. 329s). 471	RRUFF	0	0	0	0	0	0	1
Fe mineral assemblage										
Oxides and hydroxides										
Hematite	Fe_2O_3	222. 290. 408. 490. 607 hem	Das and Hendry (2011)	586	565	548	417	381	600	690
Goethite	FeOOH	162. 243. 297s. 385s. 477. 545	Das and Hendry (2011)	0	0	0	3	0	0	4
Anatase	TiO_2 - $Fe_xTi_{(1-x)}O_{(2-x)}OH_x$	145s ®	RRUFF	0	0	0	0	0	0	204
Carbonates										

Siderite	$FeCO_3$	180. 282. 722. 1082	Das and Hendry (2011)	3	1	4	0	0	0	60
Ankerite	$CaFeCO_3$	179. 299. 721. 1095	RRUFF	49	213	202	0	0	0	0
Sulfides										
Marcasite	FeS_2	292w. 321. 386	RRUFF	0	0	0	0	0	0	2
Others										
Oxides – hyydroxides										
Quartz	SiO_2	125.207. 353. 393 w. 464s	RRUFF	432	89	90	307	20	8	15
Carbonates										
Dolomite	$CaMg(CO_3)_2$	179. 299. 721. 1097	RRUFF	0	0	0	0	0	0	2
Silicates										
Aegirine	$Ca_{0.75}Na_{0.25}Mg_{0.5}Fe^{2+}_{0.25}Fe^{3+}_{0.25}(Si_2O_6)$	185. 212 341. 365. 387. 541. 661. 970s. 1040	RRUFF	0	0	0	0	0	0	1
Albite	$NaAlSi_3O_8$	478s. 507s. 287m. 330. 244w. 207sh. 182m. 161 sh	RRUFF	0	0	0	141	15	1	27
Phosphates	$Ca_{0.75}Na_{0.25}Mg_{0.5}Fe^{2+}_{0.25}Fe^{3+}_{0.25}(Si_2O_6)$									
Apatite	$[(Ca_{10}(PO_4)_6(OH. F. Cl)_2]$	427. 587. 605 w. 965s. 1040 w. 1078 w	RRUFF	6	8	28	16	2	3	15
Organic material			Orange et al. (1996); Chen et al. (2007); Jehlicka et al. (2009); Okolo et al. (2015)							
graphite		1600	C=C	0	0	0	5	15	0	0
org1		1330. 1606. 1754. 1824	CH3. fluerene. carboxyls. C=O in oils	3	1	1	55	67	3	70
org2		1245. 1330. 1600	CH2 scissors mode CH3. C=C fluerene	11	13	32	56	148	14	72
org3		1326. 1717	CH3 aliphatic. carboxyls	33	4	5	2	43	8	24
org4		1412. 1727	CH3/CH2. carboxyls	3	4	4	1	0	0	16
org5		1267. 1332. 1363. 1484. 1606. 1847	CH2 scissors mode. CH aliphatic band. CH3. CH2/CH3 vibrational mode. C=C in fuerene C=O in oils	15	13	4	34	26	10	12
org6		1387. 1522. 1607	CH3. C=C stretching of polyene chain. aromatic C=C in fluerene	0	0	0	1	2	0	0
org7		1336. 1610	CH3. aromatic C=C in fluerene	1	0	0	0	0	0	3

Nodules. Raman vibration of minerals in the nodules of Urucum banded iron formation samples with references and detected types of organic materials. The number of spectra detected in samples are described in columns.

Minerals Sample ID	Chemical formula	Bands	References	cor86				cor88		cor93		cor153 A	cor153 B	cor157		
No. Spectra				**101**	**138**	**126**	**126**	**146**	**101**	**41**	**168**	**60**	**101**	**141**	**118**	**157**
Mn mineral assemblage			**Nodule type**	**1**	**2**	**4A**	**4B**	**1**	**2A**	**3**	**3B**	**6**	**5**	**2**	**2B**	**3**
Oxides and hydroxide																
Pyrolusite	$Mn^{4+}O_2$	219w. 291w. 404w. 533s. 655s. 756w	Sepulveda et al. (2015)	0	0	0	0	0	0	0	0	0	26	26	26	26
Jacobsite	$Mn^{2+}_{0.6}Fe^{2+}_{0.3}Mg_{0.1}Fe^{3+}_{1.5}Mn^{3+}_{0.5}O_4$	620s	RRUFF	0	0	0	0	0	0	0	0	30	0	9	9	9
Manjiroite	$Na(Mn^{4+}_7Mn^{3+})O_{16}$	641s	RRUFF	0	0	0	0	0	0	0	0	60	22	22	22	22
Carbonates																
Rhodochrosite	$MnCO_3$	181. 287. 721. 1087	RRUFF	23	33	28	29	8	4	0	11	37	25	21	20	20
Kutnohorite	$CaMn^{2+}(CO_3)_2$	160. 286. 712. 1093	RRUFF	50	80	55	49	84	60	16	6	0	0	64	47	66
Mn-bearing calcite	Mn-$CaCO_3$	153. 275. 712 1017w. 1085	RRUFF	7	7	4	5	2	1	0	0	0	13	7	14	13
Oxides-silcates																
Braunite	$Mn^{2+}Mn^{3+}_6SiO_{12}$	210s 331. 376w. 510m 622. 685. 970	RRUFF	0	0	0	0	0	0	0	0	0	74	0	0	0
Fe mineral assemblage																
Oxides and hydroxides																
Hematite	Fe_2O_3	222. 290. 408. 490. 607 hem	Das and Hendry (2011)	78	116	102	100	132	59	40	159	58	36	51	106	150
Goethite	FeOOH	162. 243. 297s. 385s. 477. 545	Das and Hendry (2011)	2	0	0	0	0	1	0	0	0	0	0	0	0
Carbonates																
Siderite	$FeCO_3$	180. 282. 722. 1082	Das and Hendry (2011)	0	1	2	1	0	0	0	0	0	13	17	28	29
Ankerite	$CaFeCO_3$	179. 299. 721. 1095	RRUFF	15	15	17	26	49	36	0	2	0	0	0	1	0
Sulfides																
Marcasite	FeS_2	292w. 321. 386	RRUFF	0	0	0	0	0	2	2	0	0	0	0	0	0

Others																	
Oxides – hyydroxides																	
Quartz	SiO_2	125.207. 353. 393 w. 464s	RRUFF	27	32	42	45	3	70	40	25	0	0	70	24	26
Carbonates																	
Dolomite	$CaMg(CO_3)_2$	179. 299. 721. 1097	RRUFF	0	4	0	0	0	0	25	20	0	0	0	0	0
Silicates																	
Albite	$NaAlSi_3O_8$	478s. 507s. 287m. 330. 244w. 207sh. 182m. 161 sh	RRUFF	35	71	45	30	1	2	0	1	0	81	30	26	3
Mica (muscovite)		259s. 400. 703	RRUFF	0	2	0	0	0	0	0	0	0	0	0	0	0
Phosphates																	
Apatite	$[(Ca_{10}(PO_4)_6(OH. F. Cl)_2]$	427. 587. 605 w. 965s. 1040 w. 1078 w	RRUFF	1	1	0	0	0	0	3	1	0	35	0	0	0
Organic material			Jehlicka et al. (2009); Chen et al. (2007); Okolo et al. (2015)														
org1		1330. 1606. 1754. 1824	CH3. fluerene. carboxyls. C=O in oils	8	11	5	13	4	1	2	3	0	0	0	0	1
org2		1245. 1330. 1600	CH2 scissors mode CH3. C=C fluerene	5	13	3	15	5	3	1	0	0	0	0	0	0
org3		1326. 1717	CH3 aliphatic. carboxyls	9	9	3	4	3	3	0	0	1	1	0	0	0
org4		1412. 1727	CH3/CH2. carboxyls	1	1	0	0	0	0	0	0	0	0	17	9	9
org5		1267. 1332. 1363. 1484. 1606. 1847	CH2 scissors mode. CH aliphatic band. CH3. CH2/CH3 vibrational mode. C=C in fuerene C=O in oils	3	3	3	3	3	4	4	4	0	0	11	9	1
org6		1387. 1522. 1607	CH3. C=C stretching of polyene chain. aromatic C=C in fluerene	0	0	0	0	0	0	0	0	0	0	0	0	0
org7		1336. 1610	CH3. aromatic C=C in fluerene	4	4	4	4	4	4	1	4	0	3	3	3	3

References

Chen. J.Y.. Schopf. J.W.. Bottjer. D.J.. Zhang. C.Y.. Kudryavtsev. A.B.. Tripathi. A.B.. Wang. X.Q.. Yang. Y.H.. Gao. X. and Yang. Y.. 2007. Raman spectra of a Lower Cambrian ctenophore embryo from southwestern Shaanxi. China. *Proceedings of the National Academy of Sciences*. *104*(15). pp.6289-6292.

Das. S. and Hendry. M.J.. 2011. Application of Raman spectroscopy to identify iron minerals commonly found in mine wastes. *Chemical Geology*. *290*(3). pp.101-108.

Jehlička. J.. Edwards. H.G.M. and Vítek. P.. 2009. Assessment of Raman spectroscopy as a tool for the non-destructive identification of organic minerals and biomolecules for Mars studies. *Planetary and space Science*. *57*(5). pp.606-613.

Okolo GN. Neomagus HW. Everson RC. et al. (2015) Chemical–structural properties of South African bituminous coals: insights from wide angle XRD–carbon fraction analysis. ATR–FTIR. solid state 13 C NMR. and HRTEM techniques. Fuel 158: 779–792.

Orange. D.. Knittle. E.. Farber. D. and Williams. Q.. 1996. Raman spectroscopy of crude oils and hydrocarbon fluid inclusions: A feasibility study. *The Geochemical Society*. *Special Publication*. 5. pp.65-81.

Sepúlveda. M.. Gutiérrez. S.. Vallette. M.C.. Standen. V.G.. Arriaza. B.T. and Cárcamo-Vega. J.J.. 2015. Micro-Raman spectral identification of manganese oxides black pigments in an archaeological context in Northern Chile. *Heritage Science*. *3*(1). p.32.

RRUFF

SI 6. Mineral composition of nodules and sections based on Raman spectroscopy

NODULES – only Raman profiles (Fig. 10)

1. (86)

The mineralized cycles are formed by alternating
Hematite ↔ ankerite ↔ quartz cycles (a few tens of μm) The nodule is carbonate-rich with quartz spots. the matrix quartz-rich and fine disseminated carbonate halo occur.

Mn cycle
The mineralized cycles are formed by alternating
kutnohorite (double carb) ↔hematite and quartz (cyclic)
Fe cycle
hematite
Quartz also show cyclic section parts.

1. (88) (OM. CL same area. Raman and FTIR different area)

The mineralized cycles are formed by alternating
Hematite ↔ ankerite ↔ quartz cycles (a few tens of μm) The nodule is carbonate-rich with quartz spots. the matrix quartz-rich and fine disseminated carbonate occur.

Mn cycle
The mineralized cycles are formed by alternating
kutnohorite (double carb) ↔hematite and quartz (cyclic)
Fe cycle
hematite
Quartz also show cyclic section parts.
Similar to 1 (86)

2. (86)

The mineralized cycles are formed by alternating
Hematite ↔ ankerite ↔ calcite ↔ quartz cycles (a few tens of μm) The nodule is carbonate-rich with quartz spots, the matrix quartz-rich and fine disseminated carbonate occur.

Around the nodule biomat zone, quartz and hematite occur, toward the nodule a carbonate zone occurs (fine grained) and again a quartz–rich zone occur. The inner part of nodule is carbonate-rich with quartz spots (red). The sample is fine grained.

Mn cycle
The mineralized cycles are formed by alternating
kutnohorite (double carb) ↔hematite and quartz (cyclic)
Fe cycle
hematite
Quartz also shows cyclic section parts.

2. (157)

Main components are hematite, quartz and ankerite. In the marginal part it shows cyclic occurrence, but the inner core is quartz rich. The marginal part contain idiomorphic coarse grained carbonate crystals, which include a mineralized (Fe-rich-brown) microbial biosignature.

The mineralized cycles are formed by alternating
Hematite ↔ ankerite ↔ calcite ↔ quartz cycles (a few tens of μm)

Mn cycle
The mineralized cycles are formed by alternating
kutnohorite (double carb) ↔hematite and quartz (cyclic)
Fe cycle
hematite
Quartz also shows cyclic section parts.

2B (157)

Main components are hematite, quartz and ankerite.
The mineralized cycles are formed by alternating
Hematite ↔ ankerite ↔ calcite ↔ quartz cycles (a few tens of μm)

Mn cycle
The mineralized cycles are formed by alternating
kutnohorite (double carb) ↔hematite and quartz (cyclic)
Fe cycle
hematite↔
Quartz also show cyclic section parts.

2A (88)

Main components are hematite, quartz and ankerite.
The mineralized cycles are formed by alternating
Hematite ↔ ankerite ↔quartz cycles (a few tens of μm)

Mn cycle
The mineralized cycles are formed by alternating
kutnohorite (double carb) ↔hematite and quartz (cyclic)
Fe cycle
hematite↔
Quartz also shows cyclic section parts.

3B (93)

Main components are hematite. quartz, ankerite, calcite(rhodochrosite), feldspar (albite) and apatite.
The mineralized cycles are formed by alternating
Hematite ↔ ankerite ↔quartz cycles (a few tens of μm)

Mn cycle
The mineralized cycles are formed by alternating
kutnohorite (double carb) ↔hematite and quartz (cyclic)

Fe cycle
hematite↔
Quartz also shows cyclic section parts.

3 (93)

hematite
apatite
dolomite
quartz

4A (86)

Main components are hematite, quartz, ankerite and calcite/rhodochrosite.
The mineralized cycles are formed by alternating
Hematite ↔ ankerite ↔quartz cycles (a few tens of μm)

The core and the outer rim of the nodule contain Mn-calcite (bright CL) besides the other main minerals.

Mn cycle
The mineralized cycles are formed by alternating
kutnohorite (double carb) ↔hematite and quartz (cyclic)
Fe cycle
hematite↔
Quartz also show cyclic section parts.

4B (86)

Main components are hematite, quartz, ankerite and calcite/rhodochrosite.
The mineralized cycles are formed by alternating
Hematite ↔ ankerite ↔quartz cycles (a few tens of μm)

The core of the nodule contain Mn-calcite (bright CL)

Mn cycle
The mineralized cycles are formed by alternating
kutnohorite (double carb) ↔hematite and quartz (cyclic)
Fe cycle
hematite↔
Quartz also show cyclic section parts.

5 (153B)

Main components are hematite, braunite, siderite.

The mineralized cycles are formed by alternating
Hematite ↔ braunite ↔ siderite

Precursor Mn-oxide and segregated quartz can form Mn-oxide/silicate mineral.

Mn cycle

The mineralized cycles are formed by alternating
braunite ↔hematite
Fe cycle
hematite↔

6 (153A)

Main components are hematite, jacobsite, calcite.

The mineralized cycles are formed by alternating
Hematite ↔ jacobsite ↔ calcite

Mn cycle
The mineralized cycles are formed by alternating
jacobsite ↔hematite
Fe cycle
hematite↔

SECTIONS - only Raman profiles (Fig. 10)

A (88)

Biomat structure

Gray, black metalliferous parts: hematite mineralized cycles – quartz (Fe)

Red part: hematite ↔ carbonate (Fe, Mn), quartz (Fe+Mn)

Gray, black metalliferous parts: hematite – quartz (Fe)

Quartz is segregated (CL).

B (88)

Biomat structure

Red part: hematite mineralized cycles ↔ carbonate (Fe, Mn), quartz (Fe+Mn)

rhodochrosite ↔ kutnohorite (during diagenesis, rhodochrosite transform to kutnohorite by taking up more Ca and Mg)

Gray, black metalliferous parts: hematite mineralized cycles – quartz (Fe)

There are quartz-rich parts

Quartz show cyclic occurrence

Embryos of nodules (micro-nodules) occur (OM. CL) in laminae, meaning that a part of nodule formation starts in the syngenetic period,and later larger nodules also occur, which contain hematite ↔ carbonate.

C (86)

Biomat structure

Based on observation (e.g. 86, also in 157) there are red wide laminae, but also black, metalliferous laminae, too. In the black laminae there are red individual nodules in a chain, which do not contact, so they do not form a continuous lamina (layer). If we see the contemporary sediment surface these "nodules" most probably were lenses of microbial colonies, and the intensity of development of these colonies could have differed, in some cases they could not join to each other on the sediment surface, and later on a perpendicular section they occur as individual lens cuts ("micro-nodules"). If the intensity was stronger, or the time period was longer, these lenses would be able to reach each other and form a quasi continuous lamina (layer). In Úrkút, in Mn carbonate ore this observation was made with pink rhodochrosite-rich lenses („micro-nodules"), and laminae.
The red lamina is not homogenous, black spots occcur, and nodule embryos occur. Carbonate- and quartz-bearing parts alternate.

Gray, black metalliferous parts: hematite mineralized cycles – (Fe) with carbonate spots

Red part: hematite ↔ carbonate (Fe, Mn) (Fe+Mn) **NICE CYCLIC PART**

Gray, black metalliferous parts: hematite – (Fe) with carbonate spots

rhodochrosite ↔ kutnohorite (during diagenesis, rhodochrosite transform to kutnohorite by taking up more Ca and Mg)

Mn occurs in lamination.

D (152)

Biomat structure

Gray, black metalliferous part with lamination: hematite mineralized cycles – (Fe) with low amount of cyclic quartz and apatite spots

Elongated lenses can be seen.

E (152)

Biomat structure (metalliferous)

Gray, black metalliferous part with lamination: hematite mineralized cycles – (Fe) with low amounts of cyclic quartz in the central zone of the section.

The red parts contain larger grains, macroscopically dark spots.

The red section part: hematite mineralized cycles ↔ carbonate (Mn) (Fe+Mn) and quartz and also apatite

rhodochrosite ↔ kutnohorite (during diagenesis, rhodochrosite transforms to kutnohorite by taking up more Ca and Mg)

F (141)

Coarse-grained occurrence.

Hematite mineralized cycles ↔ quartz mineralized cycles ↔ braunite mineralized cycles (Mn oxide/silicate)(Mn +Fe)

Quartz can support feldspar (albite, K-feldspar) and pyroxene (aegirine) formation as diagenetic products.

G (153A)

Biomat structure. microbial micro-texture

Half of this sample is coarse-grained and then fine black, metalliferous and alternating red lamination develop. Nodules occur. Laminae often are not continuous.

Gray, black metalliferous parts: hematite mineralized cycles – (Fe) with quartz and scarce carbonate and feldspar spots

Red part: hematite mineralized cycles ↔ carbonate (kutnohorite)(Mn) (Fe+Mn)

Point analyses in this sample detected anatase (main component) and traces of alabandite and marcasite.

SI 7. Raman profiles of nodules

86N1

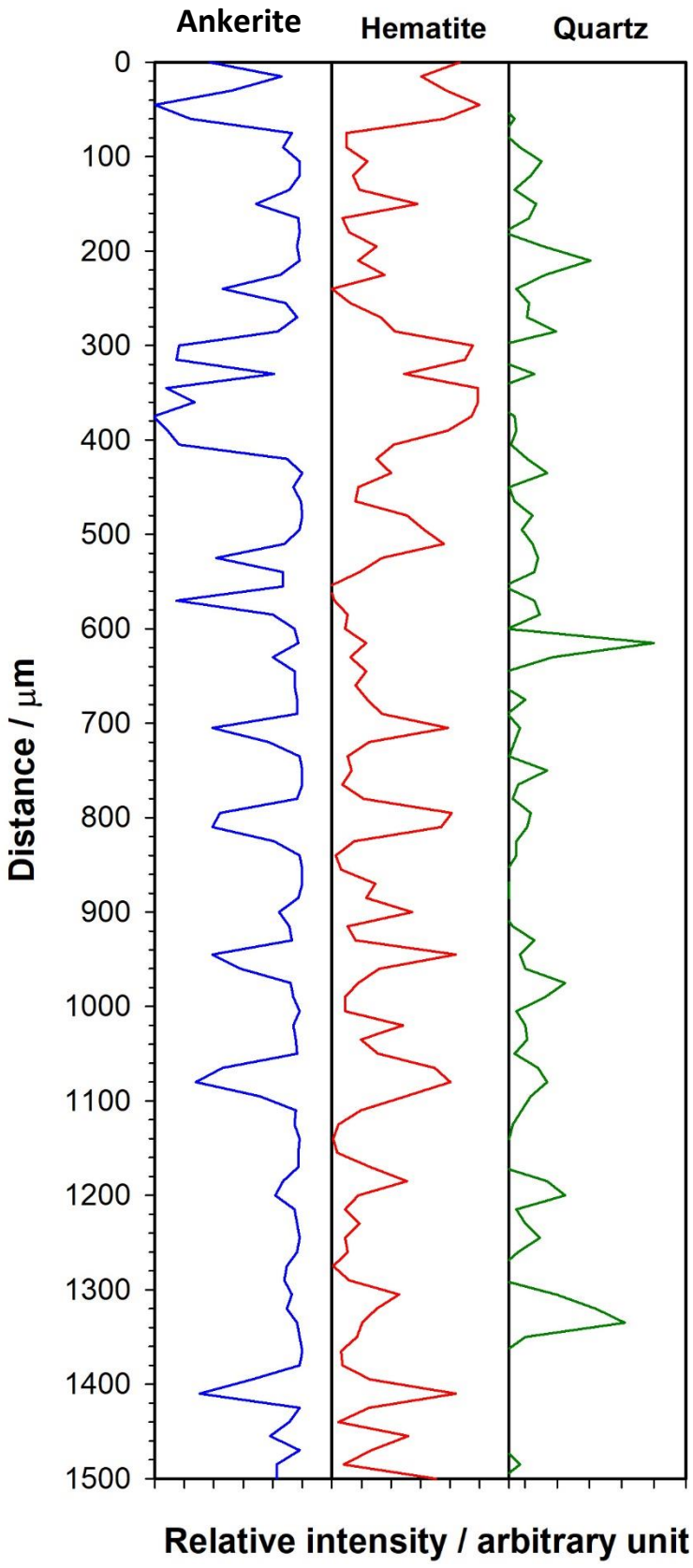

86N2

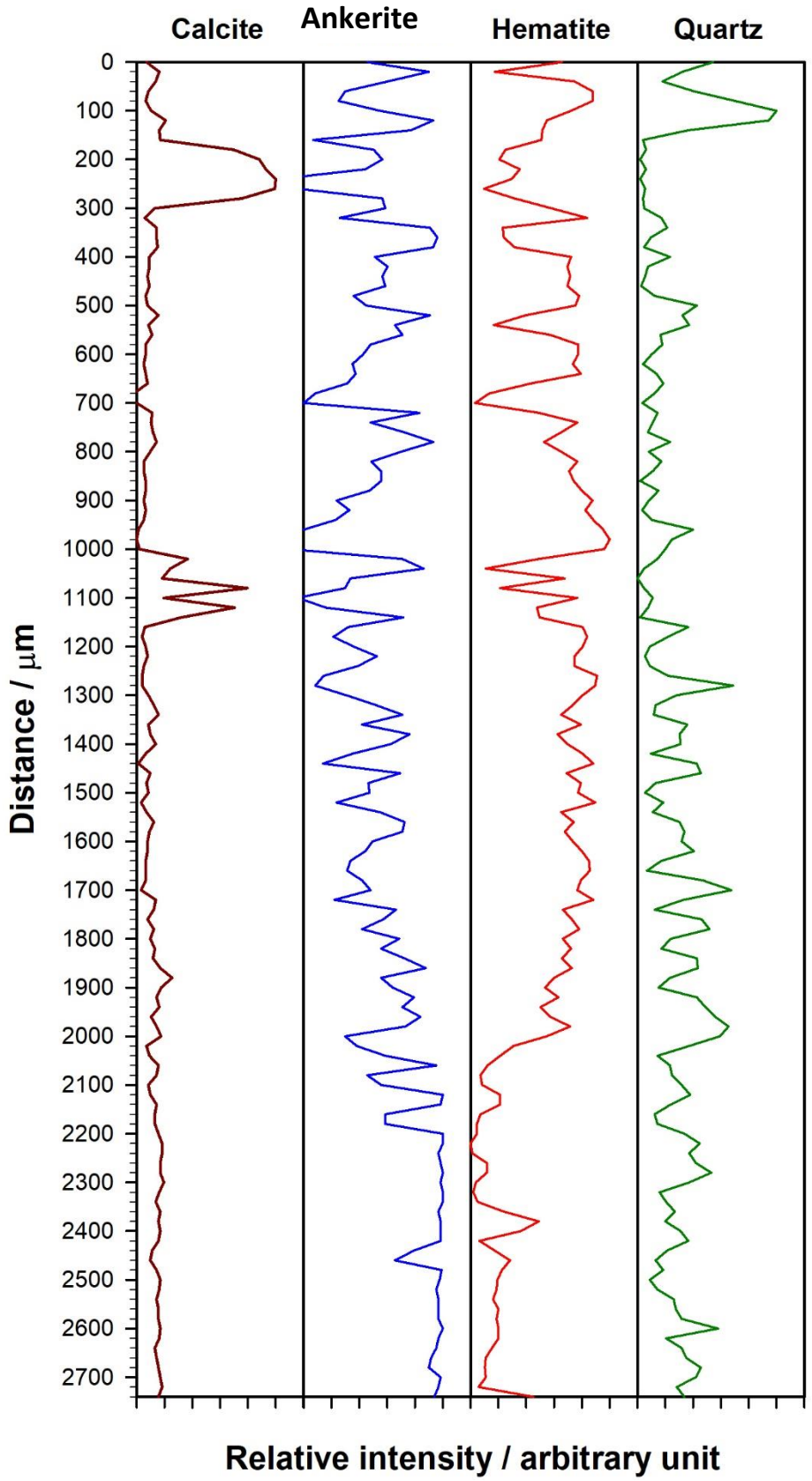
Calcite
Ankerite
Hematite
Quartz
Distance / μm
0
100
200
300
400
500
600
700
800
900
1000
1100
1200
1300
1400
1500
1600
1700
1800
1900
2000
2100
2200
2300
2400
2500
2600
2700
Relative intensity / arbitrary unit

86N4A

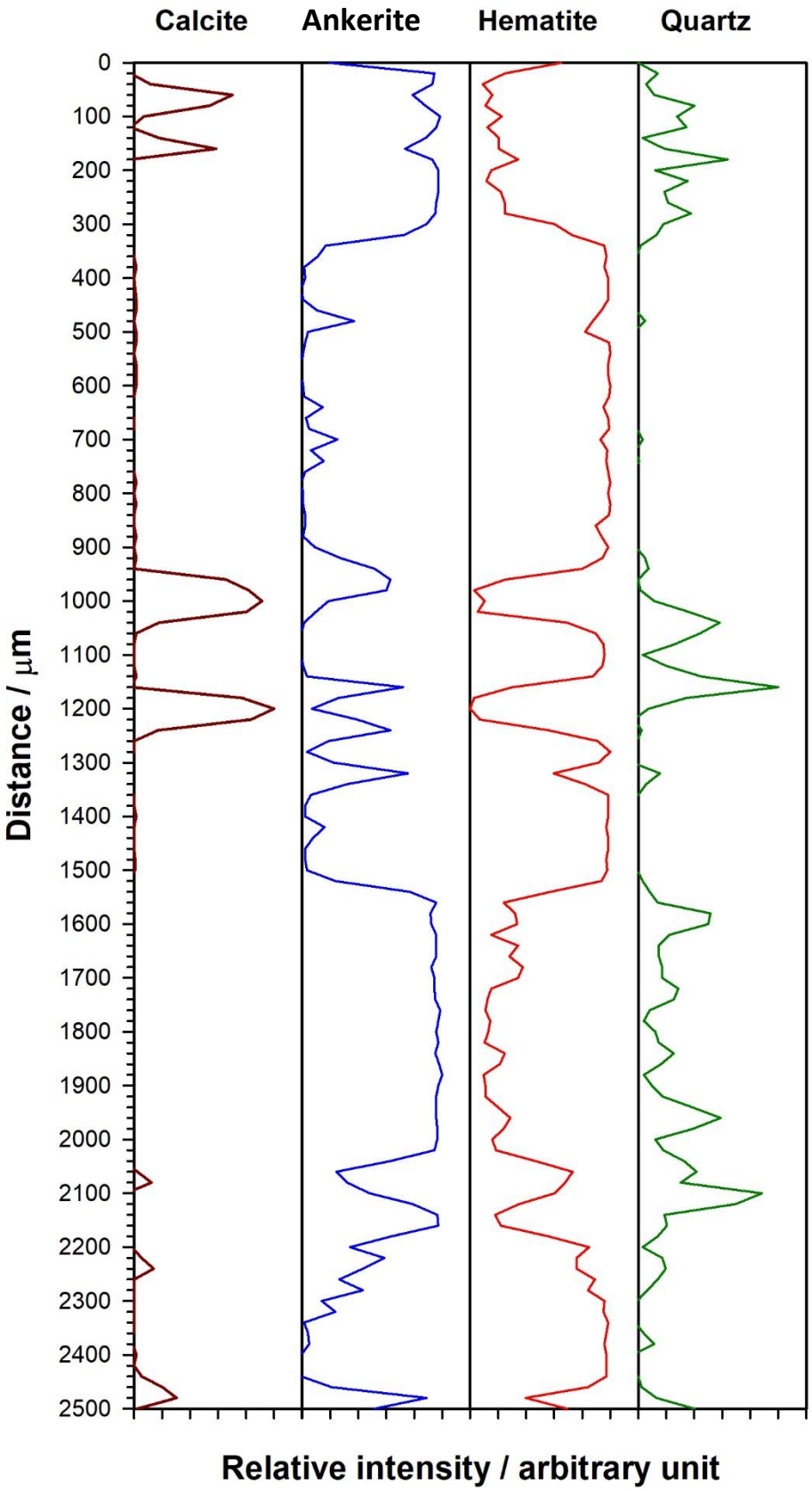
Calcite
Ankerite
Hematite
Quartz
0
100
200
300
400
500
600
700
800
900
1000
1100
1200
1300
1400
1500
1600
1700
1800
1900
2000
2100
2200
2300
2400
2500
Distance / μm
Relative intensity / arbitrary unit

86N4B

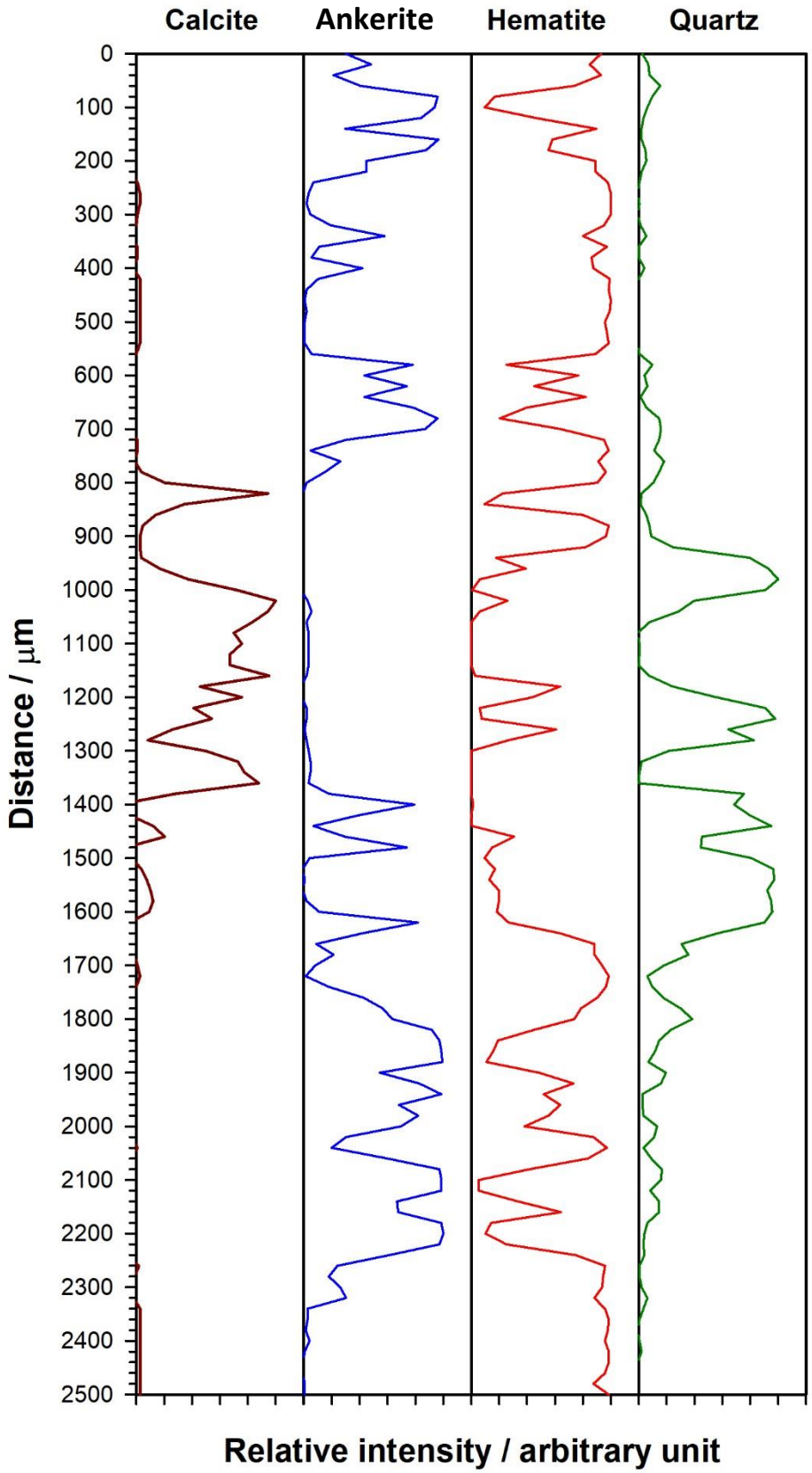
Calcite
Ankerite
Hematite
Quartz
Distance / μm
0
100
200
300
400
500
600
700
800
900
1000
1100
1200
1300
1400
1500
1600
1700
1800
1900
2000
2100
2200
2300
2400
2500
Relative intensity / arbitrary unit

88N1

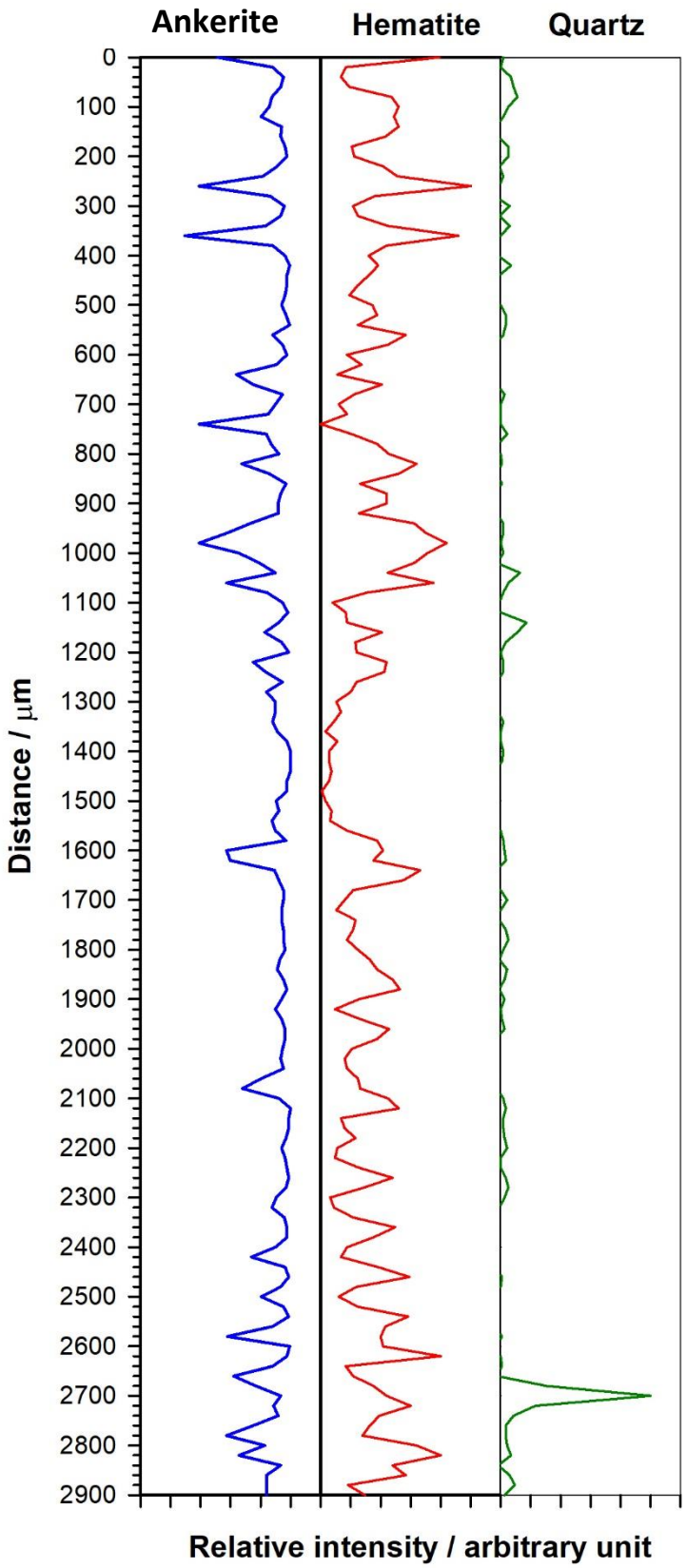
Ankerite
Hematite
Quartz
Distance / μm
0
100
200
300
400
500
600
700
800
900
1000
1100
1200
1300
1400
1500
1600
1700
1800
1900
2000
2100
2200
2300
2400
2500
2600
2700
2800
2900
Relative intensity / arbitrary unit

88N2A

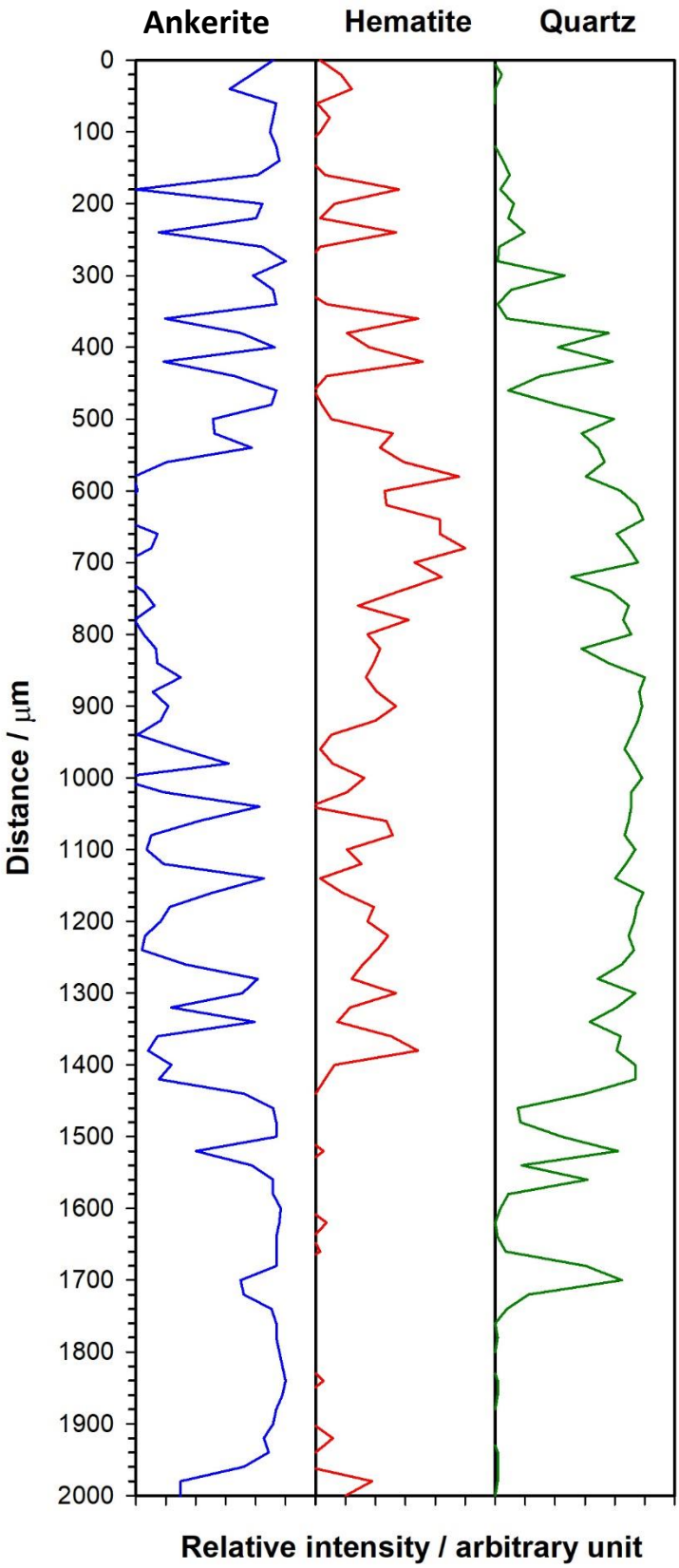
Ankerite
Hematite
Quartz
0
100
200
300
400
500
600
700
800
900
1000
1100
1200
1300
1400
1500
1600
1700
1800
1900
2000
Distance / μm
Relative intensity / arbitrary unit

93N3B

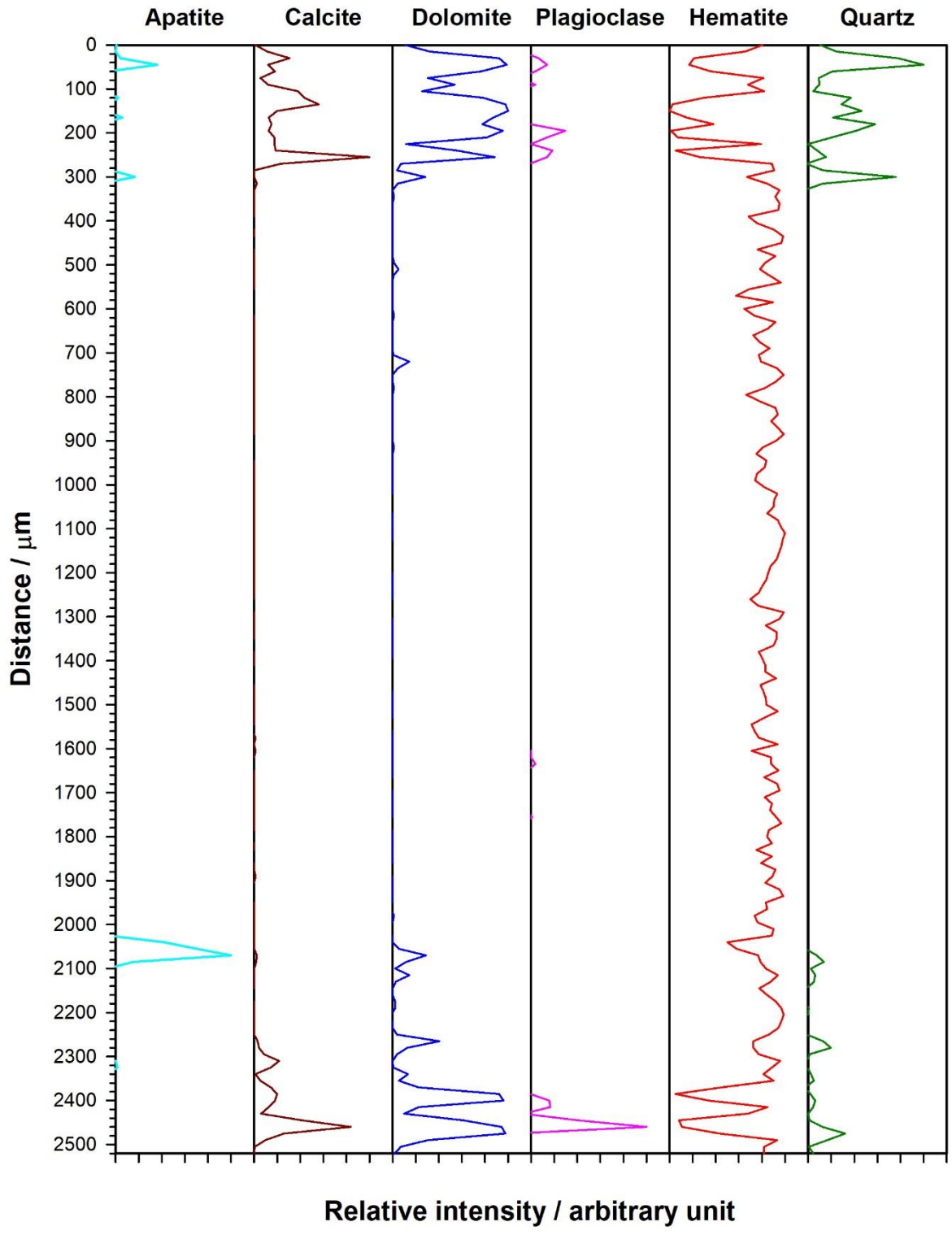

Ankerite

153AN6

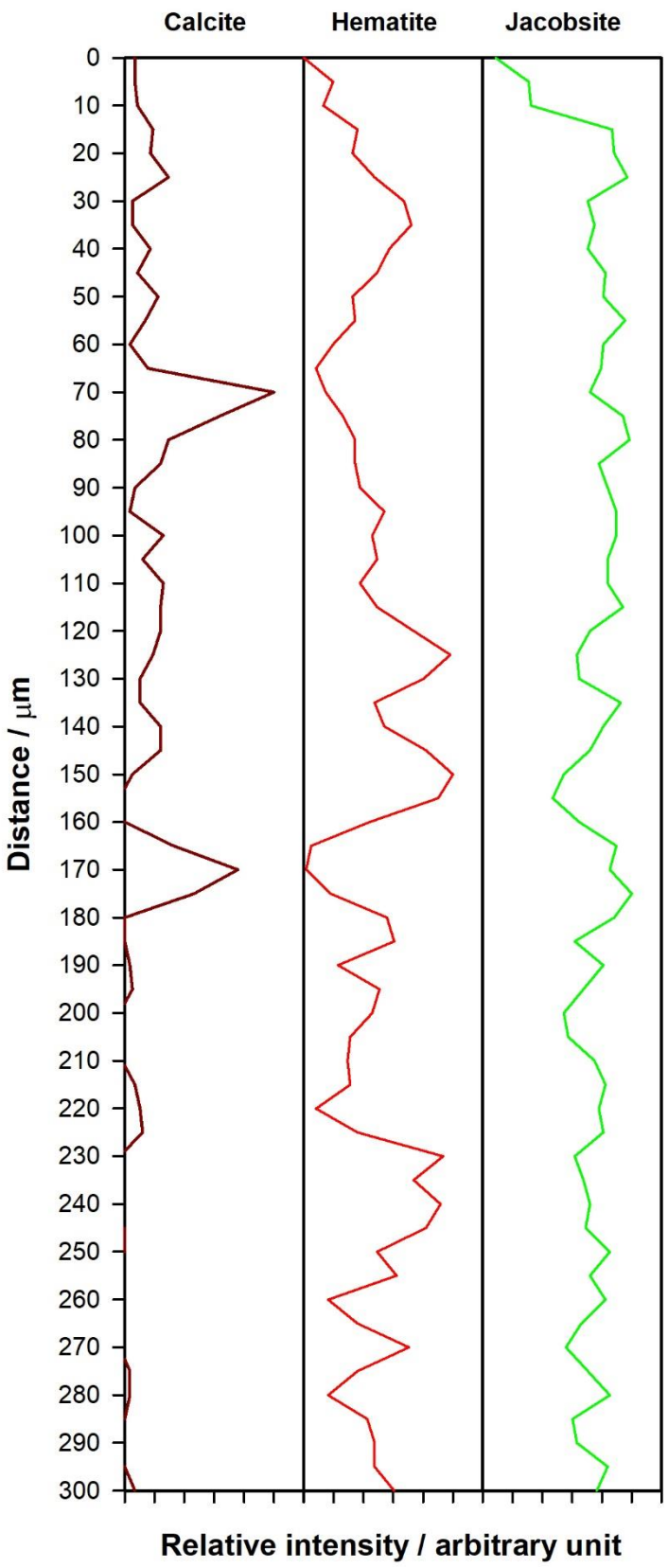
Calcite
Hematite
Jacobsite
0
10
20
30
40
50
60
70
80
90
100
110
120
130
140
150
160
170
180
190
200
210
220
230
240
250
260
270
280
290
300
Distance / μm
Relative intensity / arbitrary unit

153BN5

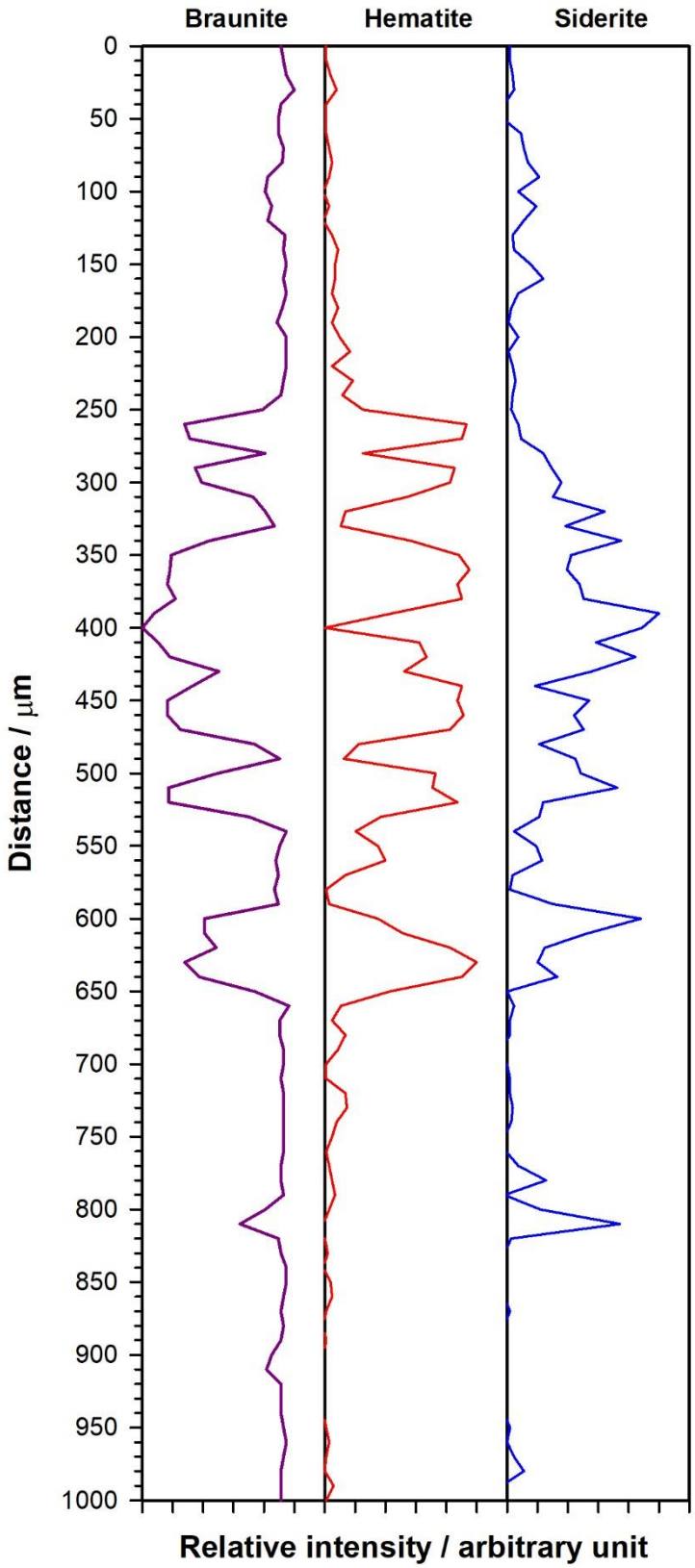
Braunite
Hematite
Siderite
Distance / μm
0
50
100
150
200
250
300
350
400
450
500
550
600
650
700
750
800
850
900
950
1000
Relative intensity / arbitrary unit

157N2

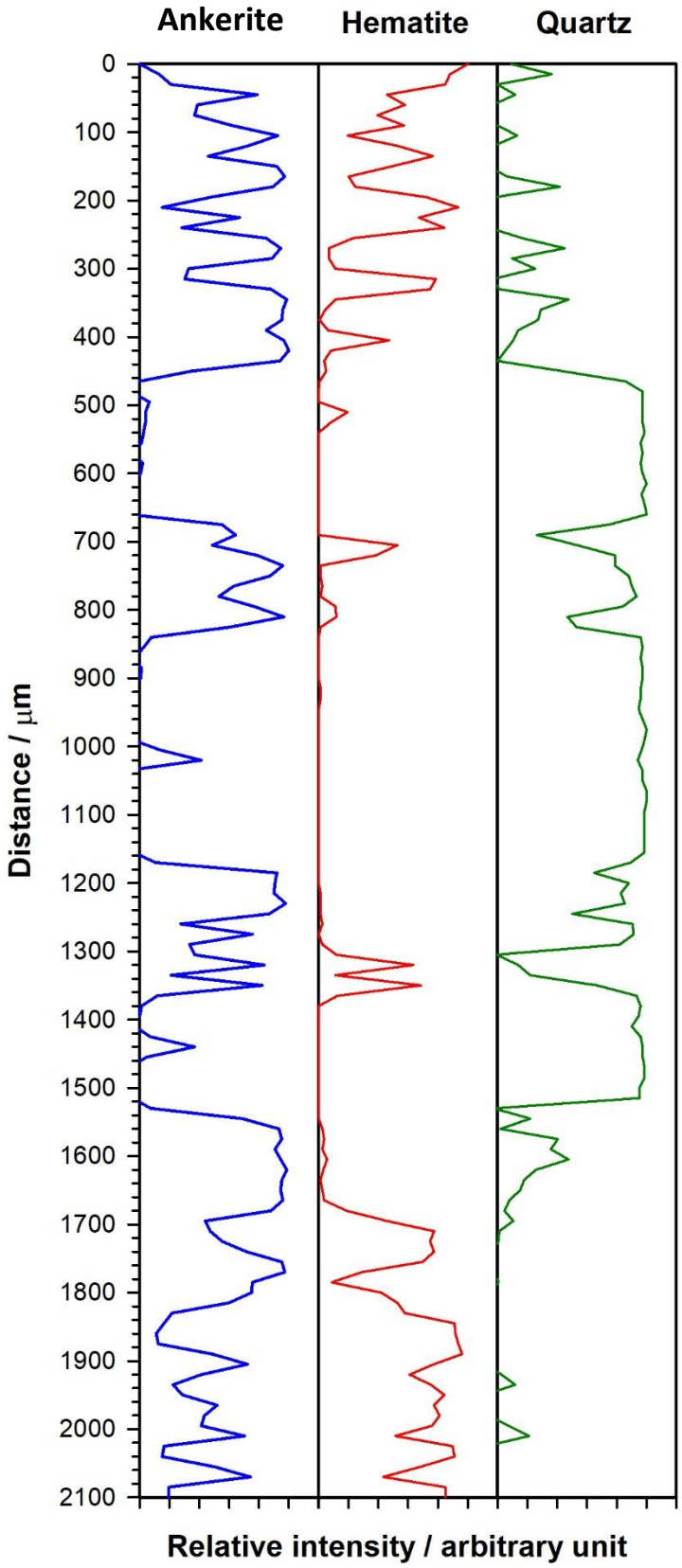
Ankerite
Hematite
Quartz
0
100
200
300
400
500
600
700
800
900
1000
1100
1200
1300
1400
1500
1600
1700
1800
1900
2000
2100
Distance / μm
Relative intensity / arbitrary unit

157N2B

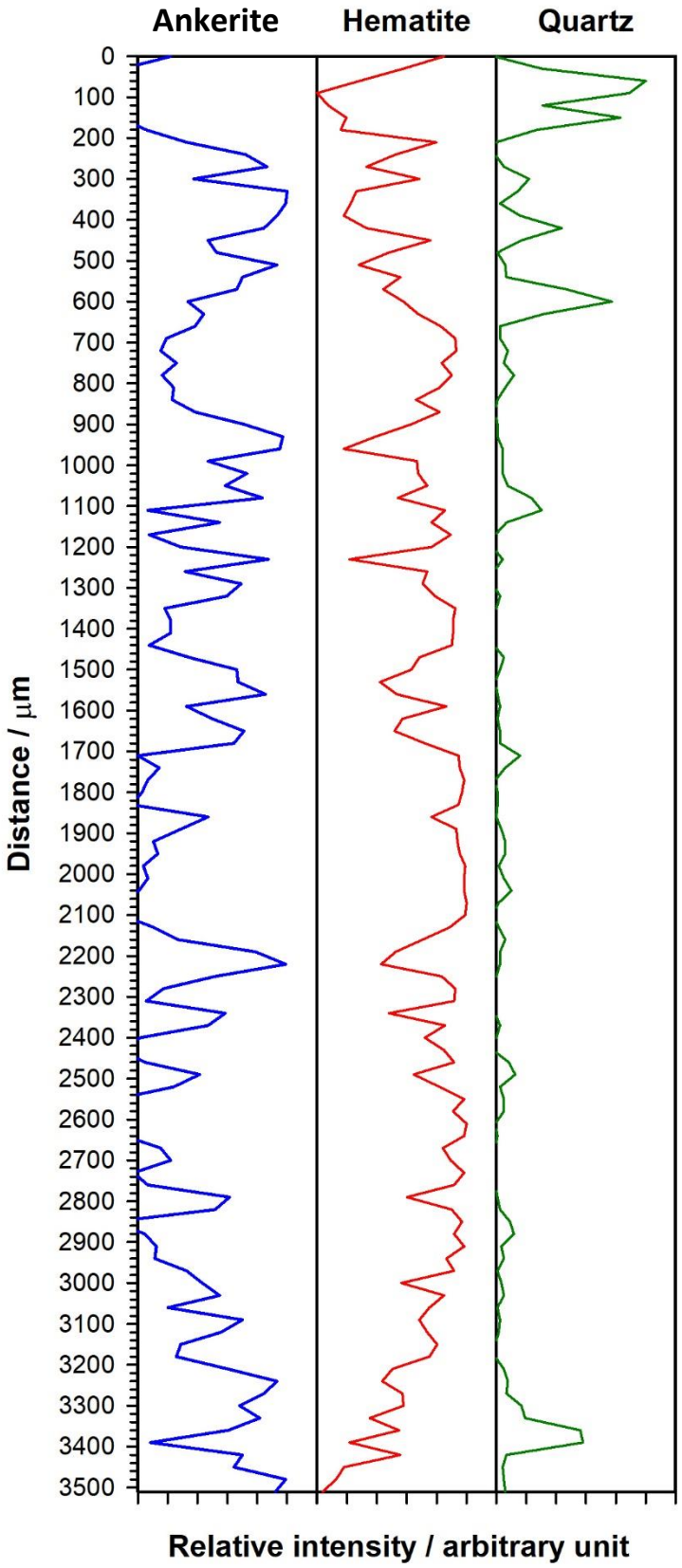
Ankerite
Hematite
Quartz
Distance / μm
0
100
200
300
400
500
600
700
800
900
1000
1100
1200
1300
1400
1500
1600
1700
1800
1900
2000
2100
2200
2300
2400
2500
2600
2700
2800
2900
3000
3100
3200
3300
3400
3500
Relative intensity / arbitrary unit

157N3

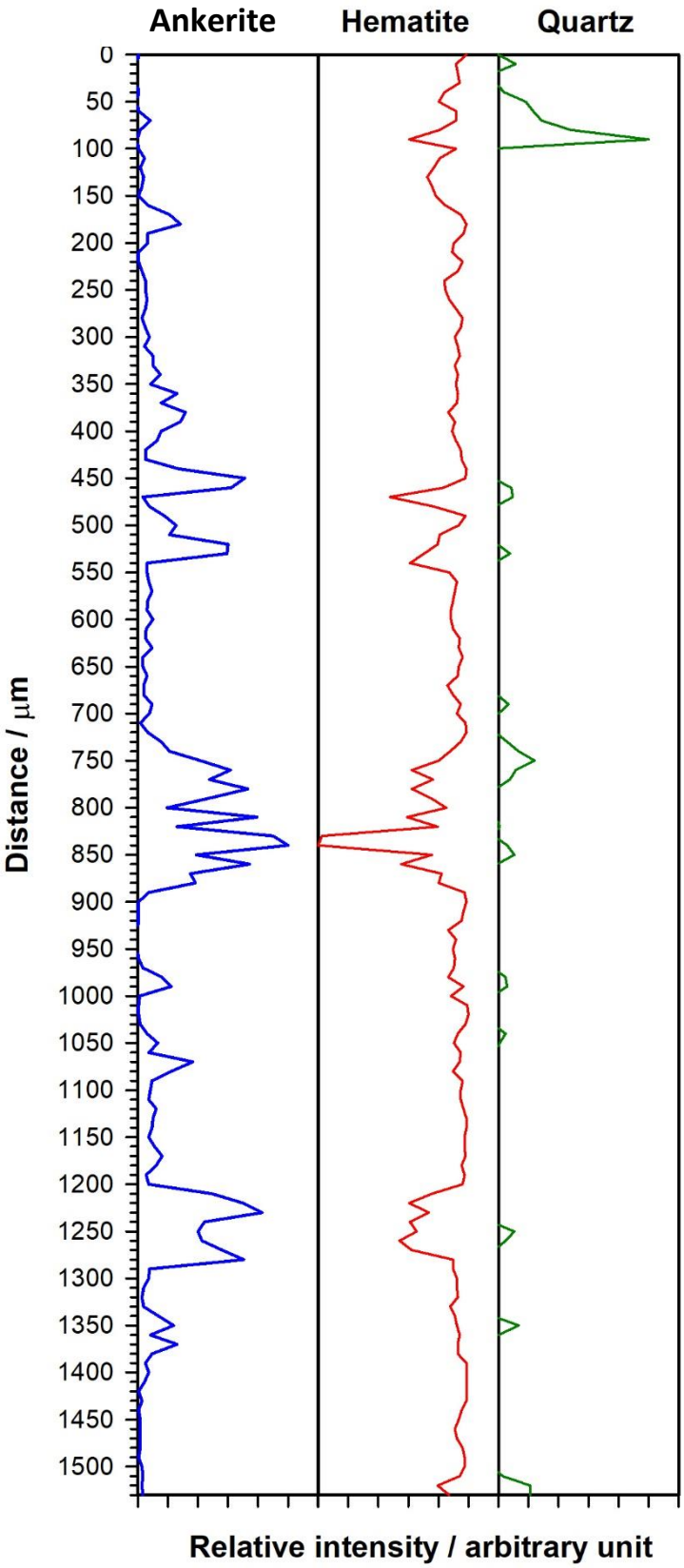
Ankerite
Hematite
Quartz
Distance / μm
0
50
100
150
200
250
300
350
400
450
500
550
600
650
700
750
800
850
900
950
1000
1050
1100
1150
1200
1250
1300
1350
1400
1450
1500
Relative intensity / arbitrary unit

SI 8. Raman profiles of sections

A (88)

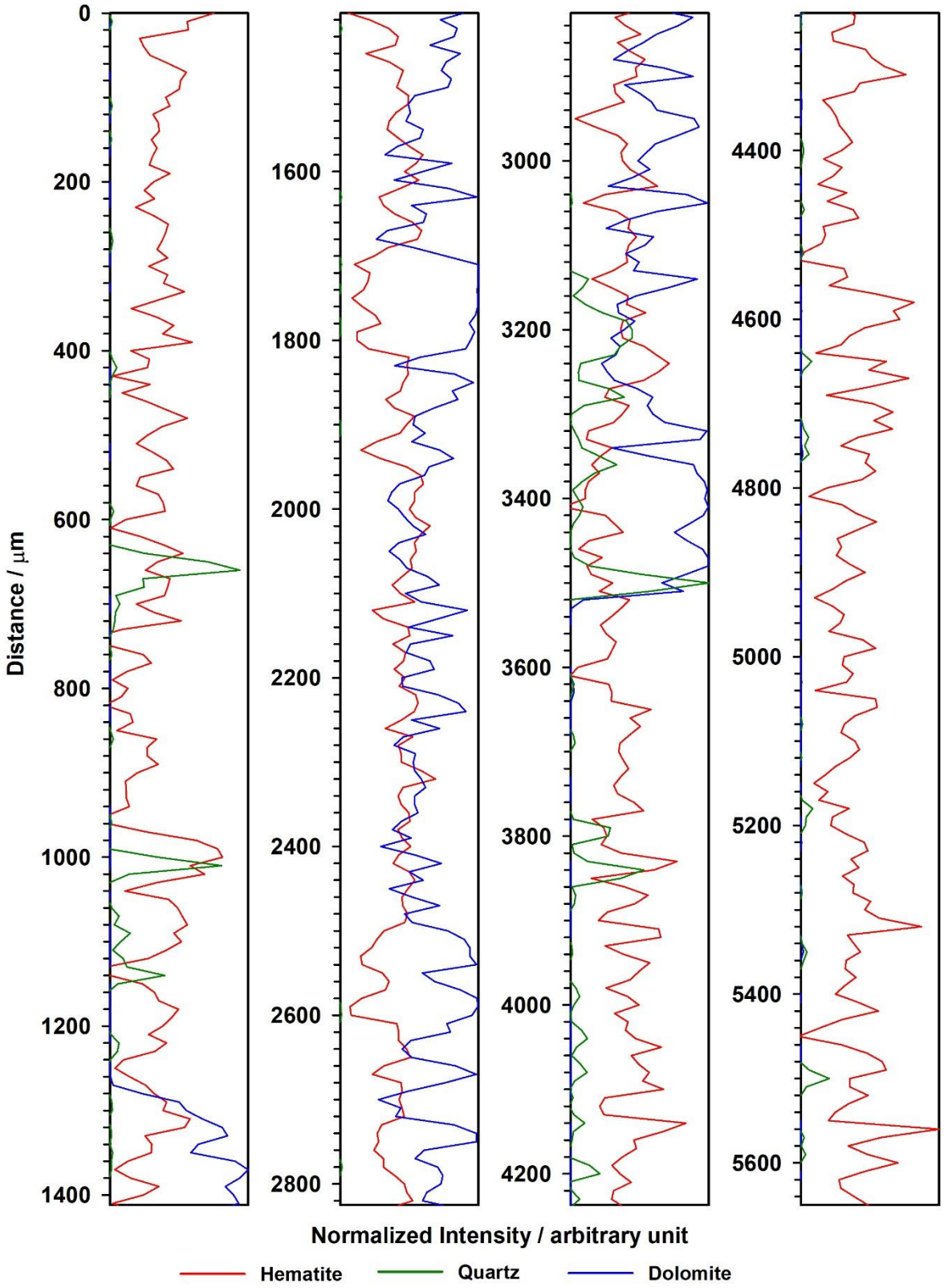

B (88)

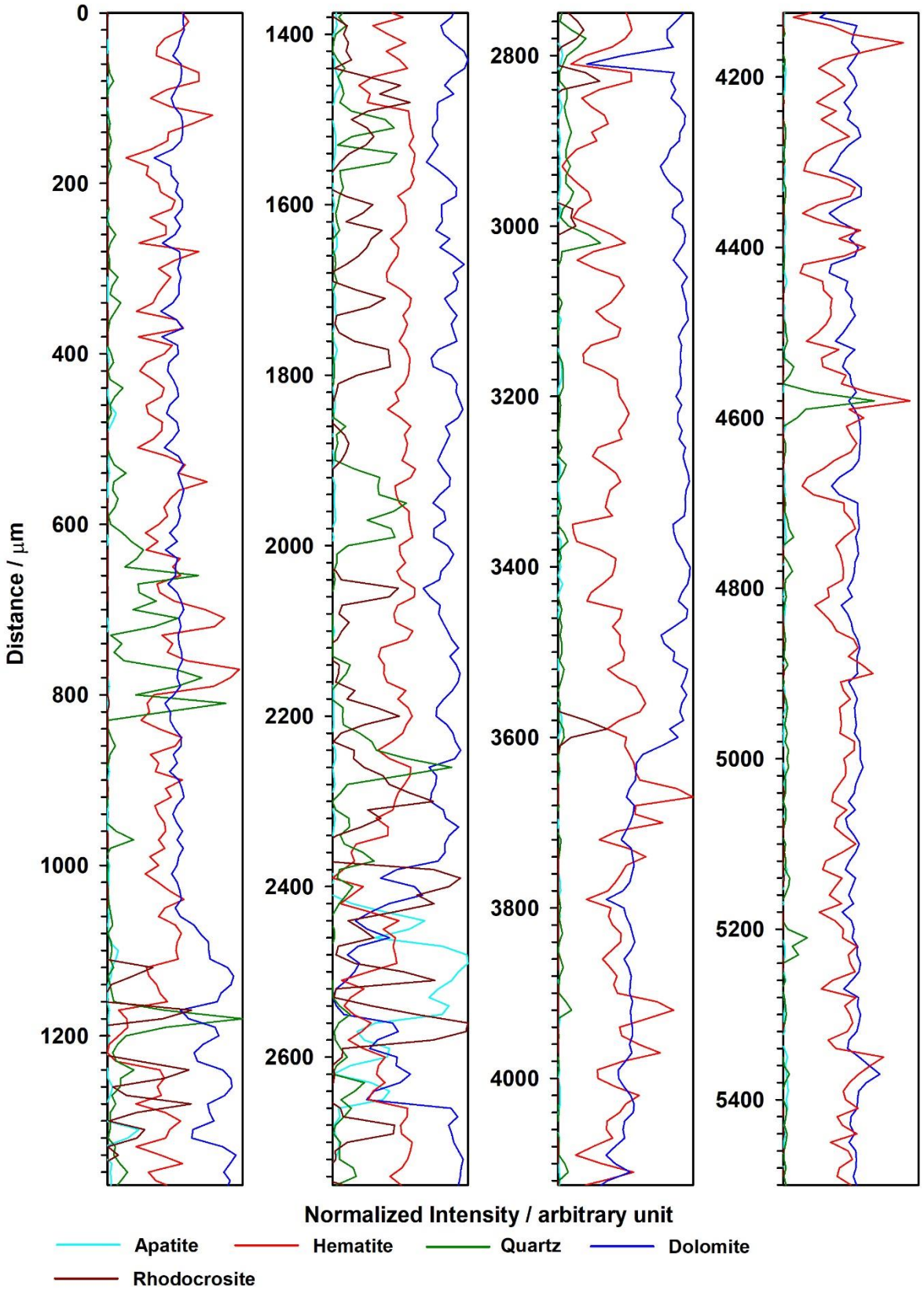
Distance / μm
0
200
400
600
800
1000
1200
1400
1600
1800
2000
2200
2400
2600
2800
3000
3200
3400
3600
3800
4000
4200
4400
4600
4800
5000
5200
5400
Normalized Intensity / arbitrary unit
Apatite
Hematite
Quartz
Dolomite
Rhodocrosite

C (86)

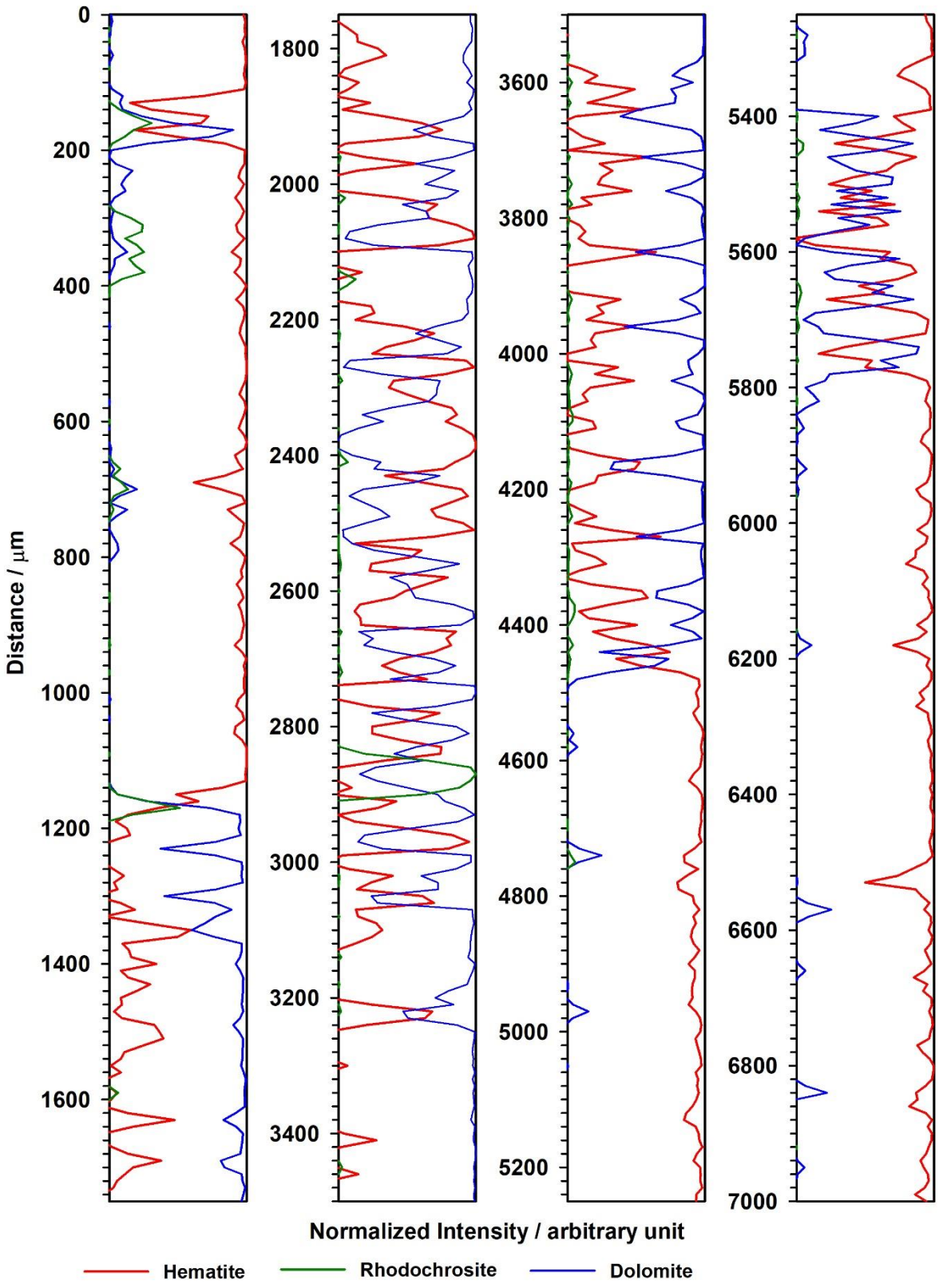
Distance / μm
0
200
400
600
800
1000
1200
1400
1600
1800
2000
2200
2400
2600
2800
3000
3200
3400
3600
3800
4000
4200
4400
4600
4800
5000
5200
5400
5600
5800
6000
6200
6400
6600
6800
7000
Normalized Intensity / arbitrary unit
Hematite
Rhodochrosite
Dolomite

D (152)

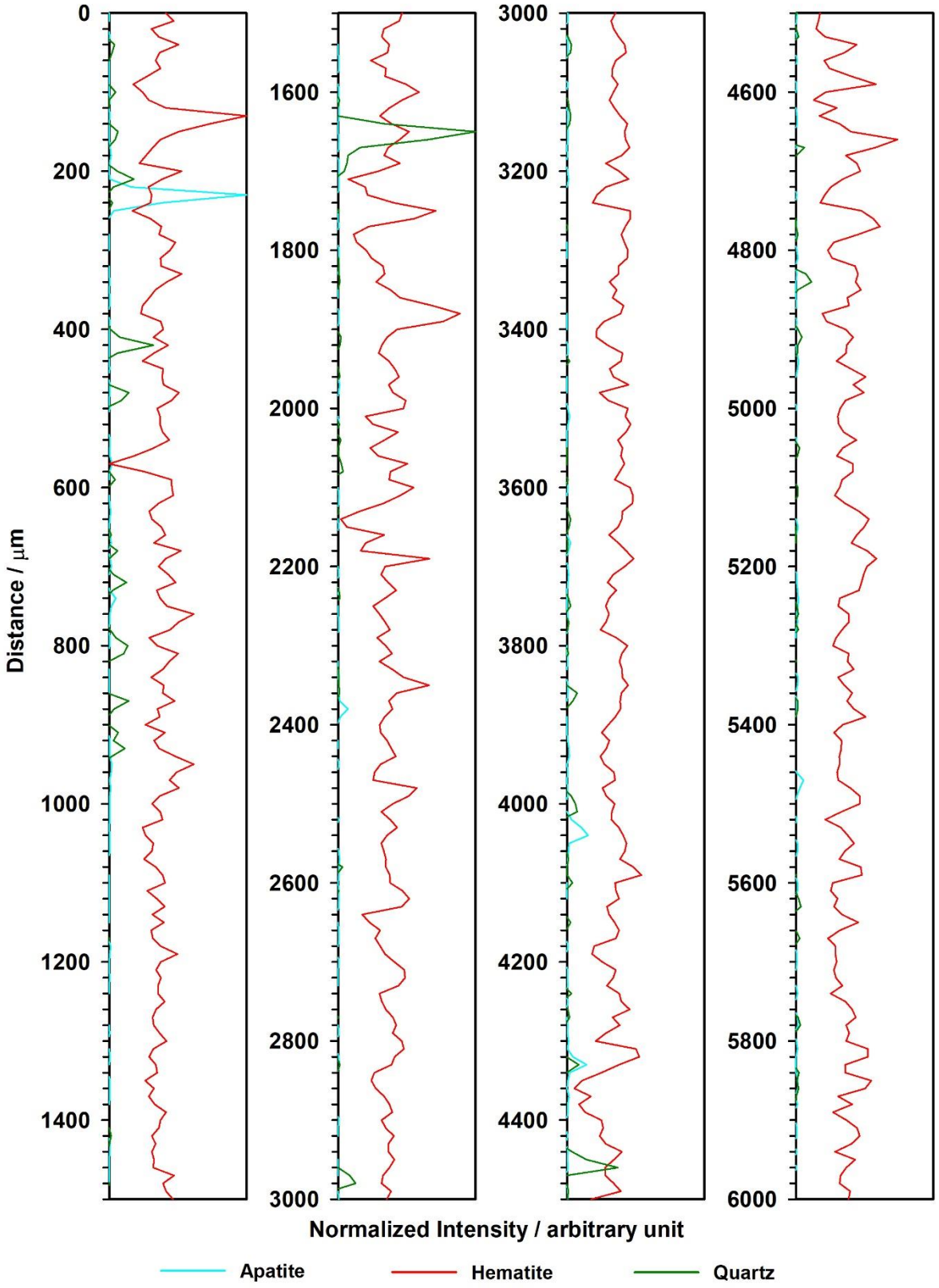
Distance / μm
0
200
400
600
800
1000
1200
1400
1600
1800
2000
2200
2400
2600
2800
3000
3000
3200
3400
3600
3800
4000
4200
4400
4600
4800
5000
5200
5400
5600
5800
6000
Normalized Intensity / arbitrary unit
Apatite
Hematite
Quartz

E (152)

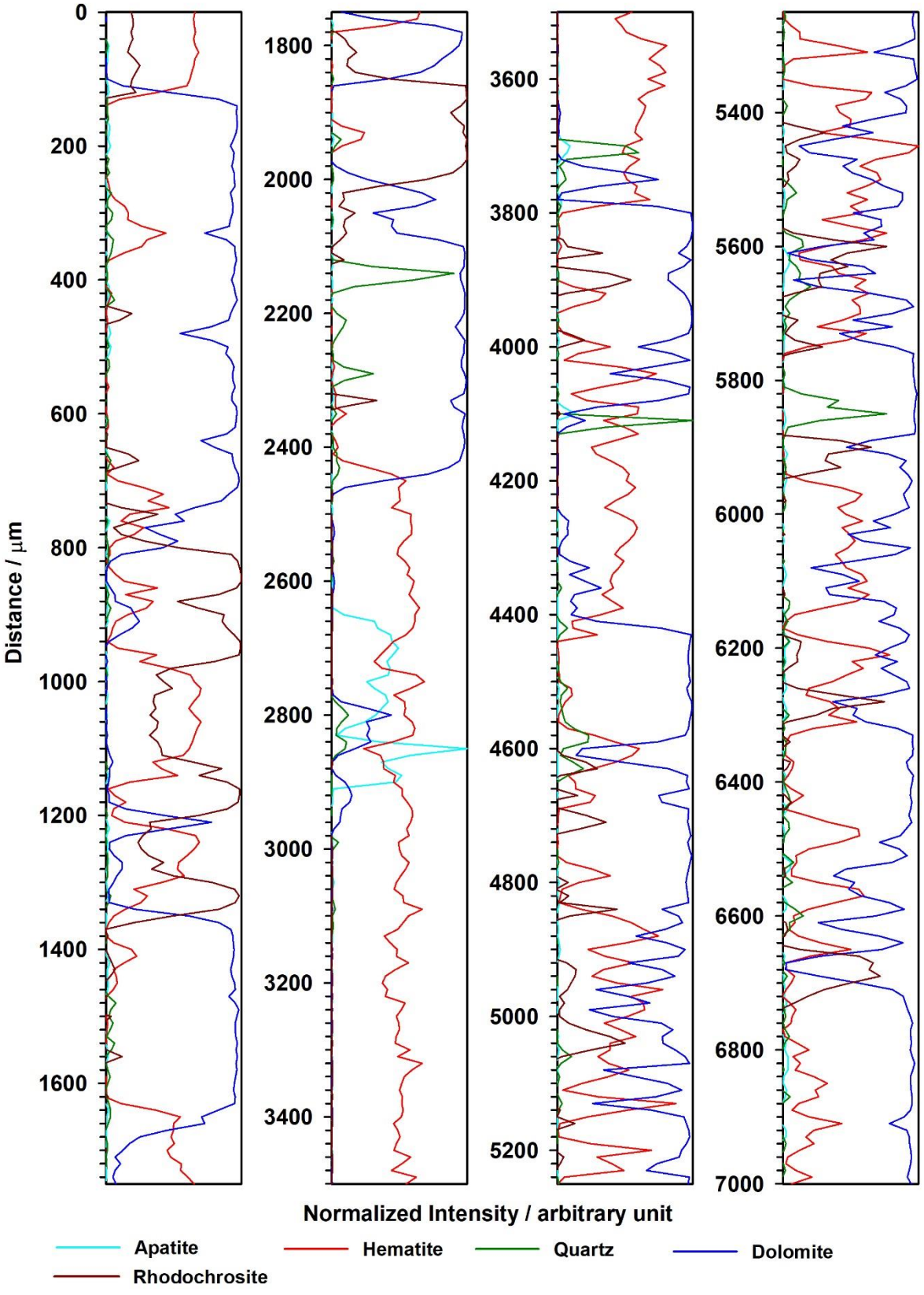
Distance / μm
0
200
400
600
800
1000
1200
1400
1600
1800
2000
2200
2400
2600
2800
3000
3200
3400
3600
3800
4000
4200
4400
4600
4800
5000
5200
5400
5600
5800
6000
6200
6400
6600
6800
7000
Normalized Intensity / arbitrary unit
Apatite
Hematite
Quartz
Dolomite
Rhodochrosite

F (141)

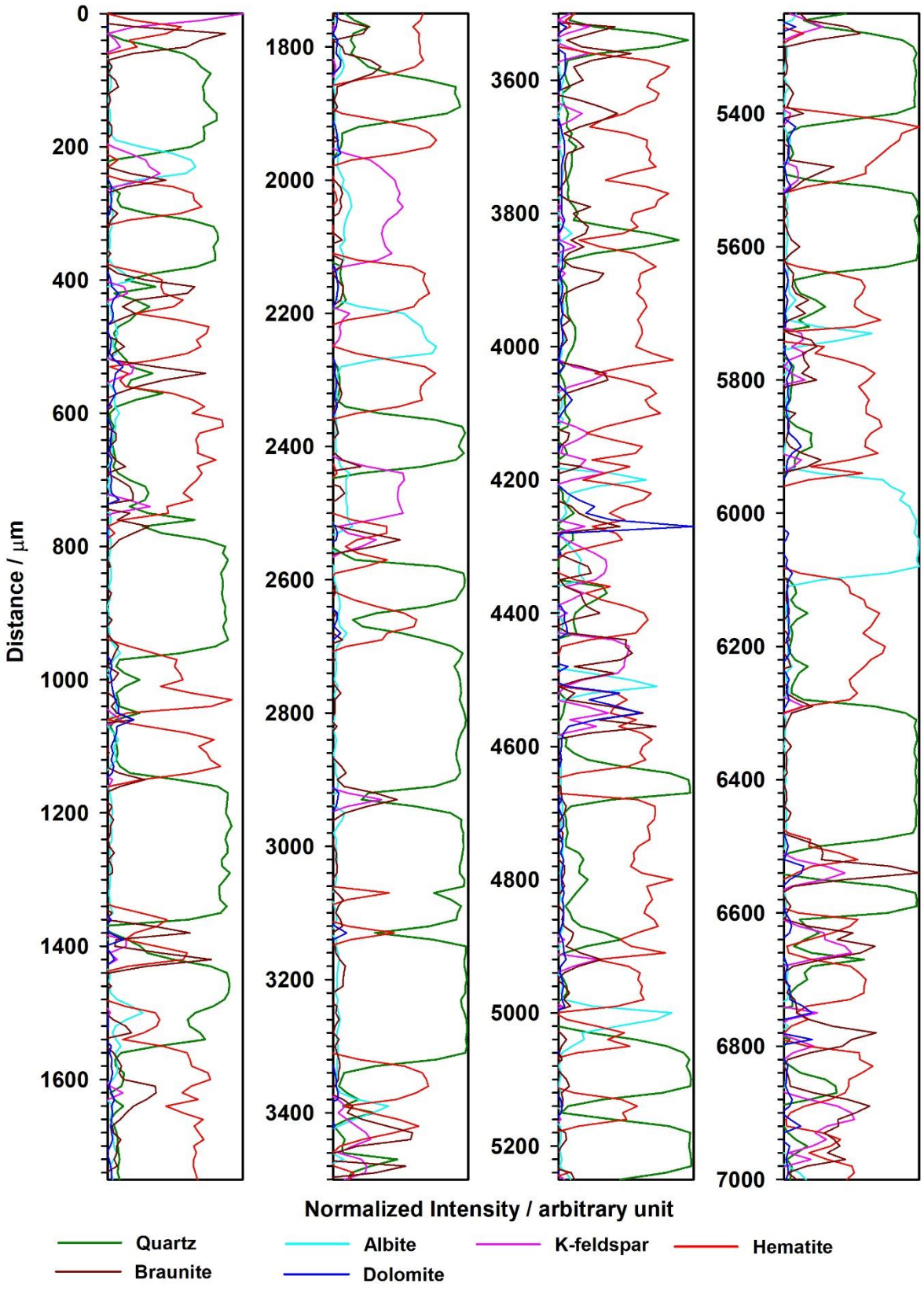
Distance / μm
0
200
400
600
800
1000
1200
1400
1600
1800
2000
2200
2400
2600
2800
3000
3200
3400
3600
3800
4000
4200
4400
4600
4800
5000
5200
5400
5600
5800
6000
6200
6400
6600
6800
7000
Normalized Intensity / arbitrary unit
Quartz
Albite
K-feldspar
Hematite
Braunite
Dolomite

G (153A)

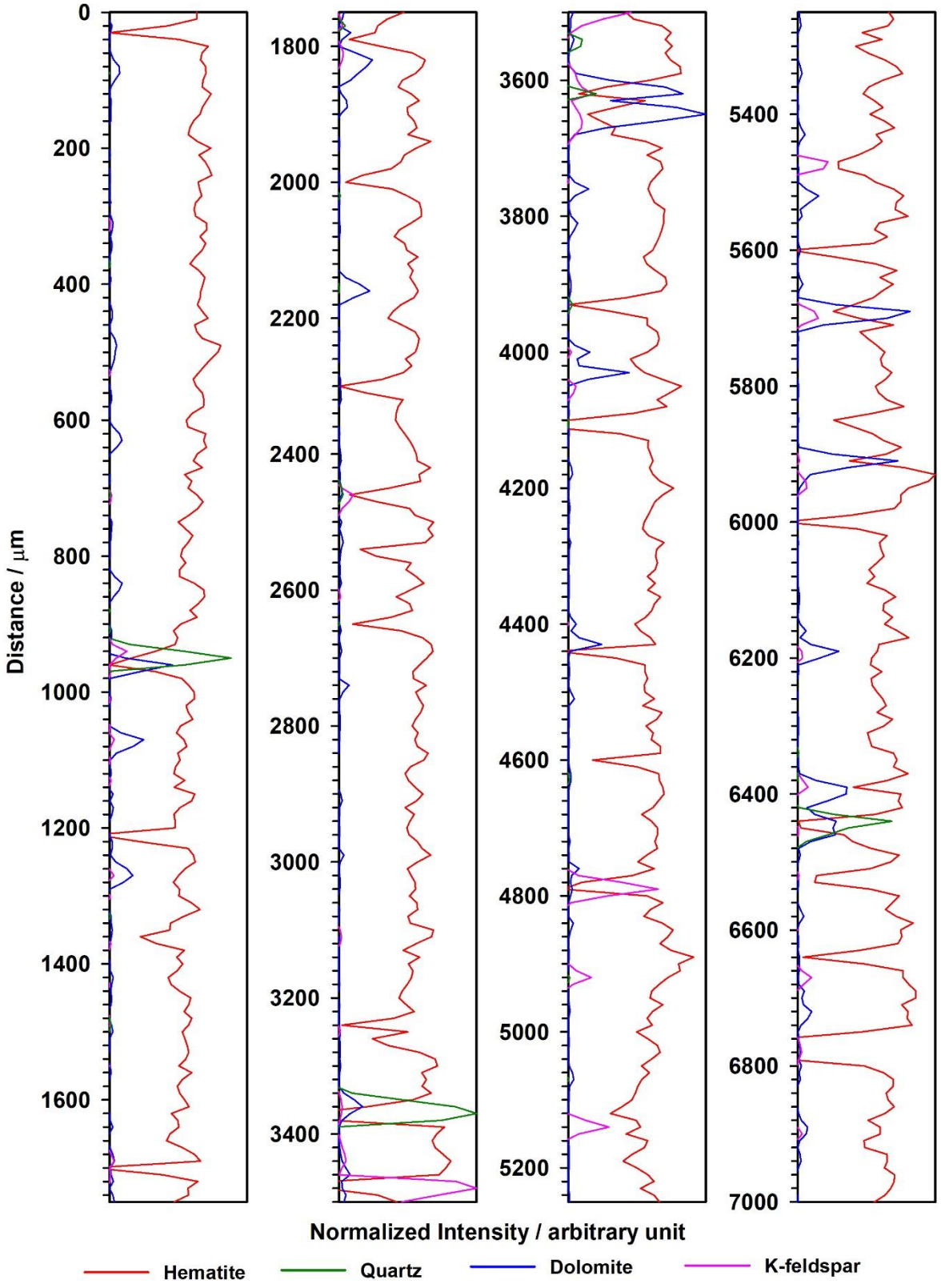
Distance / μm
0
200
400
600
800
1000
1200
1400
1600
1800
2000
2200
2400
2600
2800
3000
3200
3400
3600
3800
4000
4200
4400
4600
4800
5000
5200
5400
5600
5800
6000
6200
6400
6600
6800
7000
Normalized Intensity / arbitrary unit
Hematite
Quartz
Dolomite
K-feldspar

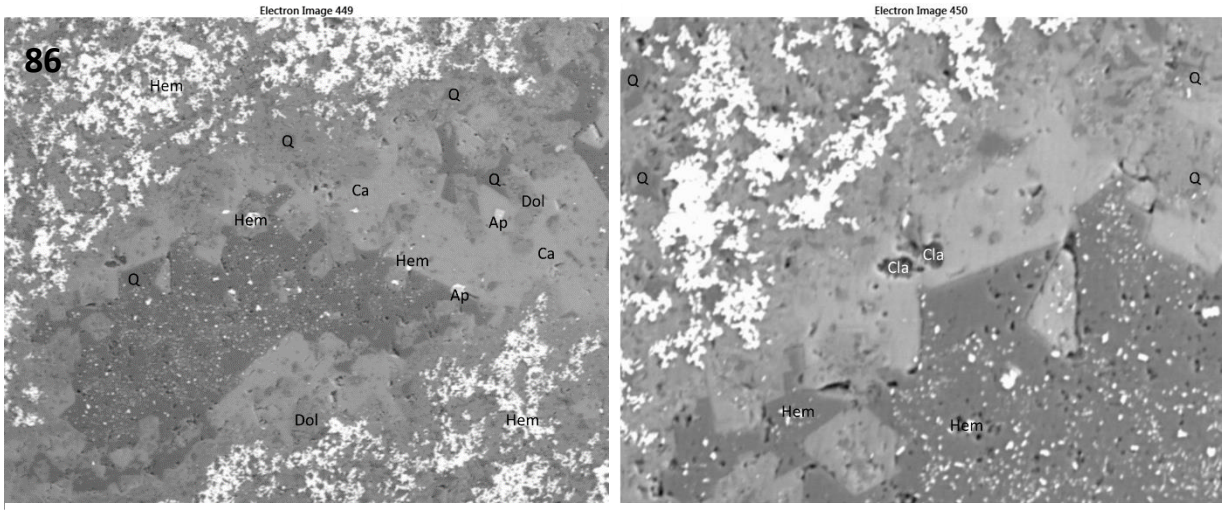

SI 9. Back scattered electron images of samples with mineral composition

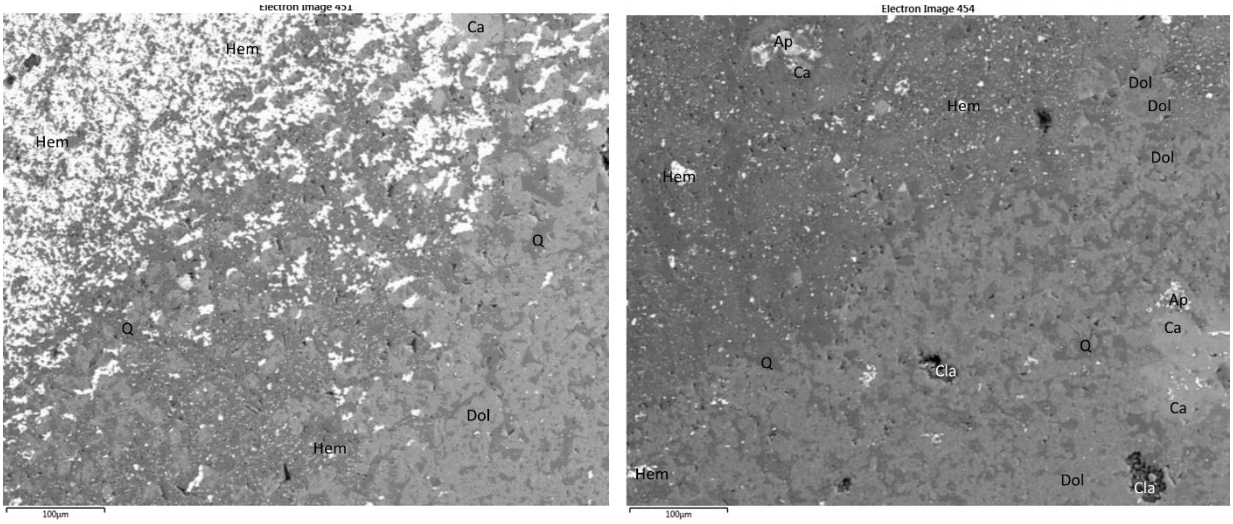

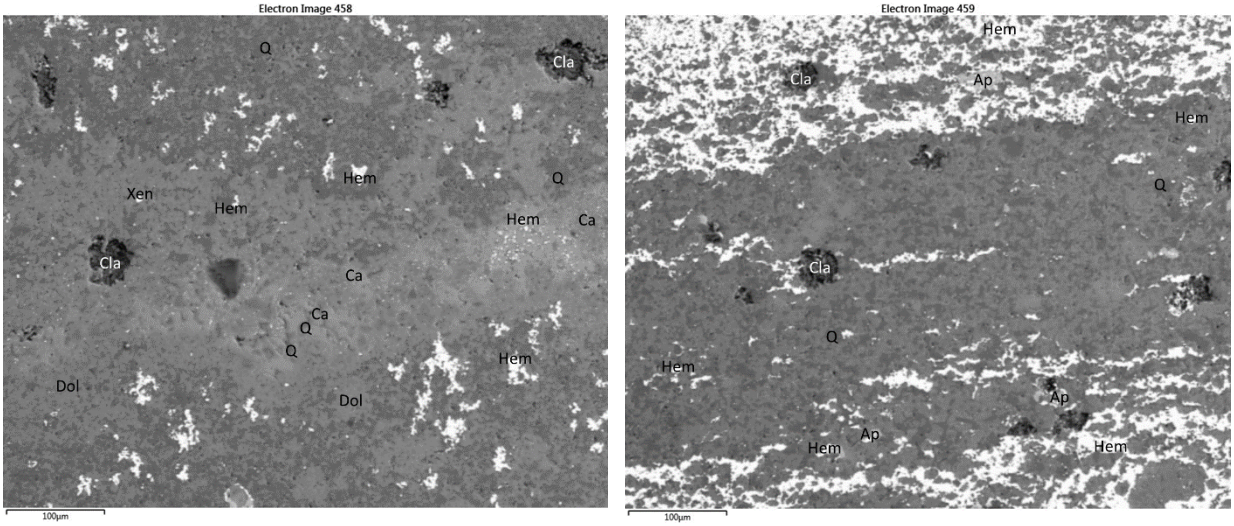

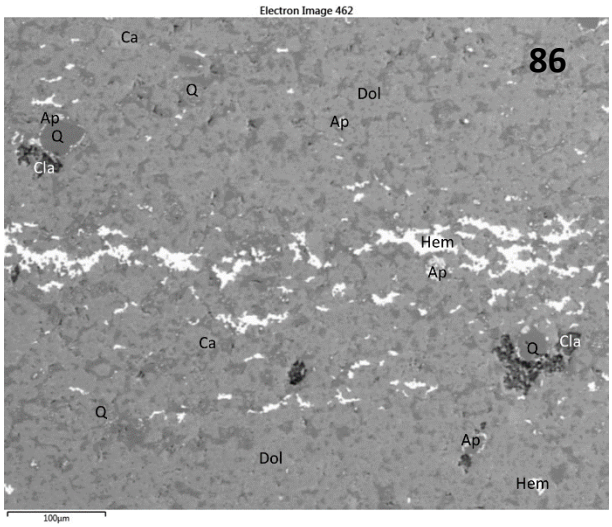
Electron Image 462
86
Ca
Q
Dol
Ap
Ap
Q
Cla
Hem
Ap
Ca
Q
Cla
Q
Ap
Dol
Hem
100µm

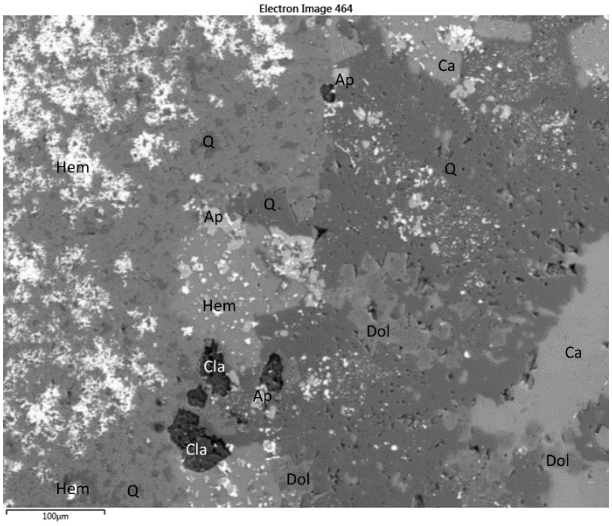
Electron Image 464
Ap
Ca
Q
Hem
Q
Q
Ap
Hem
Dol
Ca
Cla
Ap
Cla
Dol
Hem
Q
Dol
100µm

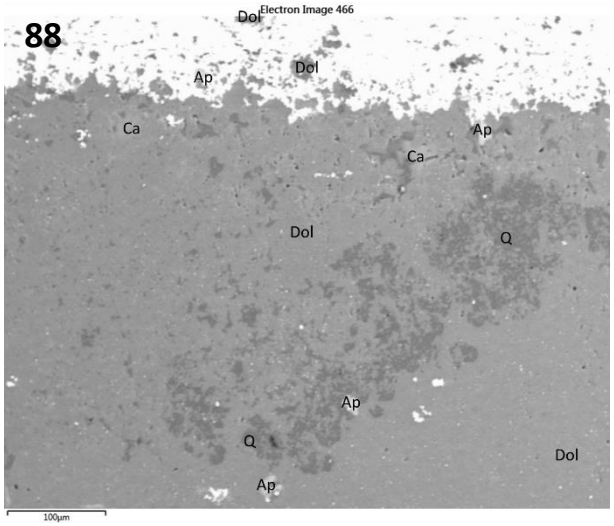
Electron Image 466
88
Dol
Ap
Dol
Ca
Ap
Ca
Dol
Q
Ap
Q
Dol
Ap
100µm

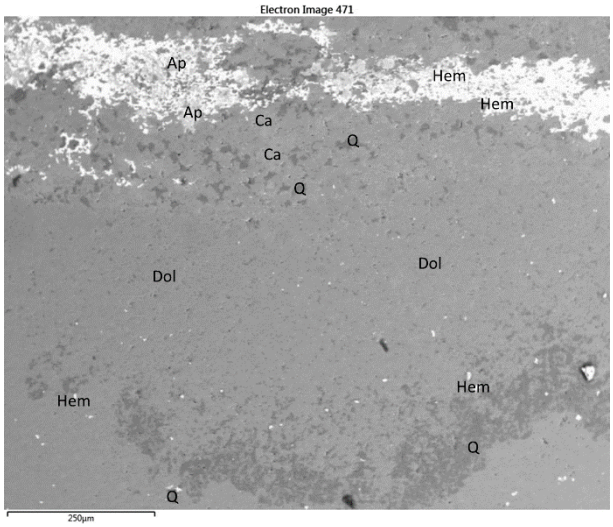
Electron Image 471
Ap
Hem
Hem
Ap
Ca
Ca
Q
Q
Dol
Dol
Hem
Hem
Q
Q
250µm

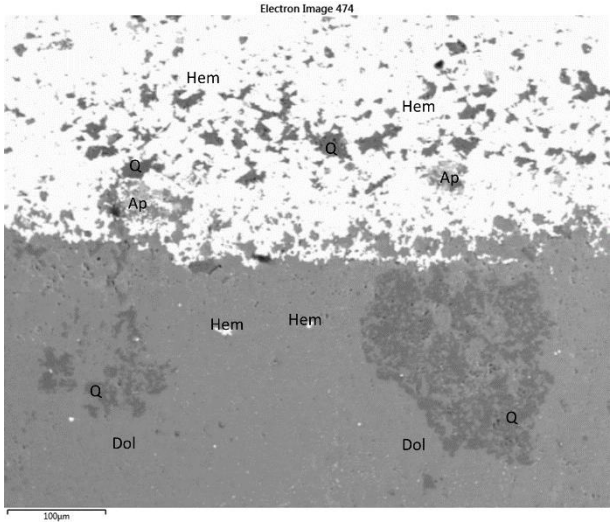
Electron Image 474
Hem
Hem
Q
Q
Ap
Ap
Hem
Hem
Q
Q
Dol
Dol
100µm

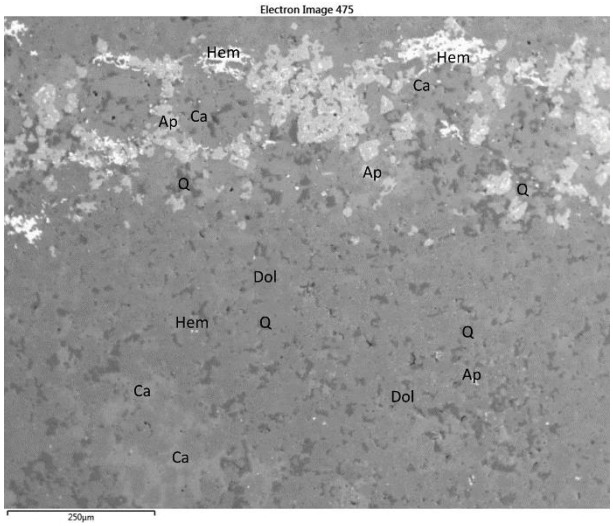
Electron Image 475
Hem
Hem
Ca
Ap
Ca
Ap
Q
Q
Dol
Hem
Q
Q
Ap
Ca
Dol
Ca
250µm

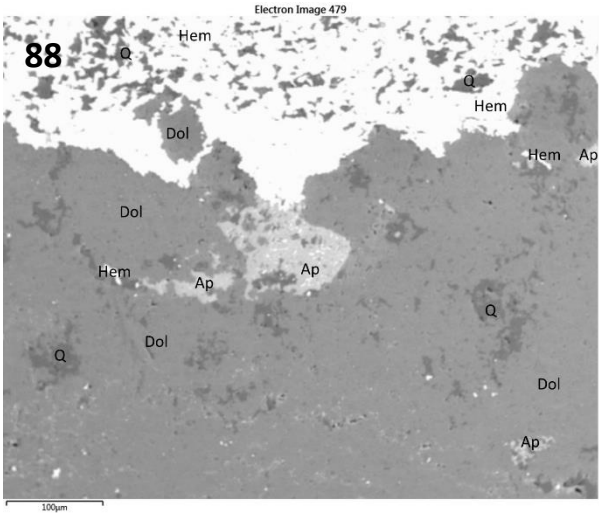
Electron Image 479
88
Hem
Q
Q
Hem
Dol
Hem
Ap
Dol
Hem
Ap
Ap
Q
Dol
Q
Dol
Ap
100µm

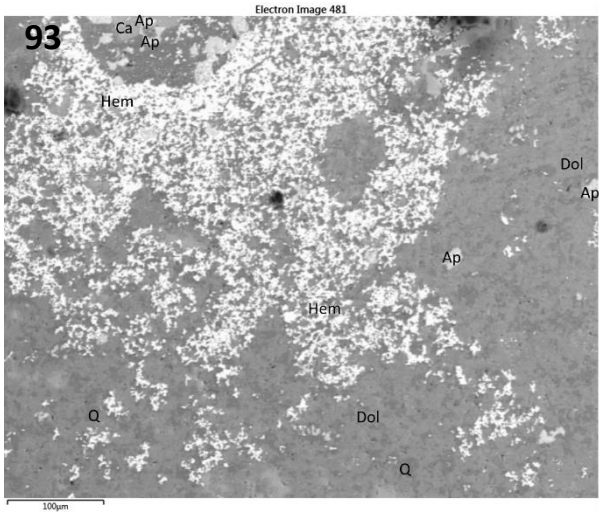
Electron Image 481
93
Ca
Ap
Ap
Hem
Dol
Ap
Ap
Hem
Q
Dol
Q
100µm

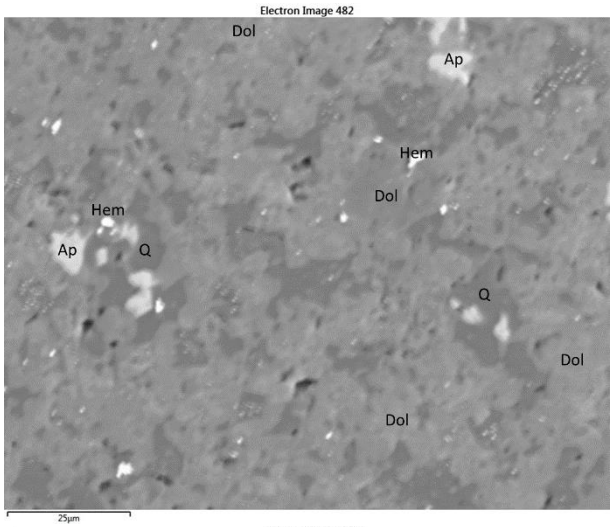
Electron Image 482
Dol
Ap
Hem
Dol
Hem
Ap
Q
Q
Dol
Dol
25µm

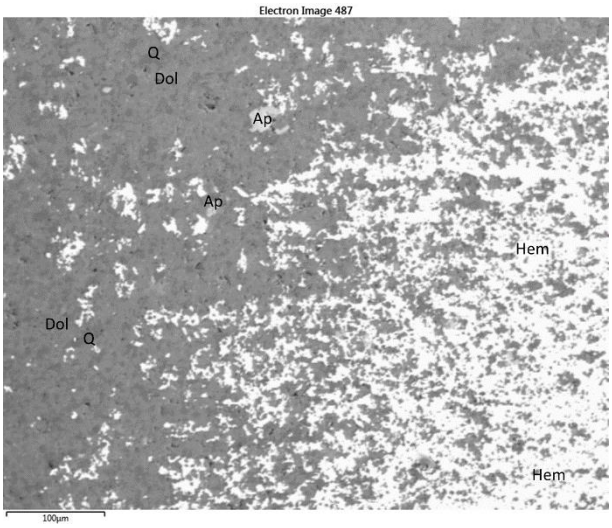
Electron Image 487
Q
Dol
Ap
Ap
Hem
Dol
Q
Hem
100µm

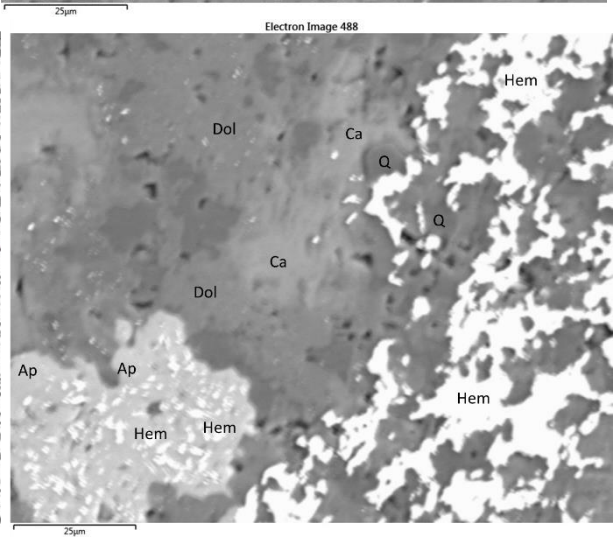
Electron Image 488
Hem
Dol
Ca
Q
Q
Ca
Dol
Ap
Ap
Hem
Hem
Hem
25µm

Electron Image 489

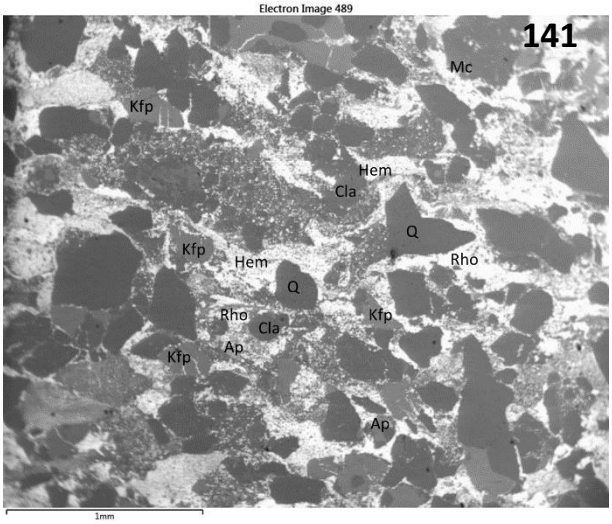

Electron Image 491

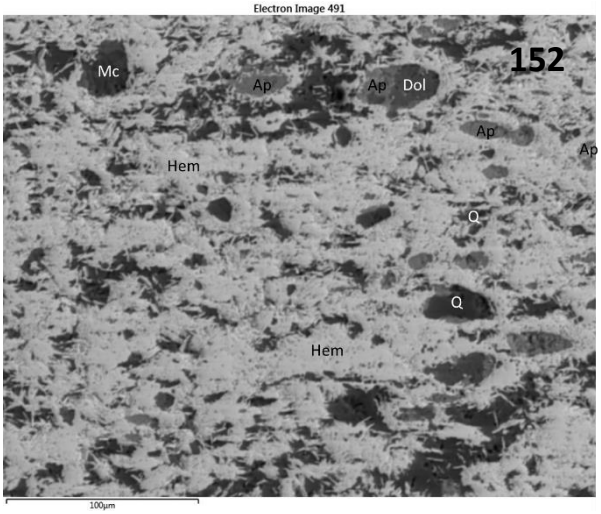

Electron Image 492

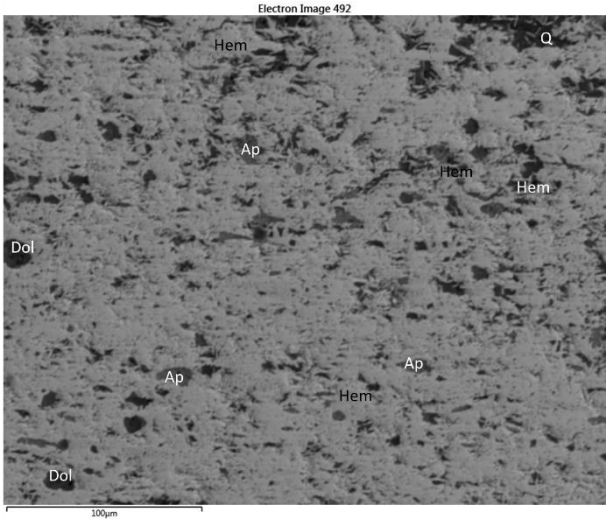

Electron Image 497

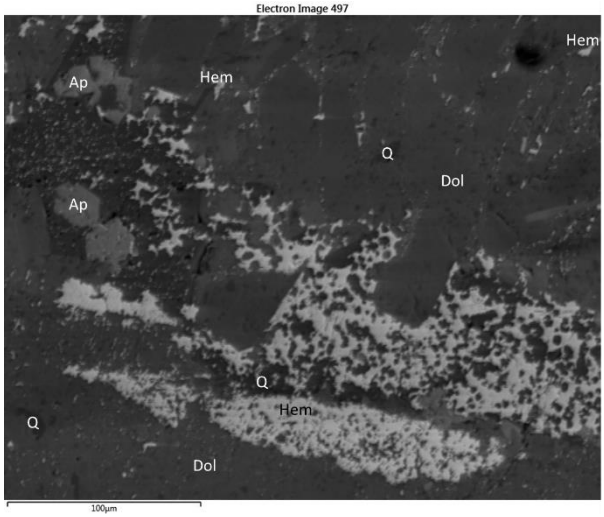

Electron Image 498

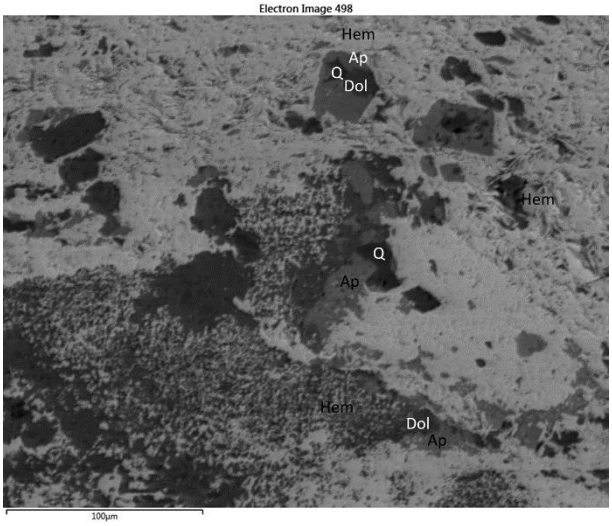

Electron Image 500

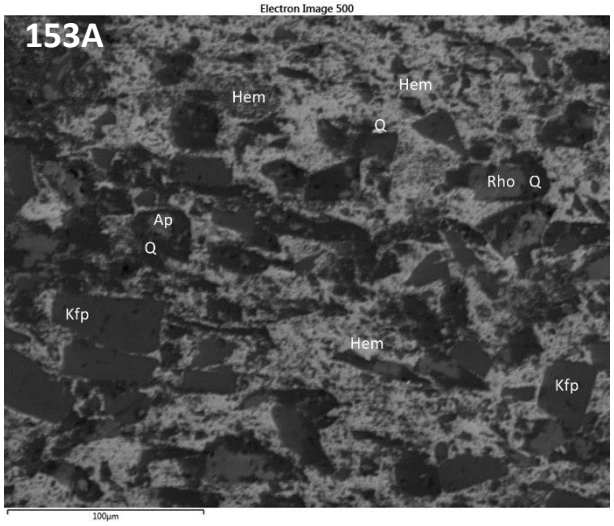

Electron Image 501

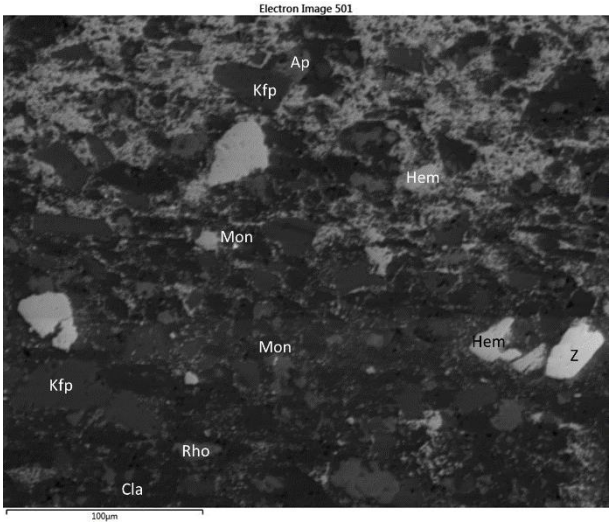

Electron Image 505

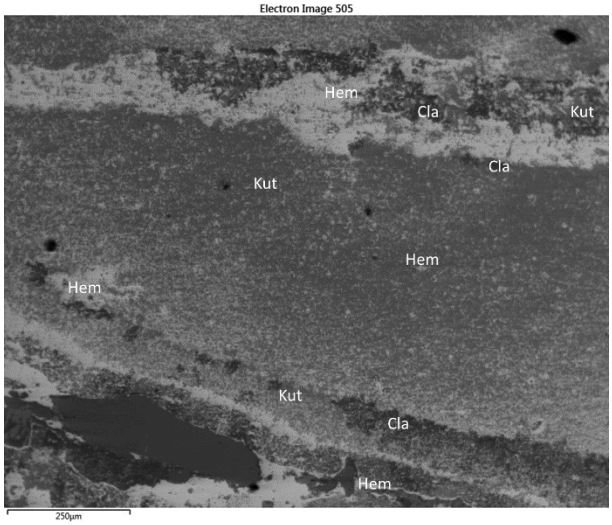

Electron Image 507

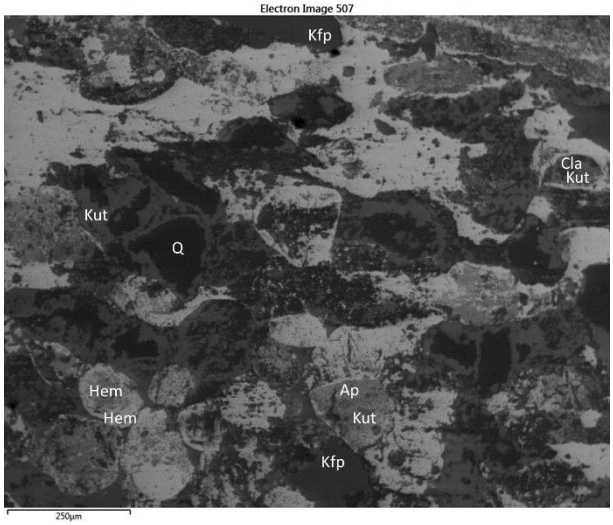

Electron Image 512

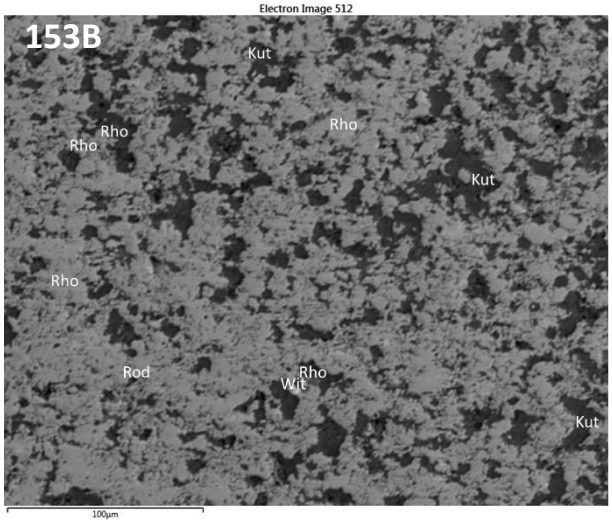

Electron Image 513

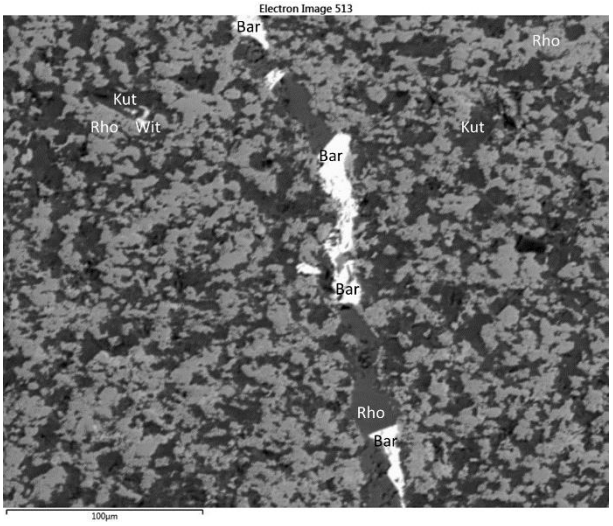

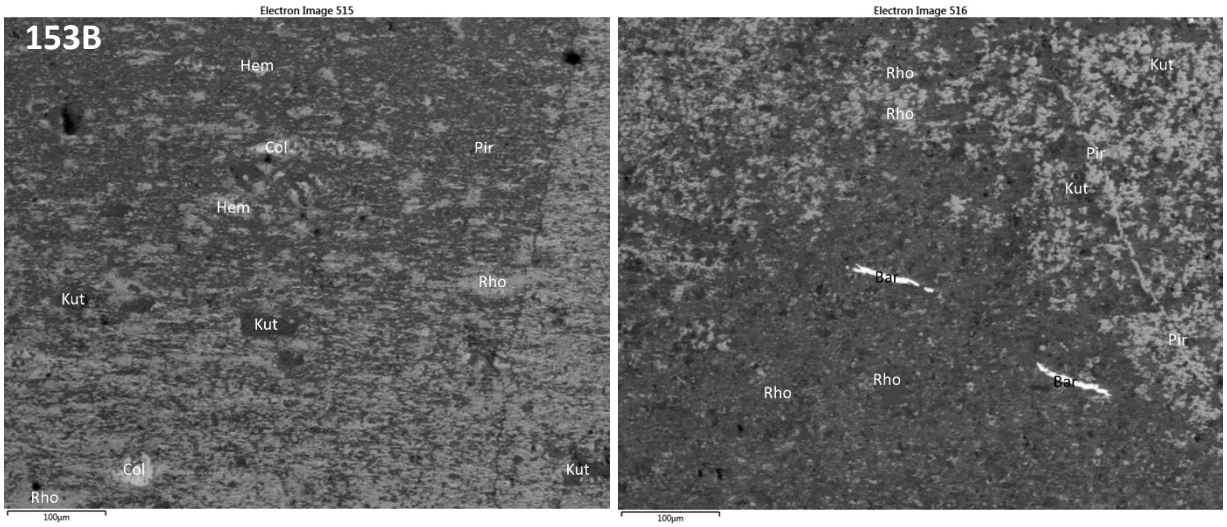

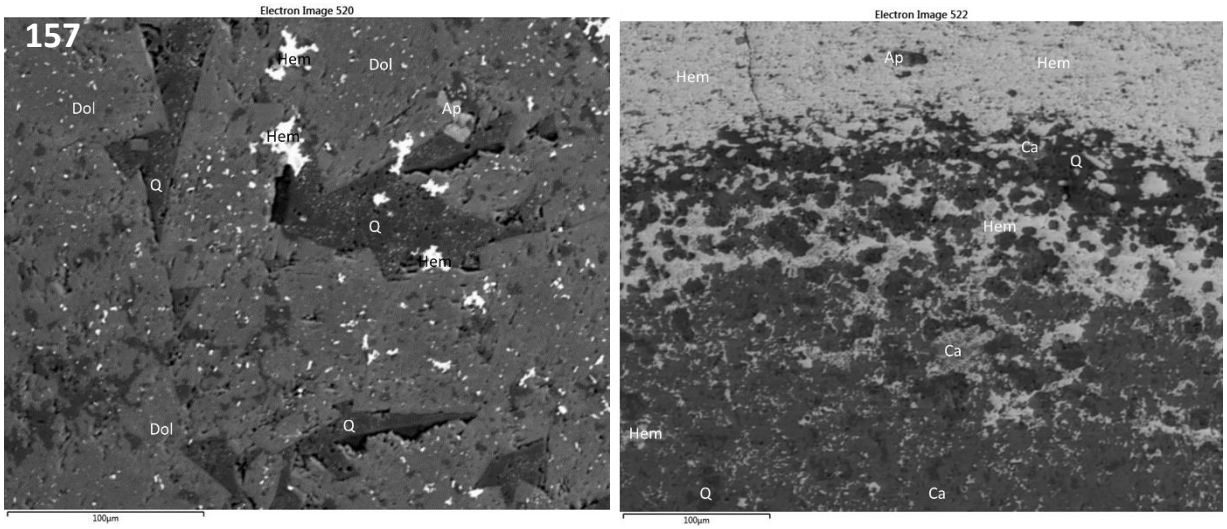

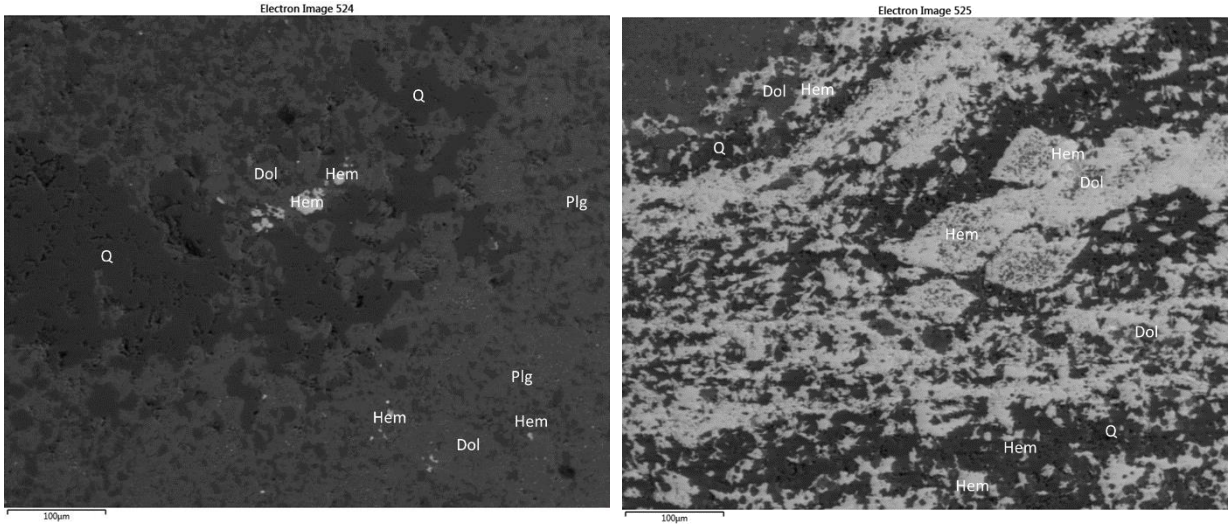

Legend: Q-quartz, Hem-hematite, Ca-calcite, Dol-double structure (dolomite-structure) carbonate, Ap-apatite, Cla-clay mineral, Xen-xenotime, Kfp-K-feldspar, Mc-mica, Rho-rhodochrosite, Mon-monacite, Z-zircon, Kut-kutnohorite, Wit-withertite, Col-cölestine, Bar-barite, Pir-pyrite, Plg-plagioclase
(dolomite represent mixed carbonates with variable composition)

SI 10. Element map images in a complex system with OM, CL, FTIR, Raman and stable isotope datasets

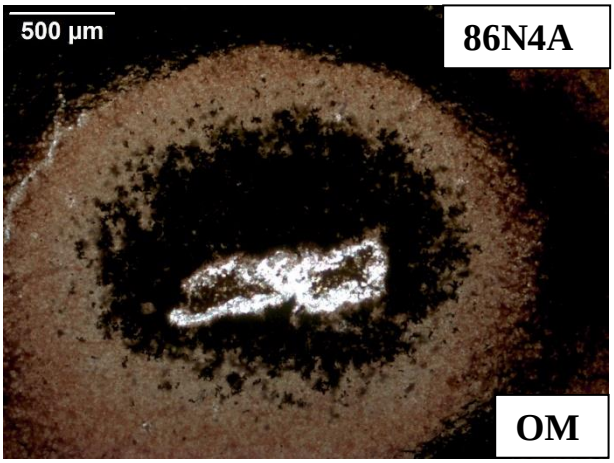

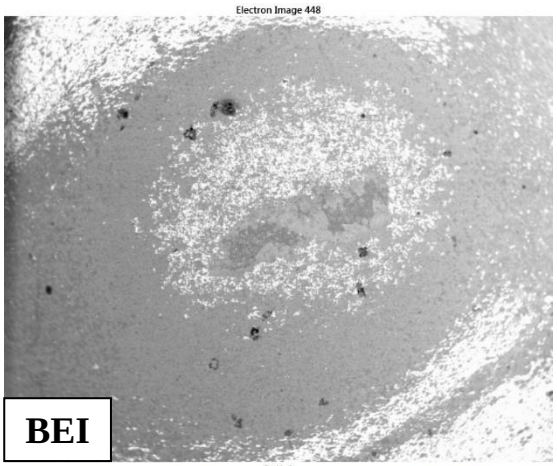

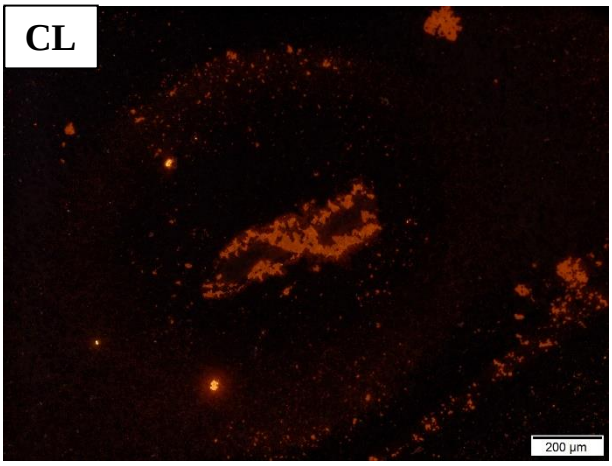

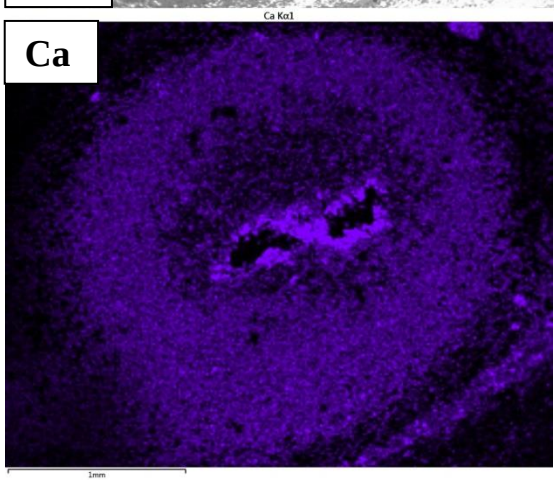

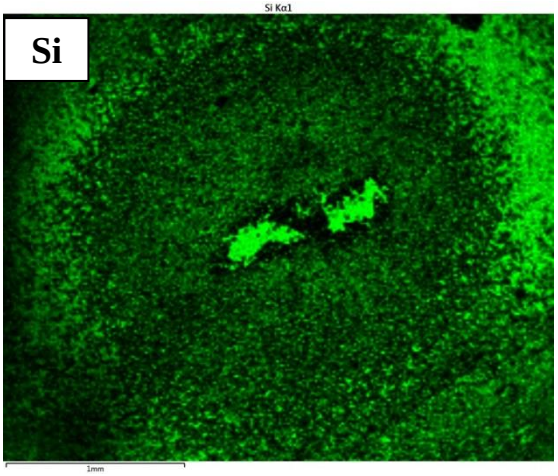

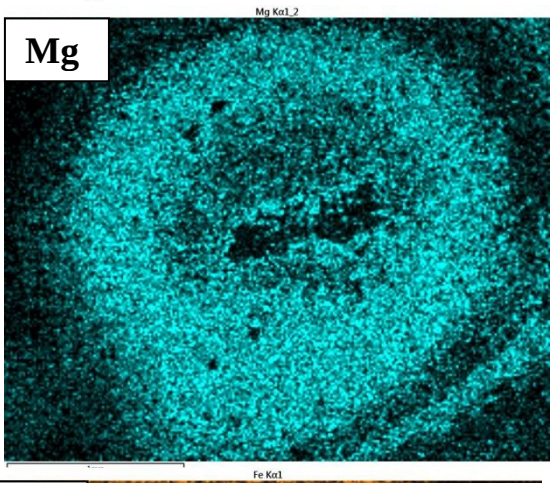

The high Si in the core indicates the presence of quartz. This is followed by Ca (Mg) enrichment, indicating the presence of calcite (dolomite)(CL), and an increase in Fe but slight decrease in Fe-Mg indicates the presence of iron oxides (hematite, goethite, ferrihydrite) and Fe-dolomite-ankerite. The Ca-Mg increase in the outer region is Fe-dolomite-ankerite. The matrix around the nodule contains a higher amount of Si and Fe, indicating the presence of iron oxides, silica, and possible nontronite. Occasionally, high P concentration occurs in a tiny area, indicating the presence of apatite. $\delta^{13}C_{PDBcarb}$ -3.38 ‰; $\delta^{18}O_{PDBcarb}$ -4.52 ‰
T: 45.1 °C

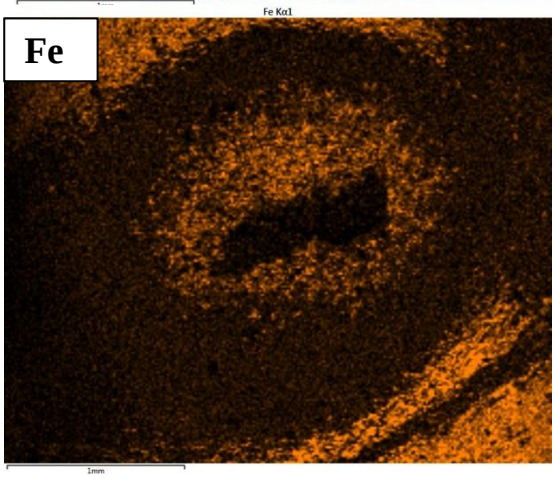

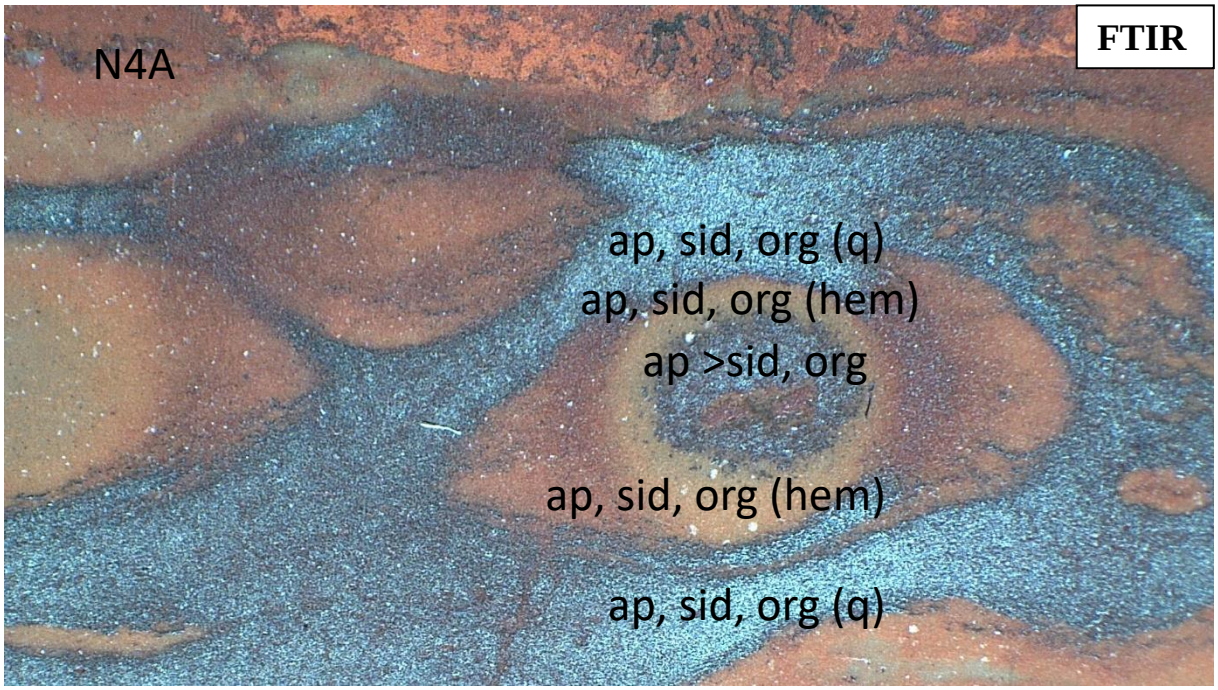
FTIR
N4A
ap, sid, org (q)
ap, sid, org (hem)
ap >sid, org
ap, sid, org (hem)
ap, sid, org (q)

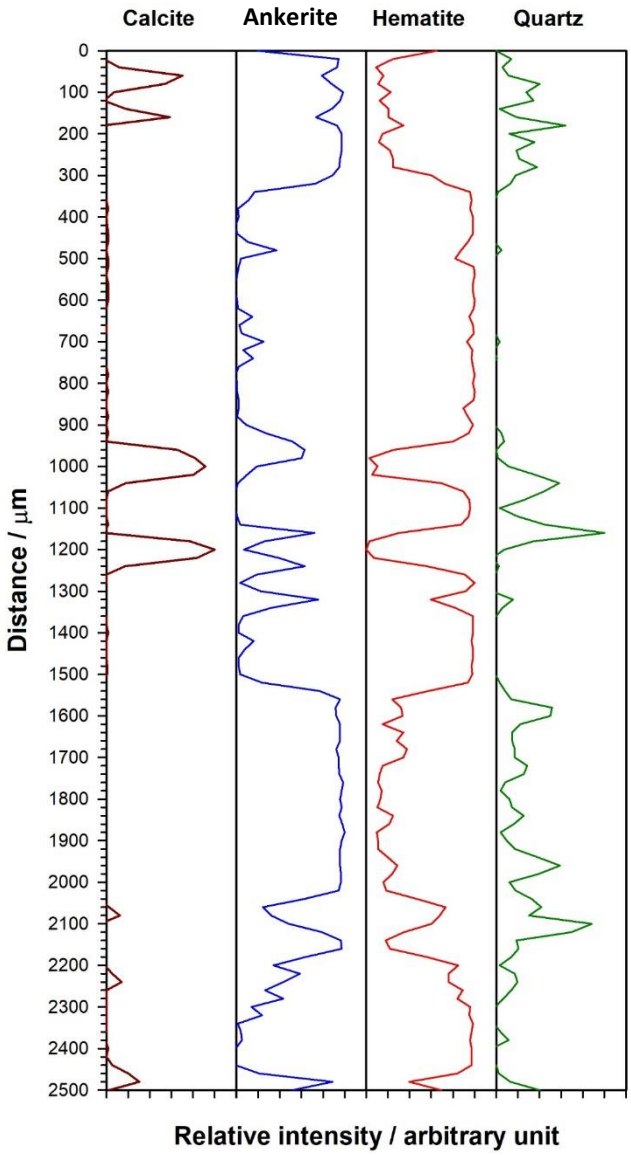
Calcite
Ankerite
Hematite
Quartz
Distance / µm
Relative intensity / arbitrary unit

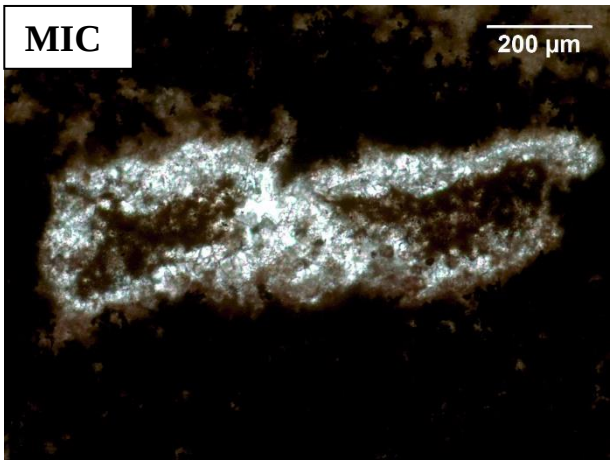
MIC
200 µm

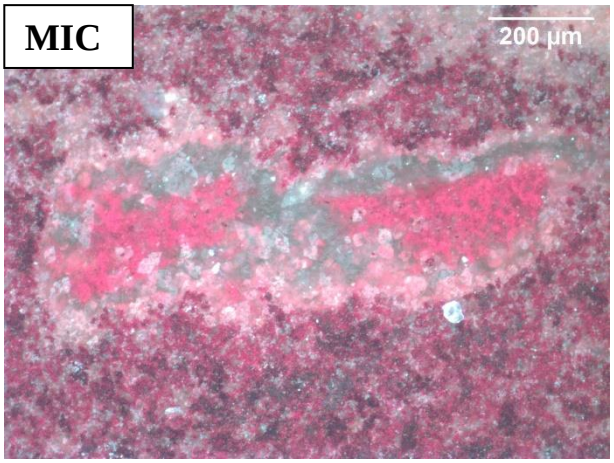
MIC
200 µm

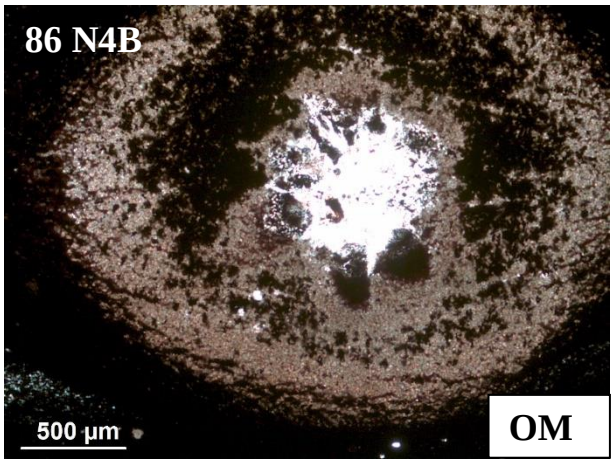
86 N4B
500 µm
OM

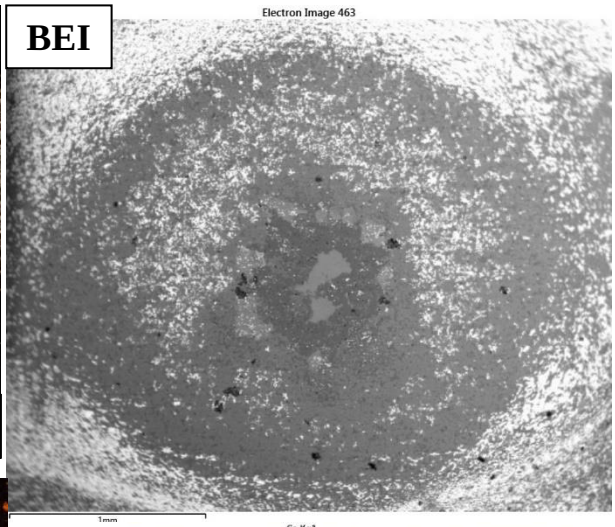
BEI
Electron Image 463

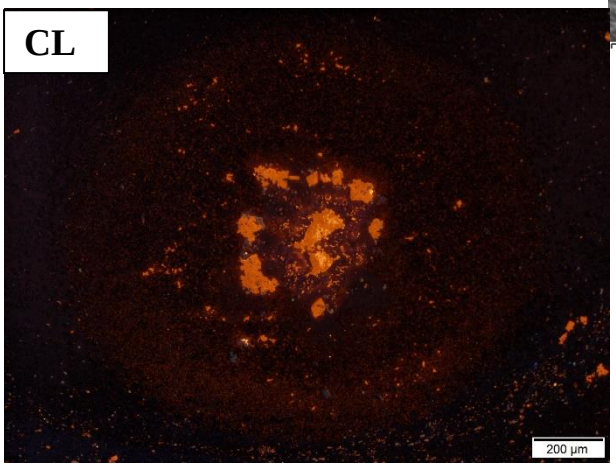
CL
200 µm

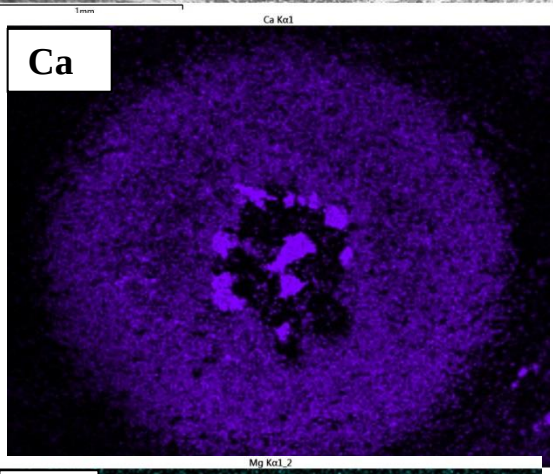
Ca
Ca Kα1

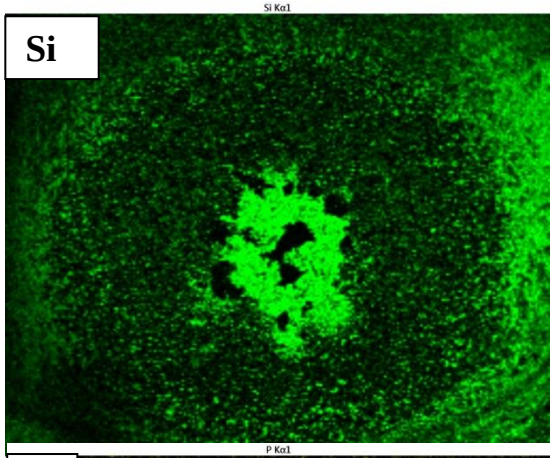
Si
Si Kα1

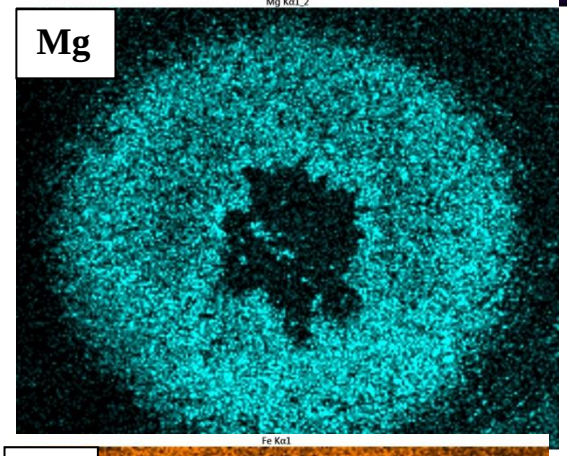
Mg
Mg Kα1_2

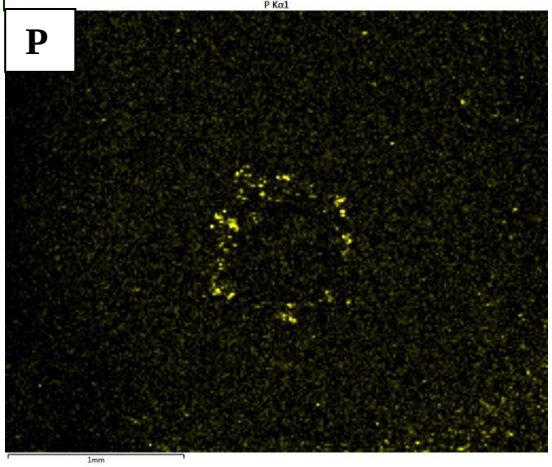
P
P Kα1

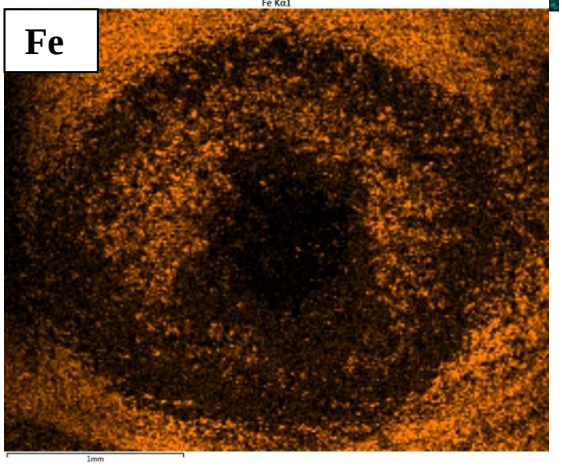
Fe
Fe Kα1

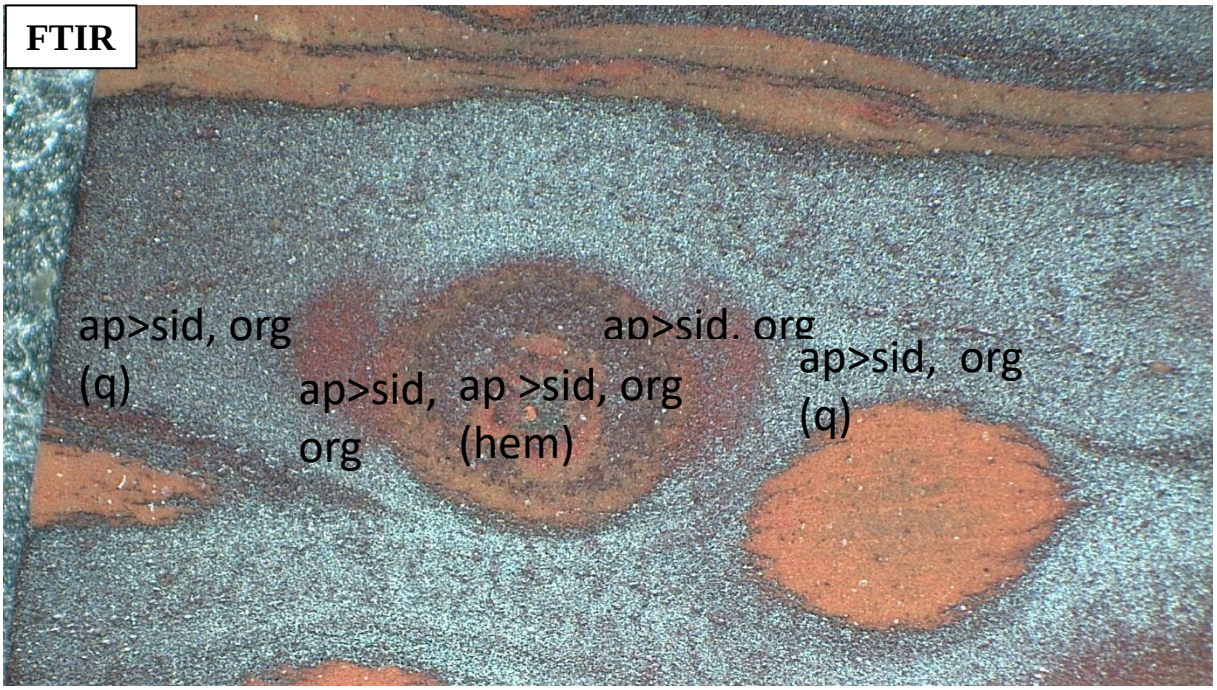

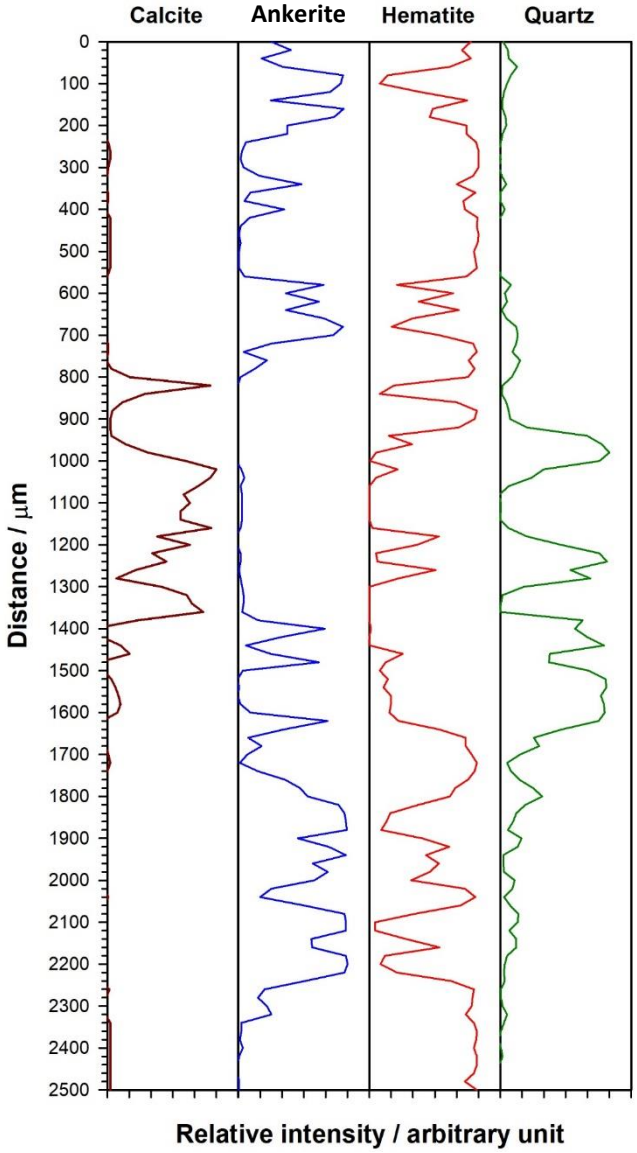

High Si suggests a quartz-rich core region, which is rimmed by apatite (high Ca, P) and a thin dolomite rim (Ca, Mg). The moderate increase in Fe but lesser decrease in Ca-Mg indicates the presence of ankerite with hematite. The outer rim is rich in Ca-Mg, indicating dolomite. The matrix contains Si-Fe laminatiton, indicating dissemination (merging) of iron oxides and quartz.
$\delta^{13}C_{PDBcarb}$ -3.38 ‰; $\delta^{18}O_{PDBcarb}$ -4.52 ‰
T: 45.1 °C

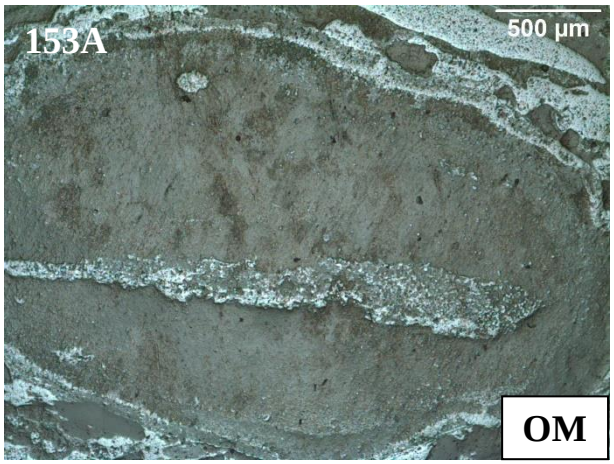
153A
500 µm
OM


Electron Image 504
BEI
1mm

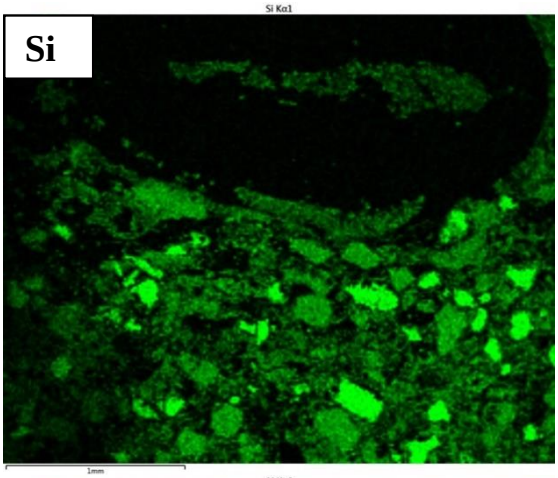
Si Kα1
Si
1mm

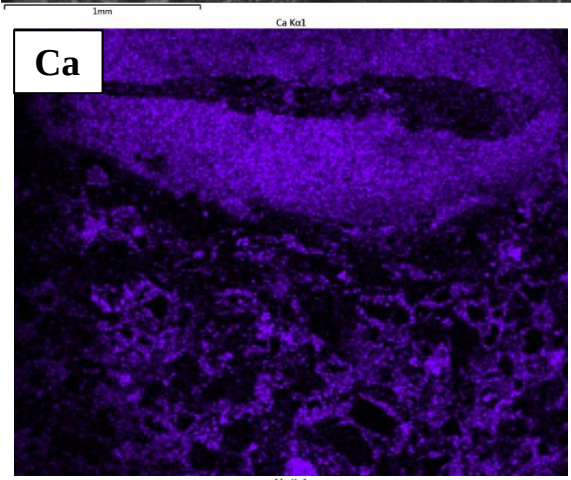
Ca Kα1
Ca

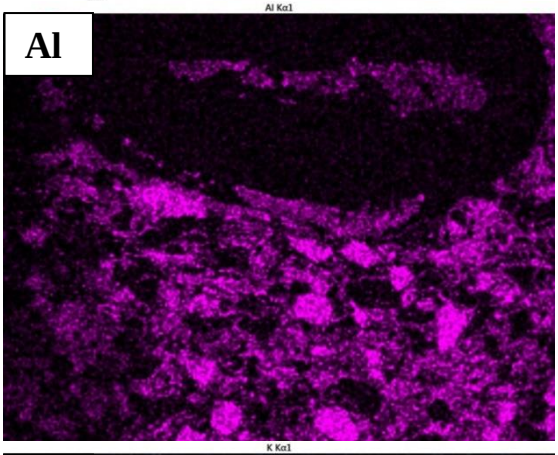
Al Kα1
Al

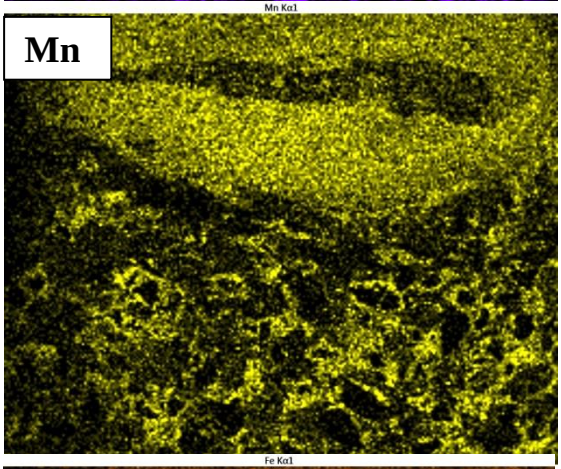
Mn Kα1
Mn

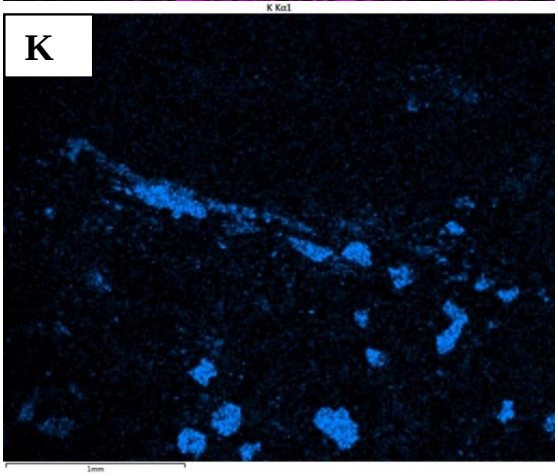
K Kα1
K
1mm

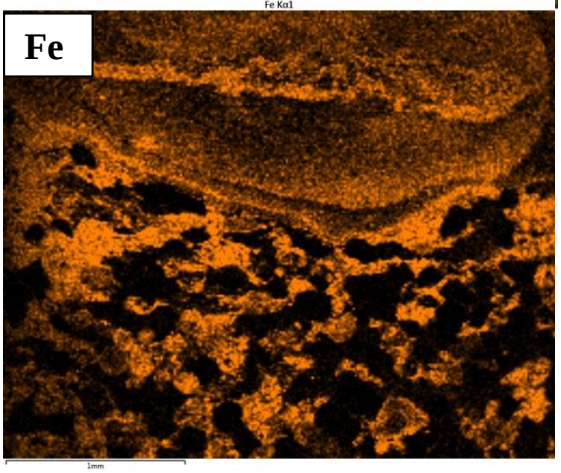
Fe Kα1
Fe
1mm

This area contains a nodule with iron-oxide (Fe) and kaolinite (Si-Al) rich core, with a Ca-Mn rich outer part with low Fe (kutnohorite). The matrix is inhomogeneous with quartz (Si) and K-feldspar (K, Al, Si) clasts, with kutnohorite (Ca, Mn) rich rims. Among the clasts are Fe-rich areas, indicating the presence of iron oxides.

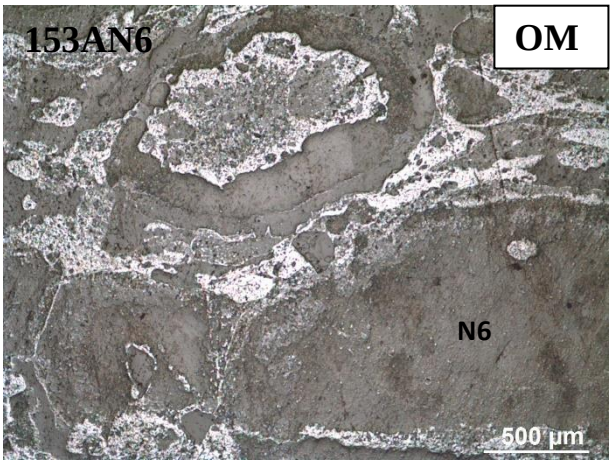
153AN6
OM
N6
500 µm

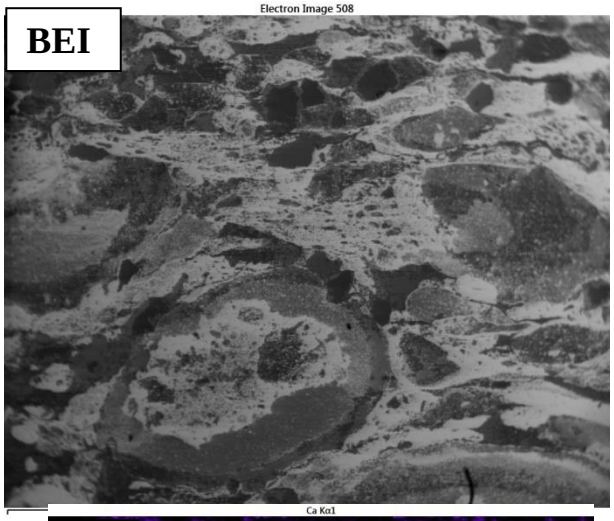
BEI
Electron Image 508

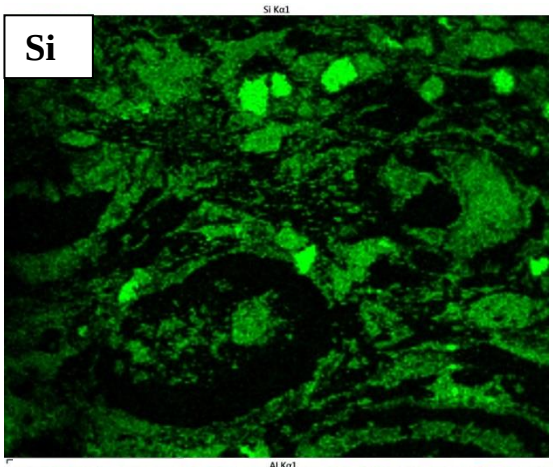
Si
Si Kα1

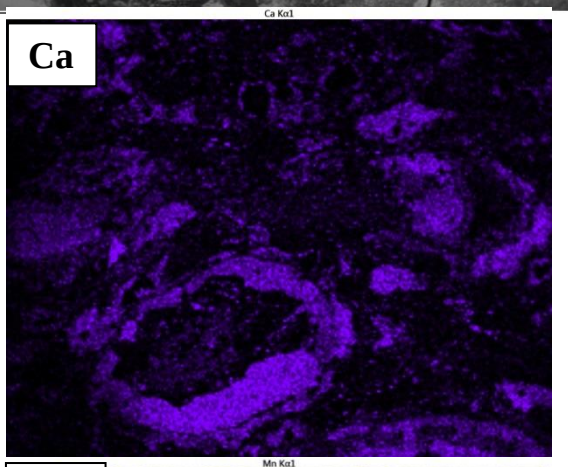
Ca
Ca Kα1

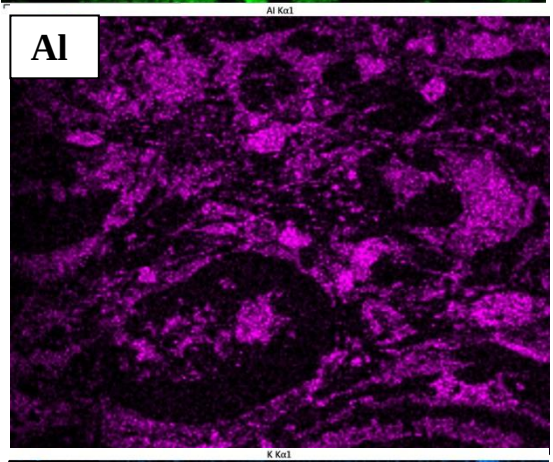
Al
Al Kα1

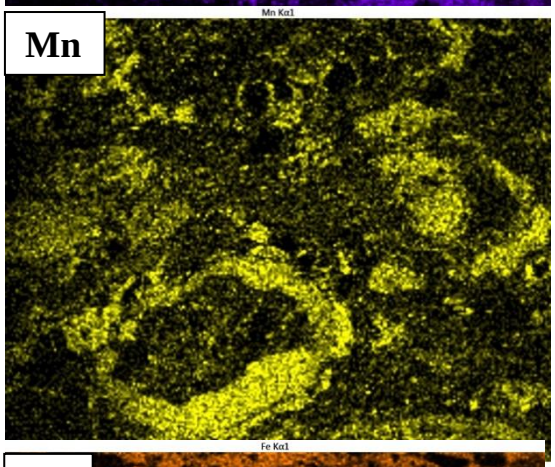
Mn
Mn Kα1

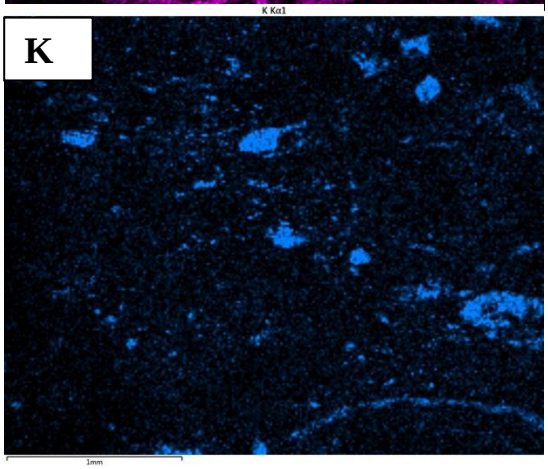
K
K Kα1
1mm

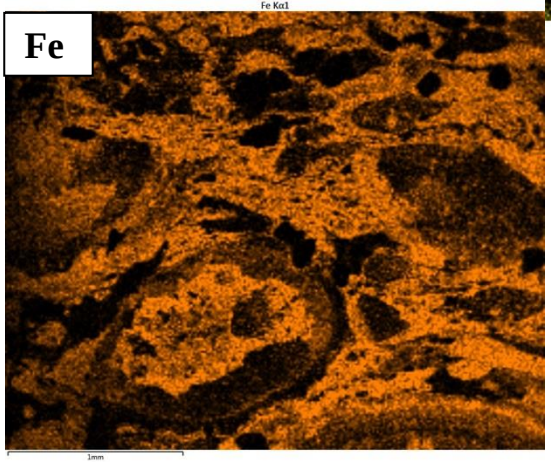
Fe
Fe Kα1
1mm

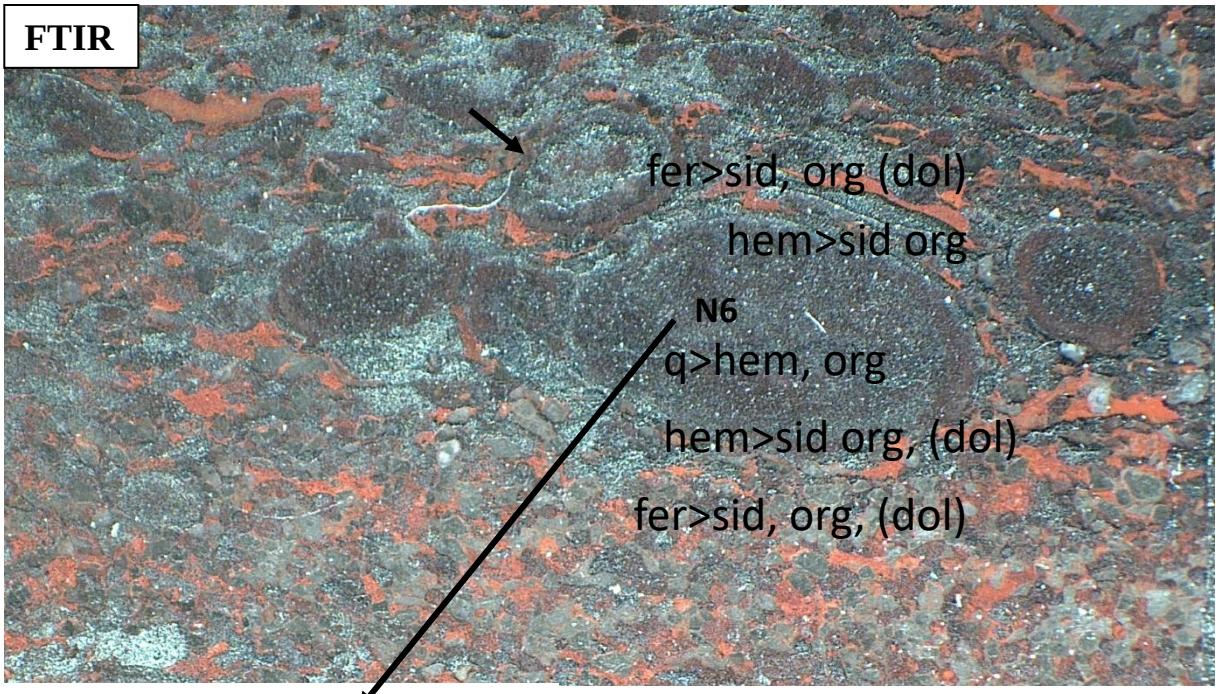

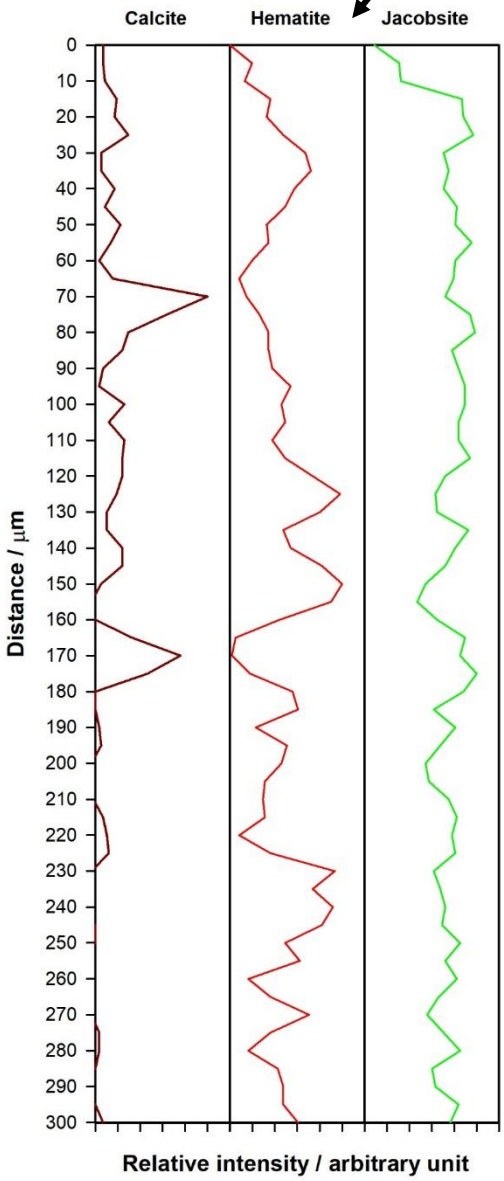

This area contain nodules with inhomogeneous structure. The core has high Si-Al (clast minerals), the outer area has higher Fe (iron oxides), and the rim is composed of kutnohorite (high Ca, Mn). The matrix is inhomogeneous with quartz (high Si), K-feldspar (K, Al, Si) embedded in iron oxides (Fe and clays (Si, Al).
$\delta^{13}C_{PDBcarb}$ -5.34 ‰; $\delta^{18}O_{PDBcarb}$ -7.98 ‰
T: 36-68 °C

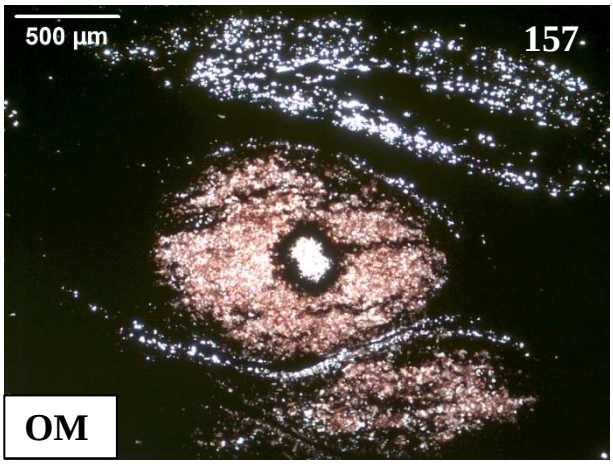
500 µm
157
OM

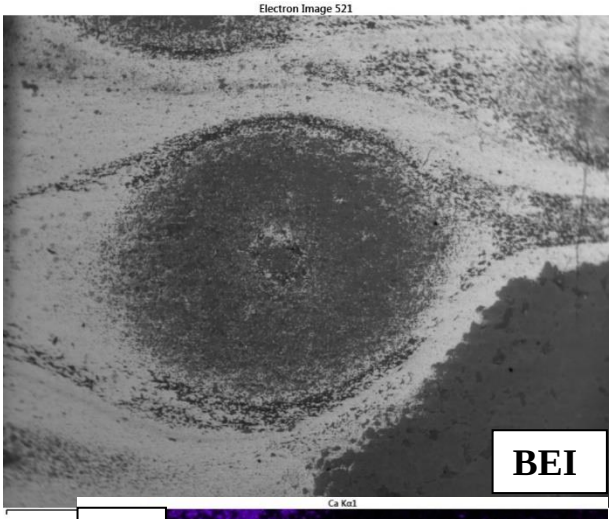
Electron Image 521
BEI

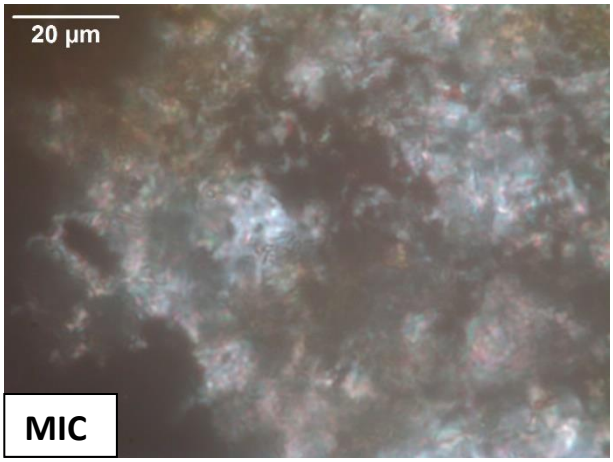
20 µm
MIC

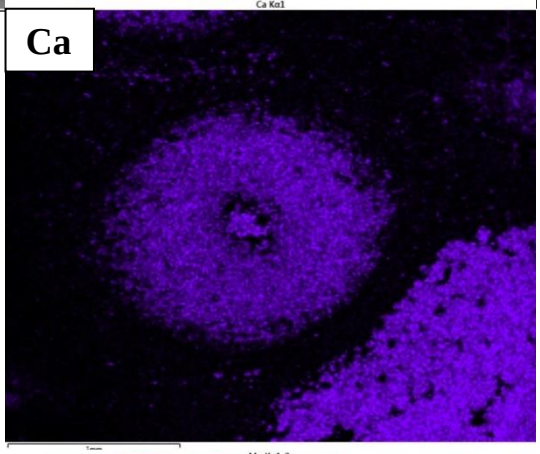
Ca Kα1
Ca

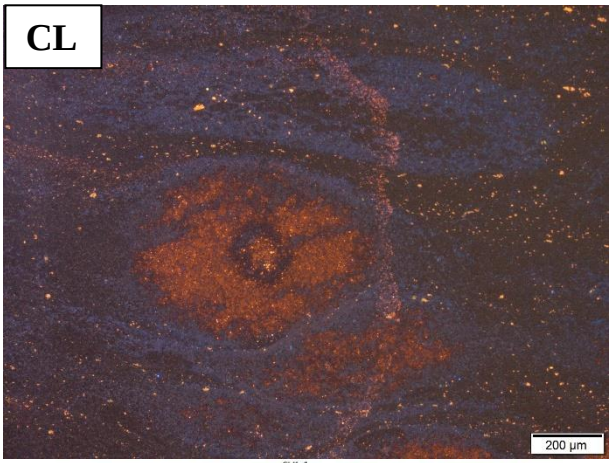
CL
200 µm

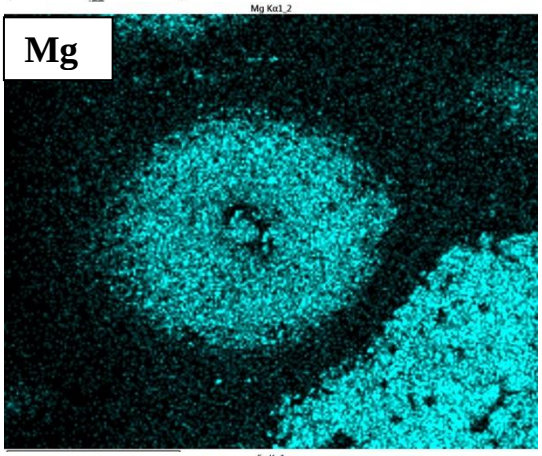
Mg Kα1_2
Mg

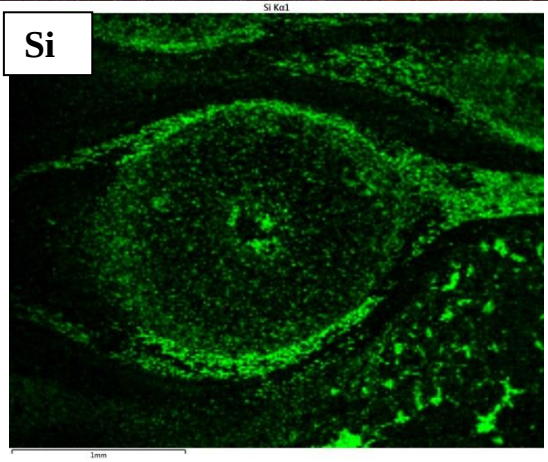
Si Kα1
Si
1mm

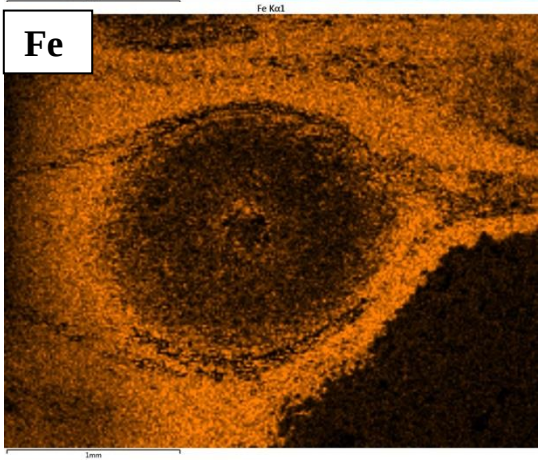
Fe Kα1
Fe
1mm

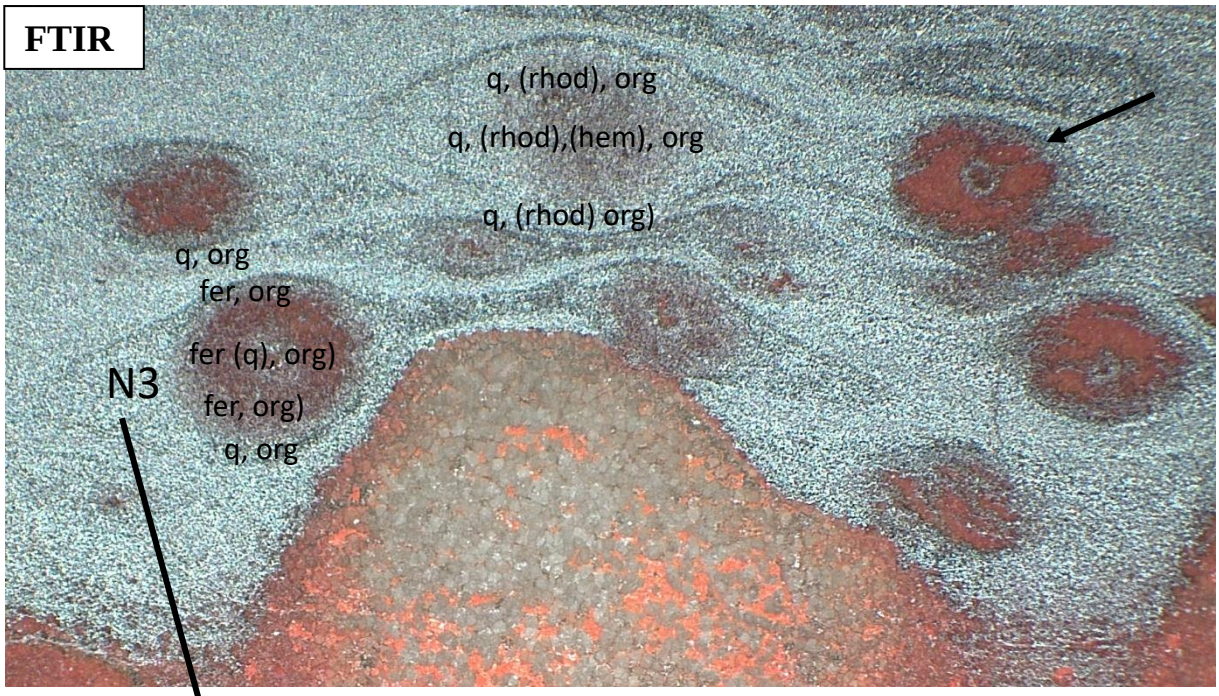

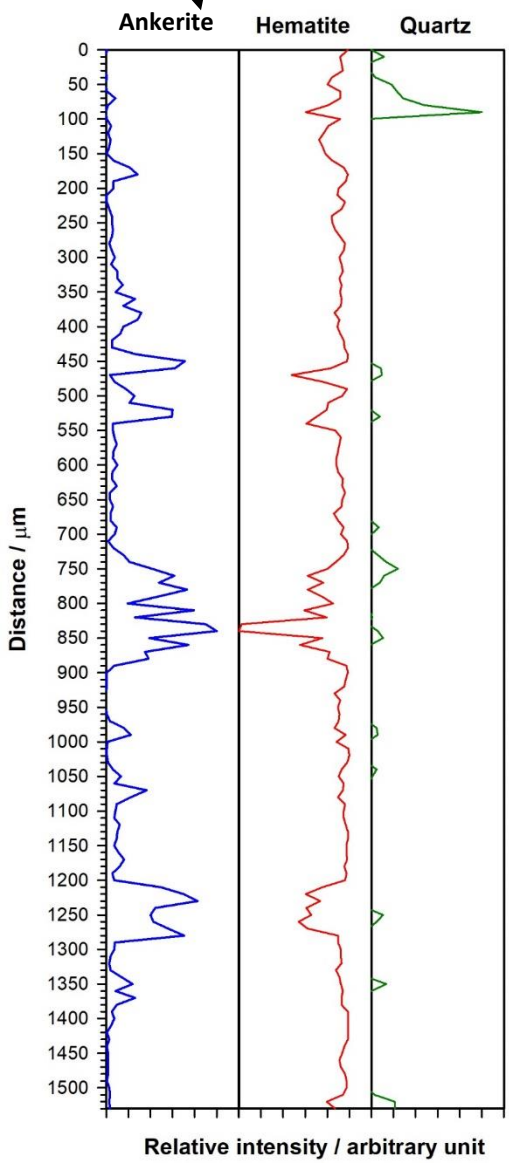

This area contains a nodule with concentric structure composing mostly dolomite (high Ca, Mg) at the rim and quartz (high Si) in the center. The matrix contains mostly iron oxide. Segregated quartz on CL is bluish. $\delta^{13}C_{PDBcarb}$ -3.92 ‰; $\delta^{18}O_{PDBcarb}$ -4.42 ‰
T: 17.9-44.5 °C

SI 11. Carbonate composition of samples based on EPMA analyses

86

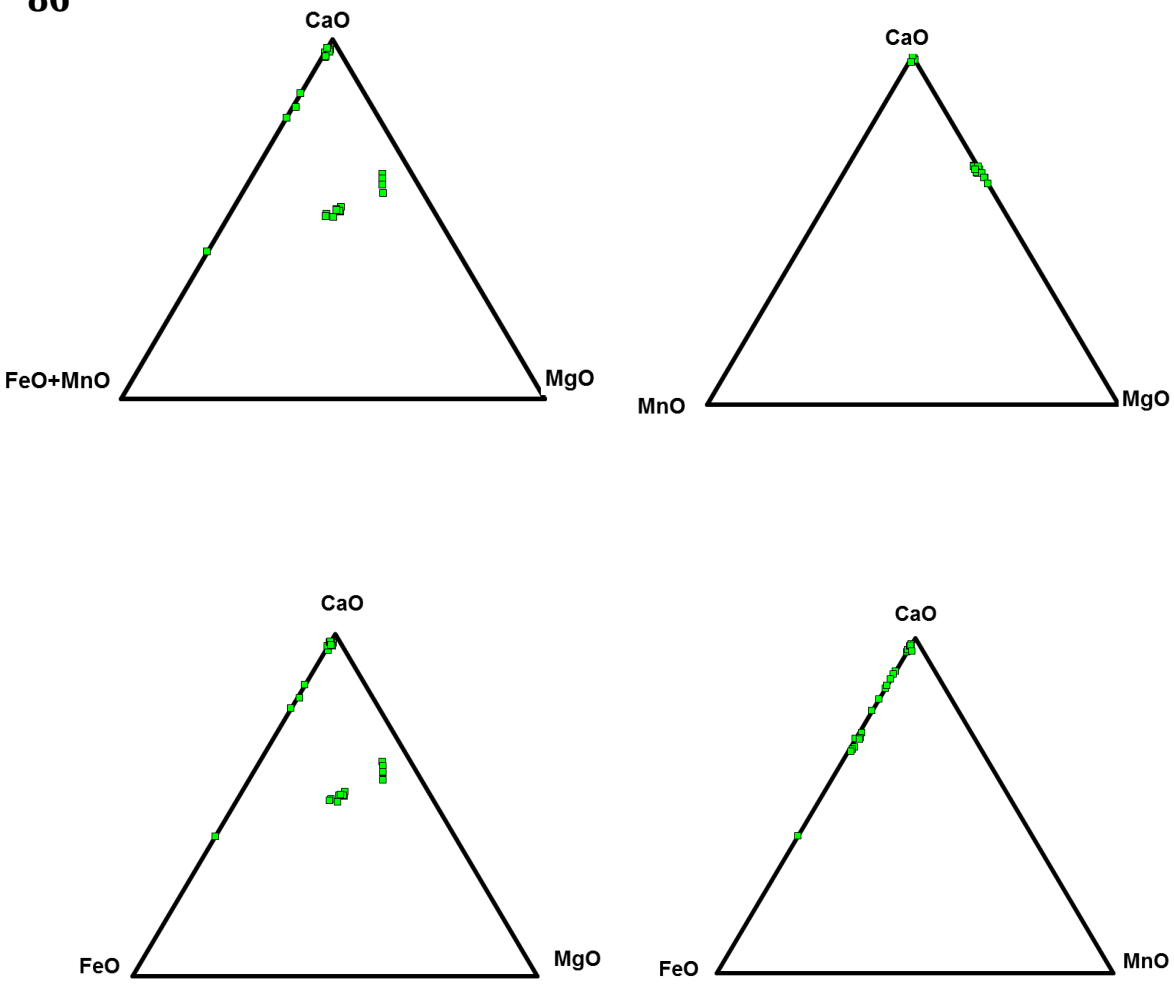

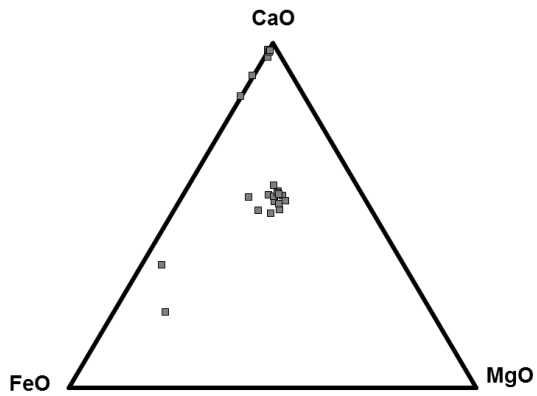
CaO
FeO
MgO

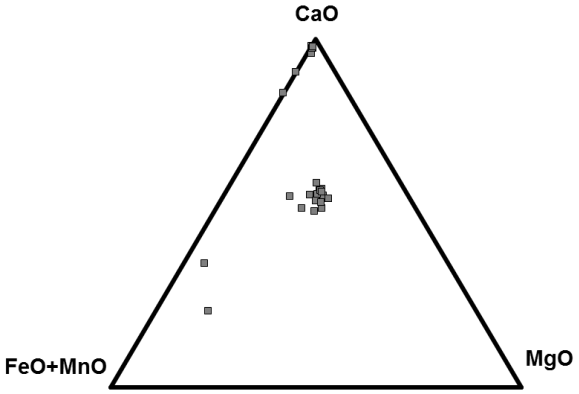
CaO
FeO+MnO
MgO

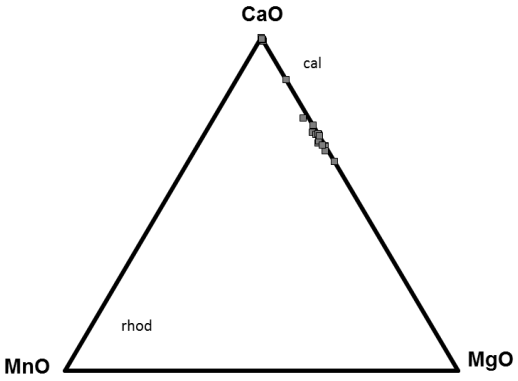
CaO
cal
rhod
MnO
MgO

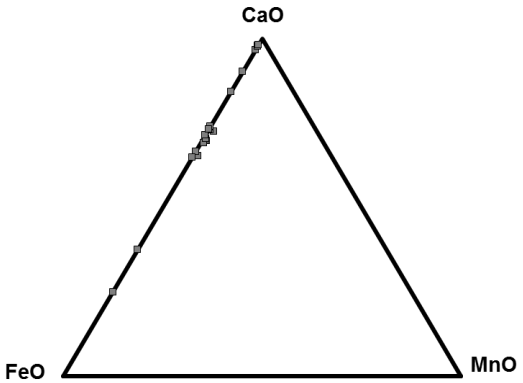
CaO
FeO
MnO

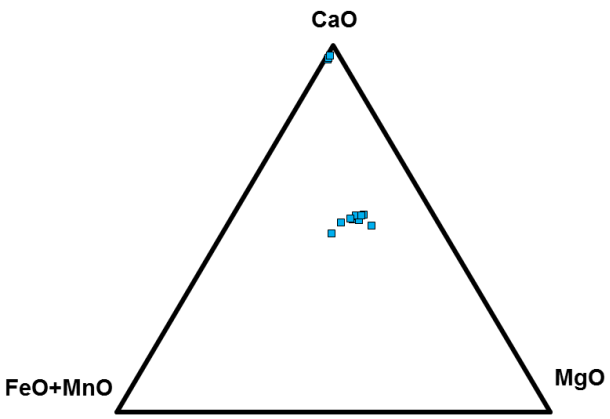
CaO
FeO+MnO
MgO

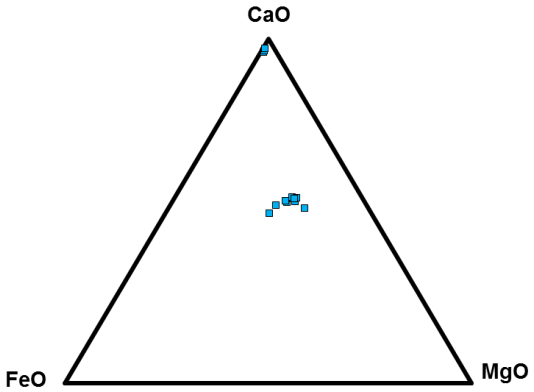
CaO
FeO
MgO

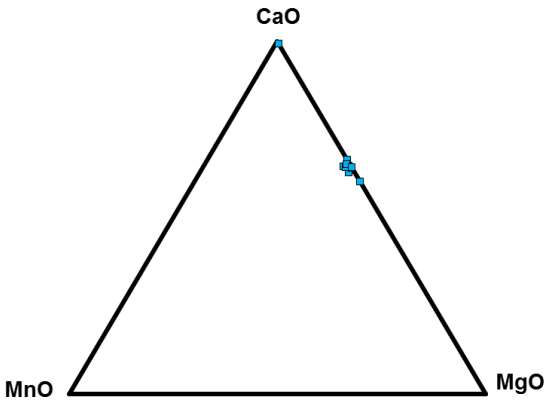
CaO
MnO
MgO

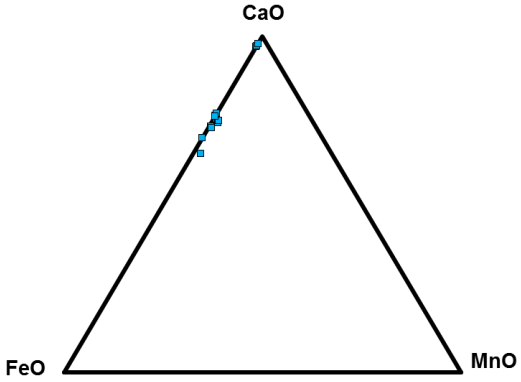
CaO
FeO
MnO

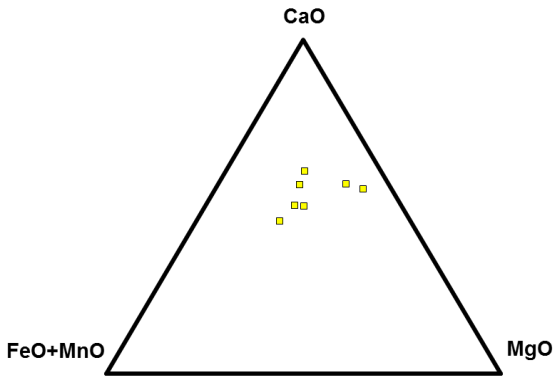
CaO
FeO+MnO
MgO

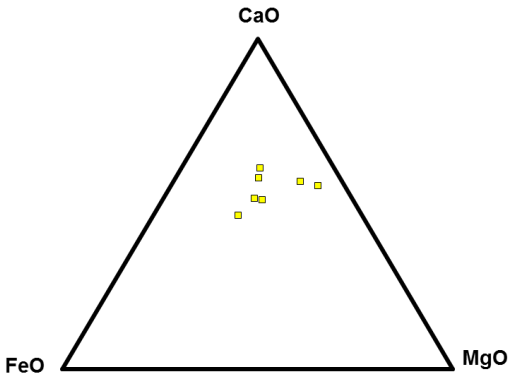
CaO
FeO
MgO

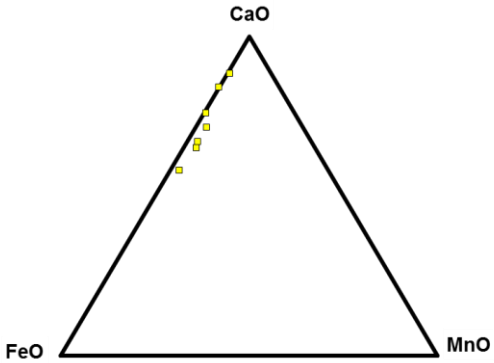
CaO
FeO
MnO

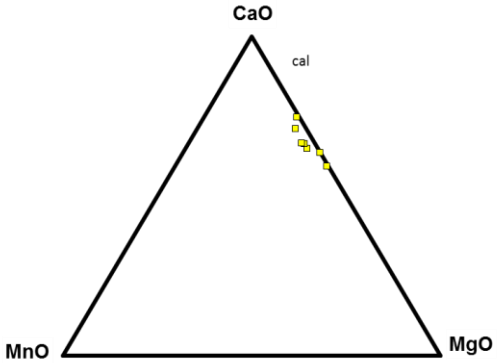
CaO
cal
MnO
MgO

153A

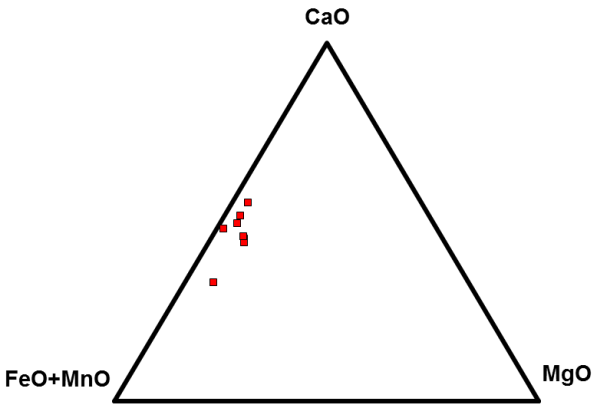

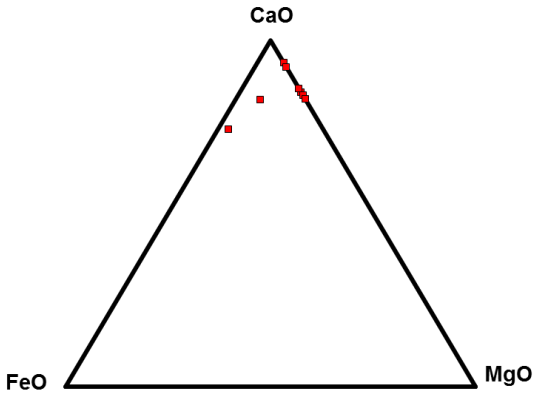

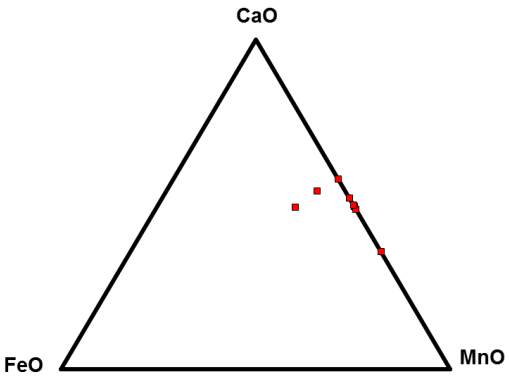

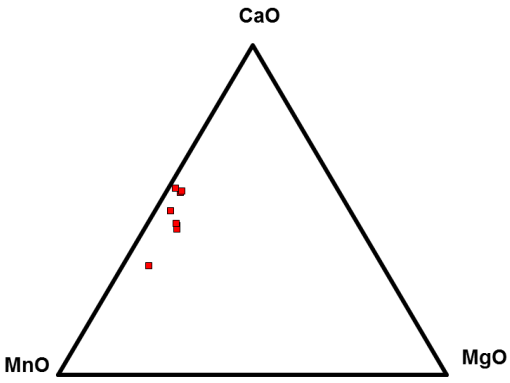

153B

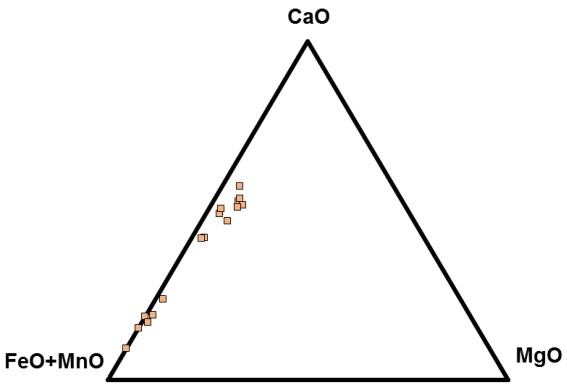

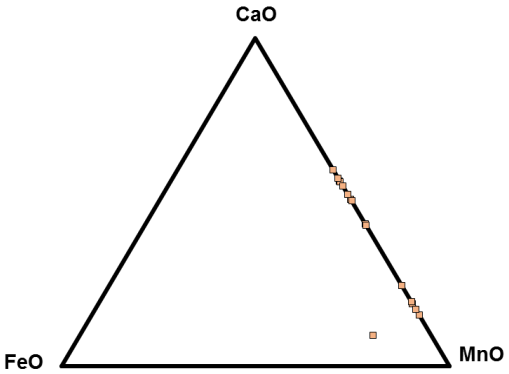

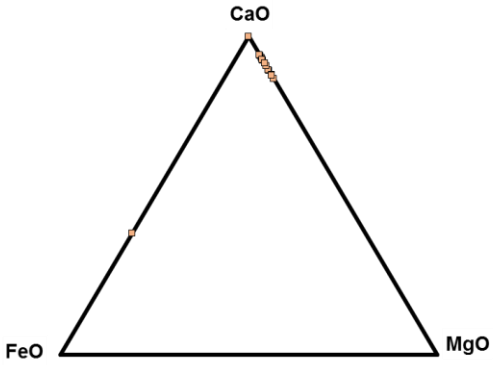

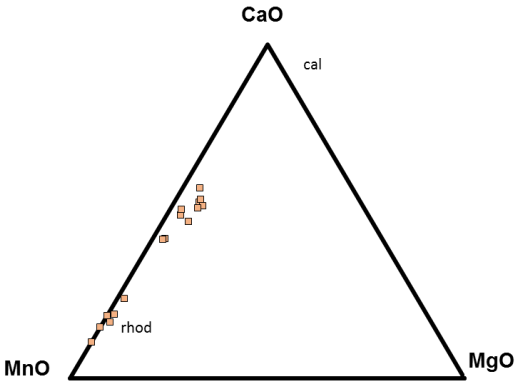

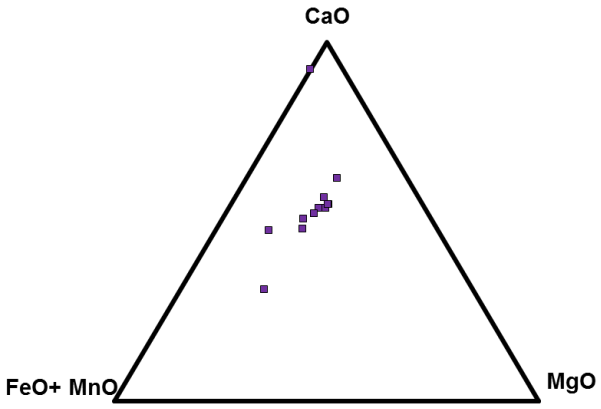
CaO
FeO+ MnO
MgO

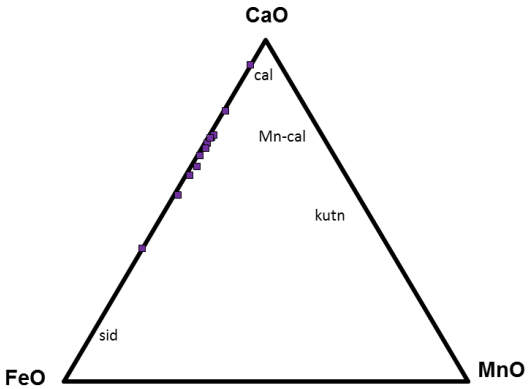
CaO
cal
Mn-cal
kutn
sid
FeO
MnO

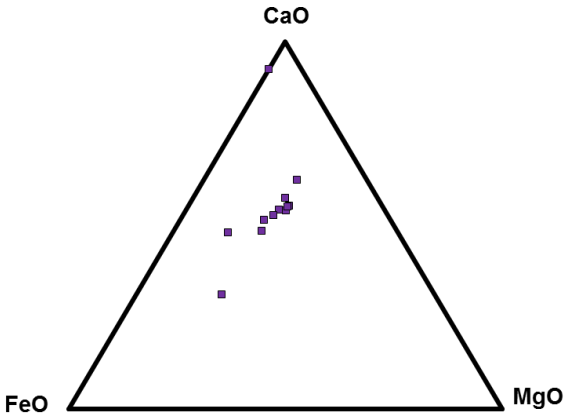
CaO
FeO
MgO

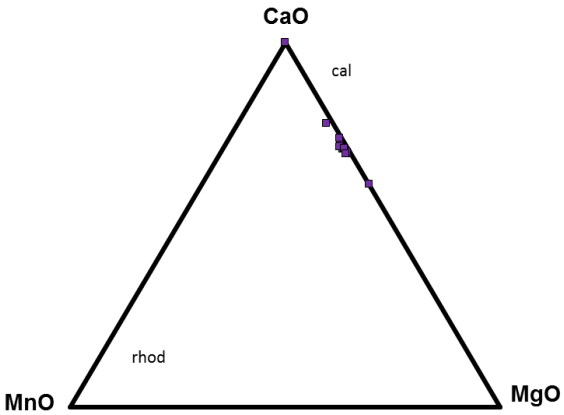
CaO
cal
rhod
MnO
MgO

SI 12. Carbonate composition of samples based on EPMA analyses

Sample ID	Composition of carbonate (EPMA)	Note
86	$Ca(Ca_{0.3}Fe_{0.2}Mg_{0.5})(CO_3)_2$ $Ca(Fe_{0.6}Mg_{0.38}Mn_{0.02})(CO_3)_2$ $Ca(Fe_{0.6}Mg_{0.4})(CO_3)_2$ $Ca(Ca_{0.5}Fe_{0.49}Mg_{0.01})(CO_3)_2$ $Ca(Fe_{0.8}Ca_{0.2})(CO_3)_2$ $CaFe(CO_3)_2$ $Ca(Fe_{0.6}Ca_{0.4})(CO_3)_2$ $Ca(Fe_{0.6}Mg_{0.38}Mn_{0.02})(CO_3)_2$ $Ca(Fe_{0.6}Mg_{0.38}Mn_{0.02})(CO_3)_2$ $Ca(Ca_{0.5}Mg_{0.49}Fe_{0.01})(CO_3)_2$ $Ca(Ca_{0.5}Mg_{0.49}Fe_{0.01})(CO_3)_2$ $Ca(Ca_{0.5}Mg_{0.48}Fe_{0.02})(CO_3)_2$	
88	$Ca(Ca_{0.24}Fe_{0.6}Mg_{0.25}Mn_{0.01})(CO_3)_2$ $Ca(Ca_{0.18}Fe_{0.4}Mg_{0.4}Mn_{0.02})(CO_3)_2$ $Ca(Ca_{0.2}Fe_{0.4}Mg_{0.4})(CO_3)_2$ $Ca(Ca_{0.15}Fe_{0.45}Mg_{0.4})(CO_3)_2$ $Ca(Ca_{0.1}Fe_{0.6}Mg_{0.3})(CO_3)_2$ $Ca(Fe_{0.8}Mg_{0.2})(CO_3)_2$ $Ca(Fe_{0.6}Mg_{0.4})(CO_3)_2$ $Ca(Fe_{0.6}Mg_{0.4})(CO_3)_2$ $Ca(Ca_{0.09}Fe_{0.6}Mg_{0.3}Mn_{0.01})(CO_3)_2$ $Ca(Ca_{0.09}Fe_{0.6}Mg_{0.3}Mn_{0.01})(CO_3)_2$ $Ca(Ca_{0.1}Fe_{0.5}Mg_{0.4})(CO_3)_2$ $Ca(Ca_{0.1}Fe_{0.5}Mg_{0.4})(CO_3)_2$ $Ca(Ca_{0.09}Fe_{0.6}Mg_{0.3}Mn_{0.01})(CO_3)_2$ $Ca(Ca_{0.1}Fe_{0.6}Mg_{0.3})(CO_3)_2$ $Ca(Ca_{0.1}Fe_{0.5}Mg_{0.4})(CO_3)_2$ $Ca(Ca_{0.1}Fe_{0.5}Mg_{0.4})(CO_3)_2$ $Ca(Ca_{0.1}Fe_{0.5}Mg_{0.4})(CO_3)_2$ $Ca(Ca_{0.1}Fe_{0.5}Mg_{0.4})(CO_3)_2$	
93	$Ca(Ca_{0.09}Mg_{0.5}Fe_{0.4}Mn_{0.01})(CO_3)_2$ $Ca(Ca_{0.09}Mg_{0.5}Fe_{0.4}Mn_{0.01})(CO_3)_2$ $Ca(Ca_{0.1}Mg_{0.6}Fe_{0.3})(CO_3)_2$ $Ca(Ca_{0.08}Mg_{0.55}Fe_{0.35}Mn_{0.02})(CO_3)_2$ $Ca(Ca_{0.1}Mg_{0.4}Fe_{0.5})(CO_3)_2$ $Ca(Ca_{0.08}Fe_{0.55}Mg_{0.35}Mn_{0.02})(CO_3)_2$ $Ca(Ca_{0.08}Mg_{0.55}Fe_{0.35}Mn_{0.02})(CO_3)_2$ $Ca(Ca_{0.09}Mg_{0.55}Fe_{0.35}Mn_{0.01})(CO_3)_2$ $Ca(Ca_{0.2}Mg_{0.45}Fe_{0.35})(CO_3)_2$ $Ca(Ca_{0.2}Mg_{0.45}Fe_{0.35})(CO_3)_2$	
152	$Ca(Fe_{0.5}Mg_{0.45}Mn_{0.05})(CO_3)_2$ $Ca(Ca_{0.2}\ Fe_{0.1}Mg_{0.65}Mn_{0.05})(CO_3)_2$ $Ca(Ca_{0.2}\ Fe_{0.1}Mg_{0.7})(CO_3)_2$ $Ca(Ca_{0.15}\ Fe_{0.45}Mg_{0.35}Mn_{0.05})(CO_3)_2$	

	$Ca(Ca_{0.2}\ Fe_{0.3}Mg_{0.35}Mn_{0.05})\ (CO_3)_2$ $Ca(Fe_{0.6}Mg_{0.35}Mn_{0.05})\ (CO_3)_2$ $Ca(Ca_{0.12}Fe_{0.5}Mg_{0.3}Mn_{0.08})\ (CO_3)_2$	
153A	$(Ca_{0.8}Mn_{0.2})(Mn_{0.96}Sr_{0.04})\ (CO_3)_2$ $(Ca_{0.8}Mn_{0.2})(Mn_{0.96}Sr_{0.04})\ (CO_3)_2$ $Ca(Ca_{0.18}Mn_{0.8}Sr_{0.02})\ (CO_3)_2$ $Ca(Mn_{0.89}Fe_{0.1}Sr_{0.01})\ (CO_3)_2$ $Ca(Mn_{0.7}Fe_{0.2}Sr_{0.1})\ (CO_3)_2$ $(Ca_{0.8}Mn_{0.2})(Mn_{0.95}Sr_{0.05})\ (CO_3)_2$ $(Ca_{0.6}Mn_{0.4})Mn\ (CO_3)_2$ $CaMn\ (CO_3)_2$	Sr
153B	$Ca(Mn_{0.88}Mg_{0.1}Sr_{0.02})\ (CO_3)_2$ $Ca(Mn_{0.8}Mg_{0.18}Sr_{0.02})\ (CO_3)_2$ $Ca(Mn_{0.88}Mg_{0.1}Sr_{0.02})\ (CO_3)_2$ $(Ca_{0.3}Mn_{0.7})(Mn_{0.88}Sr_{0.02})\ (CO_3)_2$ $(Ca_{0.3}Mn_{0.7})(Mn_{0.84}Mg_{0.04}Sr_{0.02})\ (CO_3)_2$ $(Ca_{0.8}Mn_{0.2})(Mn_{0.88}Mg_{0.1}Sr_{0.02})\ (CO_3)_2$ $(Ca_{0.9}Mn_{0.1})(Mn_{0.88}Mg_{0.1}Sr_{0.02})\ (CO_3)_2$ $(Mn_{0.8}Ca_{0.2})(Mn_{0.98}Sr_{0.02})\ (CO_3)_2$ $(Mn_{0.2}Ca_{0.8})(Mn_{0.9}Mg_{0.08}Sr_{0.02})\ (CO_3)_2$ $(Mn_{0.2}Ca_{0.8})(Mn_{0.9}Mg_{0.08}Sr_{0.02})\ (CO_3)_2$ $(Mn_{0.1}Ca_{0.9})(Mn_{0.9}Mg_{0.08}Sr_{0.02})\ (CO_3)_2$ $(Ca_{0.3}Mn_{0.7})(Mn_{0.97}Mg_{0.3})\ (CO_3)_2$ $(Ca_{0.3}Mn_{0.7})(Mn_{0.9}Mg_{0.1})\ (CO_3)_2$ $Ca(Mn_{0.8}Ca_{0.2}Mg_{0.1})\ (CO_3)_2$ $(Ca_{0.9}Mn_{0.1})(Mn_{0.98}Mg_{0.02})\ (CO_3)_2$ $(Ca_{0.4}Mn_{0.6})(Mn_{0.98}Mg_{0.02})\ (CO_3)_2$	Sr
157	$Ca(Ca_{0.18}Fe_{0.45}Mg_{0.35}Mn_{0.02})\ (CO_3)_2$ $Ca(Ca_{0.28}Fe_{0.35}Mg_{0.35}Mn_{0.02})\ (CO_3)_2$ $Ca(Ca_{0.38}Fe_{0.3}Mg_{0.3}Mn_{0.02})\ (CO_3)_2$ $Ca(Ca_{0.18}Fe_{0.45}Mg_{0.35}Mn_{0.02})\ (CO_3)_2$ $Ca(Ca_{0.08}Fe_{0.55}Mg_{0.35}Mn_{0.02})\ (CO_3)_2$ $Ca(Ca_{0.08}Fe_{0.55}Mg_{0.35}Mn_{0.02})\ (CO_3)_2$ $Ca(Fe_{0.68}Mg_{0.3}Mn_{0.02})\ (CO_3)_2$ $Ca(Fe_{0.68}Mg_{0.3}Mn_{0.02})\ (CO_3)_2$ $Ca(Fe_{0.78}Mg_{0.2}Mn_{0.02})\ (CO_3)_2$ $Ca(Fe_{0.78}Mg_{0.2}Mn_{0.02})\ (CO_3)_2$ $Ca(Fe_{0.5}Mg_{0.5})\ (CO_3)_2$	

SI 13. Temperature calculation on $\delta^{18}O_{SMOWcarb}$ (based on Kim et al., 2009; Hodel et al., 2018)

Kim et al., 2009; Hodel et al., 2018	**Temperature calculation, estimation**						
In Urucum rhodochrosite and other mixed carbonates	Neoproterozoic		1. equation	2. equation		Sample	Section
$d^{18}O_{carb}$ vs SMOW	d18O water vs SMOW	a (rod-water)	Temperature ºC	Temperature ºC		Cor	(Fig. 14)
26.25	-1.33	1.02761673	37.2	37.3		86	F
23.12	-1.33	1.024482562	54.6	56.1		87	F
24.9	-1.33	1.026264932	44.5	45.0		88	F
27.41	-1.33	1.028778275	31.2	31.1		93	F
23.42	-1.33	1.024782961	52.9	54.1		97	F
21.87	-1.33	1.023230897	62.2	64.6		127	D
20.23	-1.33	1.021588713	72.6	77.0		133	D
19.53	-1.33	1.020887781	77.3	82.7		137	D
20.04	-1.33	1.02139846	73.8	78.5		141	D
28.68	-1.33	1.030049966	24.9	24.7		152	E
22.68	-1.33	1.024041976	57.2	59.0		153A	E
21.91	-1.33	1.02327095	61.9	64.4		153B	E
26.35	-1.33	1.027716863	36.7	36.7		157	E
22.76	-1.33	1.024122082	56.8	58.5		168	D

Table S1. Samples and methods used

Sample Number	Nodule types and sections	Description	OM	CL	FTIR	Raman	SI	EPMA
COR-86	1, 2, 4A, 4B C	wavy but not uniformly laminated ore	102	54	51	1,192	1	8(30)
COR-88	1, 2A A, B	BIF, similar to other global occurrences, 5-10% zonal nodules are characteristic both in jasper and hematite, inside jasper layer nodules and further in jasper (red layers) very fine sub mm silica layers, which are thin, black layers in red jasper	132	105	68	1,363	1	6(26)
COR-93	3, 3B	rare BIF, plenty of nodules which destroy lamination very unique in Brazil, not identified elsewhere in the World "embedded nodule"	45	33	11	209	1	4(14)
COR-141	F	Fe sandstone (field classification), fragments: quartz, feldspar, jasper, matrix is hematite, Fe clastic rock, (Mn 1 carbonate)	55	54	30	701	1	1
COR-150A	not studied in detail	Mn-2 – Manganese ore	18					
COR-152	D, E	micro-conglomerate with carbonate fragments	39	75	59	1,302	1	5(7)
COR-153A	6 G	silty layers in several hematitic layers	63	84	42	761	1	4(10)
COR-153B	5	fractures filled with carbonate, It is massive manganese, probably Mn-1, eleven km from Santa Cruz Hill	22	63	12	101	1	4(16)
COR-157	2, 2B, 3	biomat, embedded nodules.	40	81	57	416	1	4(12)
Total			**516**	**549**	**330**	**6,045**	**8**	**36(115)**

Abbrev.: OM: optical rock microscopy; CL: cathodoluminescence microscopy; FTIR: infrared spectroscopy; Raman: Raman spectroscopy; SI: stable C and O isotope study; EPMA: electron probe micro analyser (EDS, bse images and spectra).

Table S2. Mineral and organic matter composition and frequency*

Nodules		Mineral composition		
	Sample ID	**Main**	**Moderate**	**Rare**
1	86 (total number 101)	hematite, ankerite, rhodochrosite	kutnohorite, quartz, feldspar (albite)	goethite, Mn-bearing calcite, apatite
1	88	hematite	kutnohorite, ankerite	rhodochrosite, Mn-calcite, quartz, albite
2	86	hematite	kutnohorite, rhodochrosite, ankerite, quartz, albite	Mn-calcite, siderite, dolomite, mica, apatite
2A	88	hematite, ankerite, quartz	kutnohorite	rhodochrosite, Mn-calcite, goethite, albite, marcasite
3	93	hematite	rhodochrosite, ankerite, quartz, dolomite	kutnohorite, marcasite, albite, apatite
	157	hematite	pyrolusite, manjiroite, rhodochrosite, ankerite, Mn-calcite, siderite, quartz	jacobsite, albite
4	86	hematite	rhodochrosite, kutnohorite, ankerite, quartz, albite	Mn-calcite, siderite
5	153B		pyrolusite, braunite, manjiroite, rhodochrosite, Mn-calcite, hematite, siderite, albite, apatite	
6	153A		manjiroite, rhodochrosite, hematite, jacobsite	
Sections				
A	88	hematite, ankerite	rhodochrosite, quartz	siderite, apatite
B	88	hematite, ankerite	kutnohorite, Mn-calcite, quartz, apatite	rhodochrosite, siderite
C	86	hematite, rhodochrosite, ankerite, quartz	Mn-calcite, kutnohorite	siderite, apatite
D	152	hematite	kutnohorite	Mn-calcite, quartz, albite, apatite
E	152	hematite, kutnohorite	rhodochrosite, Mn-calcite, quartz, albite	apatite
F	141	hematite, manganite, quartz, albite	apatite	todorokite, manjiroite, kutnohorite, goethite, aegirine
G	153A	hematite, anatase	rhodochrosite, Mn-calcite, siderite, quartz, albite, apatite	manganite, kutnohorite, alabandite, marcasite, goethite, dolomite, aegirine

Organic matter in nodules is under detection limit, rare, and low moderate in some cases.
Organic matter in sections is present in higher amounts. The most frequent is type org 2, moderate frequency is types org 3 and org 5, and graphite also occurs.
*Mineral and organic matter composition - estimation - rare: below 10 spectra/mineral/sample; moderate: 10-100 spectra/mineral/sample; main: more than 100 spectra/mineral/sample

Table S3. Raman profiles, point dataset and FTIR mineralogy both for nodules and sections according to Fe and Mn cycles and syn-and diagenetic formation

Nodules	**Sections**
Mn cycle is supported by: **various Mn oxides**: **Syngenetic:** not detected **Diagenetic** *oxide:* pyrolusite, jacobsite, manjiroite *ox/sil:* braunite *carbonates:* rhodochrosite, Mn-bearing calcite, kutnohorite *sulfides* not detected	**Mn cycle is supported by:** **various Mn oxides**: **Syngenetic:** todorokite **Diagenetic** *oxide:* manjiroite, manganite *ox/sil:* not detected *carbonates:* rhodochrosite, Mn-bearing calcite, kutnohorite *sulfides:* alabandite
Fe cycle is supported by: **various Fe oxides-hydroxides:** **Syngenetic:** ferrihydrite **Diagenetic** *oxides:* goethite, hematite *carbonate:* siderite: ankerite *silicate:* not detected *sulfide:* marcasite	**Fe cycle is supported by:** **various Fe oxides-hydroxides:** **Syngenetic:** ferrihydrite **Diagenetic** *oxides:* goethite, hematite, anatase (TiO_2 - $\mathbf{Fe_xTi_{(1-x)}O_{(2-x)}OH_x}$) *carbonate:* siderite, ankerite *silicate:* aegirine *sulfide:* marcasite
Other minerals: *oxide:* **quartz – characteristic cyclicity** *carbonate:* dolomite *silicate:* albite, mica (muscovite), montmorillonite, *phosphate:* apatite	**Other minerals:** *oxide:* **quartz – characteristic cyclicity** *carbonate:* dolomite *silicate:* albite, mica (muscovite) *phosphate:* apatite

Mineral distributions are shown in Fig. 9 and Fig. 10 and SI 7, 8.

Table S4A. Sections - Mineral assemblage in Urucum Fe ore (Brazil) and typical minerals indicative of Eh-pH ranges based on environmental mineralogy (low T)

Mineral assemblage is based on Raman and FTIR spectroscopy analyses

Minerals/ Processes	Chemical formula	A	B	C	D	E	F	G	Eh		pH			Microbially
Sample ID		88	88	86	152	152	141	153A						
Mn mineral assemblage									ox-subox	anox	acidic	neutral-slightly alkaline	alkaline	**mediated**
Oxides and hydroxide														
Todorokite	$Na_{0.2}Ca_{0.05}K_{0.02}Mn^{4+}{}_4Mn^{3+}{}_2O_{12}•3(H_2O)$						*		*			*		*
Manjiroite	$Na(Mn^{4+}{}_7Mn^{3+})O_{16}$						*							
Manganite	$Mn^{3+}OOH$						*	*	*					*
Carbonates														
Rhodochrosite	$MnCO_3$	*	*	*		*		*	*			*		*
Kutnohorite	$CaMn^{2+}(CO_3)_2$	*	*	*	*	*	*	*	*			*		*
Mn-bearing calcite	Mn-$CaCO_3$		*	*	*	*		*	*			*		
Oxides-silicates														
Sulfides														
Alabandite	MnS							*		*				*
Fe mineral assemblage														
Oxides and hydroxides														
Ferrihydrite	FeOOH	*	*	*		*		*	*			*		*
Hematite	Fe_2O_3	*	*	*	*	*	*	*	*					
Goethite	FeOOH						*		*					
Anatase	TiO_2 - $Fe_xTi_{(1-x)}O_{(2-x)}OH_x$							*	*			*		*
Carbonates														
Siderite	$FeCO_3$	*	*	*	*	*		*						*
Ankerite	$Ca(Fe^{2+}.Mg)(CO_3)_2$	*	*	*										
Silicates														
Aegirine	$Ca_{0.75}Na_{0.25}Mg_{0.5}Fe^{2+}{}_{0.25}Fe^{3+}{}_{0.25}(Si_2O_6)$						*	*					*	
Sulfides														
Marcasite	FeS_2							*			*			
Others														
Oxides – hyydroxides														
Quartz	SiO_2	*	*	*	*	*	*	*			*			*
Carbonates														
Dolomite	$CaMg(CO_3)_2$	*	*			*		*	*			*		*
Silicates														
Albite	$NaAlSi_3O_8$	*	*	*	*	*	*	*				*		*
Mica (muscovite)	$KAl_3Si_3O_{10}(OH)_{1.8}F_{0.2}$					*								
Phosphates														
Apatite	$[(Ca_{10}(PO_4)_6(OH.F.Cl)_2]$	*	*	*	*	*	*	*	*			*	*	*
Sulphates														
Organic material		*	*	*	*	*	*	*						*

Table S4B. Nodules - Mineral assemblage in Urucum Fe ore, Brazil. and typical minerals indicative of Eh-pH ranges based on environmental mineralogy (low T)

Mineral assemblage is based on Raman and FTIR spectroscopy analyses

Minerals/ Processes	**Chemical formula**	**1**	**2**	**2 A**	**3**	**4**	**5**	**6**	**Eh**		**pH**			**Microbially**
Sample ID		8688	86157	88	93157	86	153B	153A						
Mn mineral assemblage									ox-subox	anox	acidic	neutral-slightly alkaline	alkaline	**mediated**
Oxides and hydroxide														
Pyrolusite	$Mn^{4+}O_2$		*		*		*		*					
Jacobsite	$Mn^{2+}_{0.6}Fe^{2+}_{0.3}Mg_{0.1}Fe^{3+}_{1.5}Mn^{3+}_{0.5}O_4$		*		*			*						
Manjiroite	$Na(Mn^{4+}_7Mn^{3+})O_{16}$		*		*		*	*						
Carbonates														
Rhodochrosite	$MnCO_3$	*	*	*	*	*	*	*	*			*		*
Kutnohorite	$CaMn^{2+}(CO_3)_2$	*	*	*	*	*			*			*		*
Mn-bearing calcite	Mn-$CaCO_3$	*	*	*	*	*	*	*	*			*		
Oxides-silicates														
Braunite	$Mn^{2+}Mn^{3+}_6SiO_{12}$						*		*				*	*
Sulfides														
Fe mineral assemblage														
Oxides and hydroxides														
Ferrihydrite	FeOOH	*	*	*	*			*	*			*		*
Hematite	Fe_2O_3	*	*	*	*	*	*	*	*					
Goethite	FeOOH	*		*					*					
Carbonates														
Siderite	$FeCO_3$		*		*	*	*							*
Ankerite	$Ca(Fe^{2+}.Mg)(CO_3)_2$	*	*	*	*	*								
Silicates														
Sulfides														
Marcasite	FeS_2			*	*						*			
Others														
Oxides – hyydroxides														
Quartz	SiO_2	*	*	*	*	*	*	*			*			*
Carbonates														
Dolomite	$CaMg(CO_3)_2$	*	*		*			*	*			*		*
Silicates														
Albite	$NaAlSi_3O_8$	*	*	*	*	*	*					*		*
Mica (muscovite)	$KAl_3Si_3O_{10}(OH)_{1.8}F_{0.2}$		*											
Montmorillonite	$(Na.Ca)(Al.Mg)_2Si_4O_{10}(OH)_2xnH_2O$	*							*			*		
Phosphates														
Apatite	$[(Ca_{10}(PO_4)_6(OH.F.Cl)_2]$	*	*		*	*	*		*			*	*	*
Sulphates														
Organic material		*	*	*	*	*	*	*						*

Table S4C. Area measurements FTIR - Mineral assemblage in Urucum Fe ore, Brazil. and typical minerals indicative of Eh-pH ranges based on environmental mineralogy (low T)

Mineral assemblage is based on FTIR spectroscopy analyses

Minerals/ Processes	**Chemical formula**	**Area 1**	**Area 1**	**Area 2**	**Area 3**	**Eh**		**pH**			**Microbially**
Sample ID		86	157	157	157						
Mn mineral assemblage						ox-subox	anox	acidic	neutral-slightly alkaline	alkaline	**mediated**
Carbonates											
Rhodochrosite	$MnCO_3$		*	*	*	*			*		*
Kutnohorite	$CaMn^{2+}(CO_3)_2$					*			*		*
Oxides-silicates											
Fe mineral assemblage											
Oxides and hydroxides											
Hematite	Fe_2O_3				*	*					
Others											
Oxides – hyydroxides											
Quartz	SiO_2	*	*	*	*			*			*
Carbonates											
Montmorillonite	$(Na.Ca)(Al.Mg)_2Si_4O_{10}(OH)_2xnH_2O$										
Phosphates											
Apatite	$[(Ca_{10}(PO_4)_6(OH.\ F.\ Cl)_2]$	*	*			*			*	*	*
Sulphates											
Organic material		*	*	*	*						*

Eh-pH ranges and microbially mediated mineralogy is based on: Listova (1961); Harder (1976. 1978); Trudinger& Swaine eds. (1979); Berner (1980); Giovanoli (1980); Sung & Morgan (1981); Cole & Shaw (1983); Ewers (1983); Maynard (1983); Coleman (1985); Skinner (1993); Ehrenreich & Widdel (1994); Wignall (1994); Mandernack et al. (1995); Straub et al. (1996); Banfield & Nealson (1997); Konhauser (1998); Herdianita et al. (2000); Ehrlich (2002); Bazylinski & Frankel (2003); Villalobos et al.(2003); Bargar et al. (2005); Dupraz & Visscher (2005); Morgan (2005); Bodeï et al. (2007); Schwertmann & Cornell (2007); Dupraz et al. (2009); Sanz-Montero et al. (2009); Chan et al. (2011); Polgári.et al. (2012a, 2012b, 2013, 2016); Biagioni et al. (2014); Johnson et al. (2016); Gyollai et al. (2017); Mloszewska et al. (2018)

Table S4D: Samples - EPMA – Further mineral assemblage in Urucum Fe ore, Brazil, and typical minerals indicative of Eh-pH ranges based on environmental mineralogy (low T)

Mineral assemblage is based on EPMA

Minerals/ Processes	**Chemical formula**								**Eh**		**pH**			**Microbially**
Sample ID		86	88	93	152	153A	153B	157						
Mn mineral assemblage									ox-subox	anox	acidic	neutral-slightly alkaline	alkaline	**mediated**
Carbonates														
Rhodochrosite	$MnCO_3$					*	*		*			*		*
Kutnohorite	$CaMn^{2+}(CO_3)_2$					*	*		*			*		*
Calcite	Mn-$CaCO_3$	*	*	*				*	*			*		
Fe mineral assemblage														
Oxides and hydroxides														
Hematite	Fe_2O_3	*	*	*	*	*	*	*	*					
Carbonates														
Ankerite	$Ca(Fe^{2+},Mg)(CO_3)_2$	*	*	*	*			*						
Sulfides														
Pyrite	FeS_2						*			*	*			
Others														
Oxides – hyydroxides														
Quartz	SiO_2	*	*	*	*	*		*			*			*
Carbonates														
Witherite	$BaCO_3$						*		*					
Silicates														
K-feldspar	$KAlSi_3O_8$					*						*		*
Plagioclase	$NaAlSi_3O_8$							*				*		*
Zircon	$ZrSiO_4$					*								
Mica (muscovite)	$KAl_3Si_3O_{10}(OH)_{1.8}F_{0.2}$				*									
Clay mineral	$(Na,Ca)(Al,Mg)_2Si_4O_{10}(OH)_2xnH_2O$	*				*			*			*		
Phosphates														
Apatite	$[(Ca_{10}(PO_4)_6(OH, F, Cl)_2]$	*	*	*	*			*	*			*	*	*
Xenotime	YPO_4	*												
Sulphates														
Baryte	$BaSO_4$						*					*		*
Coelestite	$SrSO_4$						*							*

Table S5. Carbonate types and $\delta^{13}C_{PDBcarb}$ and $\delta^{18}O_{PDBcarb}$ values of sedimentary carbonates in BIFs and Mn ore from Urucum and Vetorial mines, Urucum region (MS, Brazil). $\delta^{13}C_{PDBcarb}$ and $\delta^{18}O_{PDBcarb}$ values of sedimentary Tamengo Formation are according to Boggiani et al. (2010).

Urucum rocks and ore	Samples ID	Carbonate type**	$\delta C^{13}_{PDBcarb}$ ‰	$\delta^{18}O_{PDBcarb}$ ‰
BIF with sedimentary * biochemical carbonate (section F)	COR-86	Siderite, ankerite, rhodochrosite, kutnohorite, Mn-bearing calcite	-3.38	-4.52
BIF with sedimentary biochemical carbonate (section F)	COR-87		-4.42	-7.56
BIF with sedimentary biochemical carbonate (section F)	COR-88	Rhodochrosite, ankerite, kutnohorite, Mn-bearing calcite, siderite, dolomite	-3.85	-5.83
BIF with sedimentary biochemical carbonate (section F)	COR-93	Rhodochrosite, ankerite, kutnohorite, dolomite	-3.49	-3.40
BIF with sedimentary biochemical carbonate (section F)	COR-97		-4.21	-7.27
BIF with sedimentary biochemical carbonate (section D)	COR-127		-4.61	-8.77
BIF with sedimentary biochemical carbonate (section D)	COR-137		-5.01	-11.04
BIF with sedimentary biochemical carbonate (section D)	COR-141		-2.53	-10.55
BIF with sedimentary biochemical carbonate (section E)	COR-157	Rhodochrosite, kutnohorite, Mn-bearing calcite, siderite, ankerite	-3.92	-4.42
BIF with sedimentary biochemical carbonate (section D)	COR-168 =COR-14		-4.58	-7.90
BIF with sedimentary biochemical carbonate (section D)	COR-133		-5.79	-10.36
BIF with sedimentary clastic (section E)	COR-151		-3.49	1.06
BIF with sedimentary clastic (section E)	COR-152	Siderite, dolomite, rhodochrosite, kutnohorite, Mn-bearing calcite	-3.65	-2.16
Mn-3 layer Mn ore with biochemical carbonate (section E)	COR-153A	Siderite, dolomite, rhodochrosite, kutnohorite, Mn-bearing calcite	-5.34	-7.98
Mn-3 layer Mn ore with biochemical carbonate (section E)	COR-153B	Rhodochrosite, Mn-bearing calcite, siderite,	-7.08	-8.73
$\delta^{13}C_{PDBcarb}$ and $\delta^{18}O_{PDBcarb}$ average values of carbonate of BIFs from Urucum				
		BIF average	-4.16	-7.42
		BIF S.D.	0.84	2.52
		BIF variation (+/-)	0.59	1.77
		BIF average value (2σ)	-4.16±0.59	-7.42±1.77
$\delta^{13}C_{PDBcarb}$ of Tamengo Formation carbonate rocks				
			$\delta C^{13}_{PDBcarb}$	$\delta^{18}O_{PDBcarb}$
Tamengo Formation – Corcal location		Average value (±2σ)	4.71 ± 0.30	-6.70 ± 0.64
Tamengo Formation – Saladeiro location		Average value (±2σ)	4.00 ± 0.66	-7.94 ± 0.90
Tamengo Formation - Eastern Laginha mine		Average value (±2σ)	2.91 ± 0.23	-6.96 ± 0.24
Tamengo Formation – Western Laginha mine		Average value (±2σ)	1.35 ± 1.23	-7.44 ± 1.94
Tamengo Formation – Western base of the Laginha mine		Average value (±2σ)	-0.71 ± 0.48	-7.45 ± -2.95

*sections are according to Fig. 2 and Fig. 14

**carbonate types were determined by FTIR and Raman spectroscopy